Studies of Bright Steep-Spectrum Radio Sources

N. M. Lipovka[1], A. A. Lipovka[1], O. V. Verkhodanov[2], and E. Chavira[3]

[1]*St. Petersburg Branch of the Special Astrophysical Observatory, Russian Academy of Sciences,*
Pulkovo, St. Petersburg, 196140 Russia

[2]*Special Astrophysical Observatory, Russian Academy of Sciences, Nizhniĭ Arkhyz,*
Karachaevo-Cherkesskaya Republic, 357147 Russia

[3]*Instituto Nacional de Astrofísica, Óptica y Electrónica, Luis Enrique Erro No. 1,*
Apdo Postal 51 y 216, 72840 Tonantzintla, Puebla, México

Received January 28, 1999

Abstract—Results of studies of bright radio sources in the constellation Cetus are presented. More than 50% of the sources have radio spectral indices steeper than 0.9. Optical identifications have been determined for 35 sources. A large fraction of the radio sources are identified with weak blue galaxies. Given their spectral indices, it is likely that these objects have redshifts $z = 0.4$–1.0. More than 20% of the steep-spectrum sources do not have optical identifications and appear to be weak galaxies with $z > 2$. © 2000 MAIK "Nauka/Interperiodica".

1. INTRODUCTION

This paper continues an analysis of a cluster of blue galaxies in Cetus. Individual parts of this region were studied for the first time by Chavira [1] as part of a project proposed by Haro [2] to observe blue galaxies using a 26″/30″ Schmidt camera. In [1], three successive, slightly shifted exposures of a plate were used to identify quickly and reliably objects with blue color excesses. It was shown that the region in question contains many blue galaxies.

In 1993–1994, we continued this work using Palomar glass copies of the sky atlas and a blink comparator and confirmed that, indeed, there are a factor of four more blue galaxies in this cluster compared to other nearby clusters [3, 4].

In accordance with the Butcher–Oemler effect [5], this may indicate that this galaxy cluster is distant. In [6], it was shown using clusters at $z = 0.3$ as an example that the redshifts of blue galaxies can be estimated if their morphological composition and mean projected density are known. Analysis of our catalog led us to suggest that most galaxies in this region should have $z > 0.4$ [4]. Our earlier optical studies showed that 10% of bright blue galaxies (11–14^m) are identified with faint radio sources [7]. These sources are nearby galaxies with compact nuclei and thin spirals or irregular coronal filaments, most of which have been detected in IRAS surveys [8]. However, there are many bright radio sources in this region that are not identified with galaxies because the magnitudes of the associated optical objects are below the limiting magnitude corresponding to our sample.

We attempted to obtain optical identifications of these radio sources using the APM maps [9]. Steep spectrum radio sources are of special interest, since it is believed that these objects are associated with distant galaxies that are often not visible on the Palomar plates due to their large redshifts. As a rule, such galaxies have compact nuclei with jet structures.

In the current paper, we analyze the radio emission from objects within our box in Cetus that were detected in the high-sensitivity NVSS survey [10]. We have determined their spectral indices in the frequency band 365–1400 MHz and performed optical identifications.

2. SPECTRAL CHARACTERISTICS OF THE RADIO GALAXIES

We have detected 66 bright radio sources in a box 15 square degrees in size centered at RA(1950.0) = 2^h34^m and DEC(1950.0) = $-6°$. These sources were detected in two high-sensitivity surveys whose coordinates coincided with high accuracy [10, 11]. We selected objects from these catalogs using the CATs database of Galactic and extragalactic sources [12]. The density of steep-spectrum radio sources in this region is more than twice that in the survey [13].

We determined the spectral indices of these sources at frequencies 365–1400 MHz. Figure 1 presents a histogram of the spectral-index distribution. The spectral indices are plotted along the X-axis, and the number of objects with a given spectral index is plotted along the Y-axis. Over 50% of the objects have spectral indices greater than 0.9.

3. OPTICAL IDENTIFICATIONS

Optical identifications were made using APM maps [9] of 35 areas of the sky. The limiting magnitude of these measurements is 22.5^m for B plates and 21^m for R plates. The optical and radio coordinates of the radio sources, as well as the characteristics of their optical counterparts, are given in the table. Column 1 gives the object
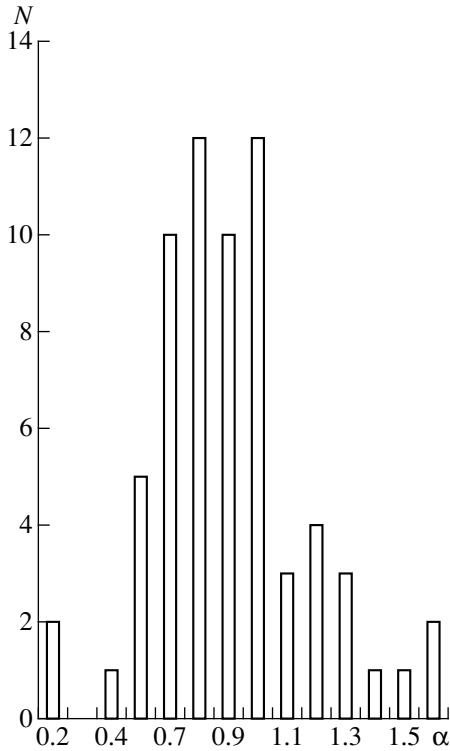
Fig. 1. Histogram of spectral indices.

Fig. 2. Dependence of radio spectral index on the magnitude of the optical counterparts. The square shows the magnitude on the red plate, and the triangle shows the magnitude on the blue plate.

number; columns 2 and 4, equatorial coordinates (epoch 1950.0); columns 3 and 5, observing frequency; columns 7 and 8, flux density and corresponding error; column 9, spectral index at 365–1400 MHz; columns 10 and 11, stellar magnitudes on red and blue plates, respectively; column 12, type of optical object (Gb is blue galaxy, Gr is red galaxy, and EF is empty field); and column 13, the reference.

Nine radio sources were identified with blue galaxies, which were mostly weaker than 19^m. The mean optical magnitude of these galaxies is 20.27 ± 1.66^m. Two galaxies with red color excesses (nos. 19 and 25) have radio spectral indices exceeding 1.0. One source (no. 29) was identified with a blue stellar-like object that is probably a flat-spectrum quasar. One source (no. 30) with an inverted radio spectrum proved to be a bright elliptical galaxy (PGC 10175) at $z = 0.004$. The spectrum of this galaxy is typical of Seyfert galaxies. Over 60% of the sources do not have optical counterparts or fall between two galaxies. These objects are indicated by EF (empty field) in column 12 of the table. The lack of visible optical-counterpart candidates may provide evidence that we are dealing with distant, faint galaxies with magnitudes exceeding 21^m, the limiting magnitude for the APM measurements based on the Palomar plates. Another possibility is that it is necessary to refine the radio coordinates of the studied objects.
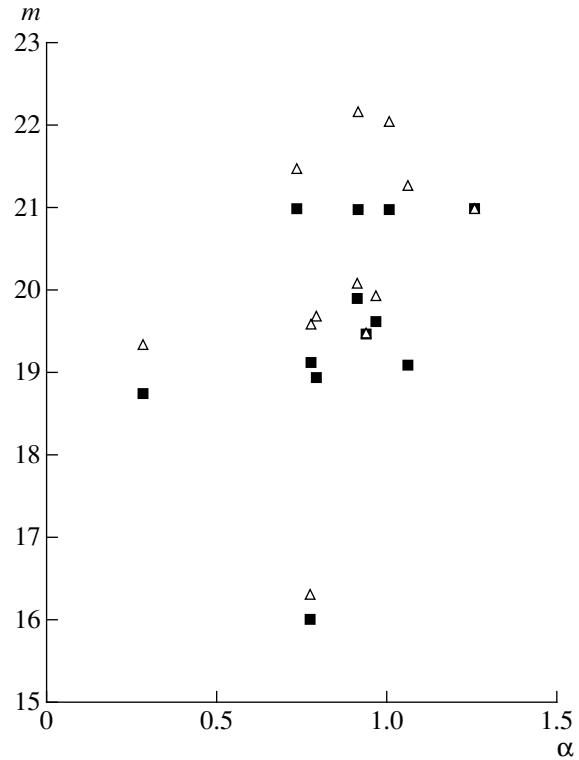
It is thought that the redshift of an object can be determined using the value of its spectral index [13, 14]. In our sample of radio sources identified with blue galaxies, the mean spectral index is $\alpha_{mean} = 0.92 \pm 0.15$, whereas the spectra of the radio sources in empty fields are steeper, $\alpha_{mean} = 1.1 \pm 0.3$. This may indicate that these are more distant, faint galaxies. Figure 2 shows the dependence of the radio spectral indices on the magnitudes of their optical counterparts. The correlation can clearly be traced: the weaker the galaxy, the steeper the spectral index of the associated radio source.

The statistics of the mean radio fluxes show that the identified radio sources are, on average, brighter at radio wavelengths ($P_{mean} = 165 \pm 76$ mJy) than the unidentified sources ($P_{mean} = 106 \pm 70$ mJy).

Studies of this region [3] using the method of Butcher and Oemler [5] suggest that this cluster is located at $z > 0.4$. This conclusion takes into account the observed ratio of elliptical and SO galaxies. On the other hand, using the mean spectral indices of identified galaxies and empty-field radio sources, we arrive at the redshift estimate $z > 0.4$–1.0. A number of objects from the table (nos. 2, 10, 14, 15, 19, 20, and 33) should have $z > 2$. Object no. 4 is an exception, since there is some discrepancy in its radio coordinates, and the object is located in a complex region with many galaxies, so that the observed radio emission could be associated with

Table. Radio source parameters

No.	RA (1950.0)	rms	DEC(1950.0)	rms	ν, MHz	P, MJy	rms, MJy	α	m(R)	m(B)	Type	References
1	2	3	4	5	6	7	8	9	10	11	12	13
1	$2^h28^m02^s.108$	$0^s.245$	$-3°22'27''.57$	$1''.55$	367	168	0.245	0.872				[11]
	2 28 02.00	0.02	−3 22 26.1	0.4	1400	52.1	1.8					[10]
											EF	[9]
2	2 28 14.718	0.164	−7 14 39.72	1.10	365	314	33	1.116				[11]
	2 28 14.58	0.02	−7 14 37.9	0.3	1400	70.0	2.3					[10]
											EF	[9]
3	2 28 56.021	0.047	−4 34 50.38	0.38	365	966	30	0.833				[11]
	2 28 56.02	0.02	−4 34 50.0	0.3	1400	315.4	9.5					[10]
											EF	[9]
4	2 29 11.630	0.133	−5 06 16.96	1.04	365	772	73	1.253				[11]
	2 29 08.8	0.2	−5 06 14	5	408	850	40					[15]
	2 29 10.61	0.2	−5 06 10.1	0.3	1400	143	5.0					[10]
	2 29 10 98		−5 06 11.4						$14^m.62$	$17^m.1$	Gr	[9]
	2 29 10.98		−5 06 15.6						<21.	21.0	Gb	[9]
5	2 29 29.026	0.143	−4 47 12.96	1.06	365	451	39	0.788				[11]
	2 29 28.86	0.02	−4 47 10.5	0.3	1400	156.3	5.0					[10]
											EF	[9]
6	2 29 43.711	0.151	−4 55 03.39	1.10	365	465	43	0.914				[11]
	2 29 43.77	0.02	−4 55 03.9	0.3	1400	136.3	4.3					[10]
	2 29 44.14		−4 55 04.2						19.90	20.11	Gb	[9]
7	2 29 47.38	0.163	−8 03 01.91	1.23	365	270	39	0.734				[11]
	2 29 47.52	0.02	−8 03 01.5	0.3	1400	100.7	3.4					[10]
	2 29 47.67		−8 03 01.0						<21.	21.52	Gb	[9]
8	2 30 19.151	0.140	−4 38 43.39	1.07	365	300	26	0.914				[11]
	2 30 19.27	0.02	−4 38 45.6	0.3	1400	87.8	2.9					[10]
	2 30 20.75		−4 38 44.6						<21.	22.2	Gb	[9]
9	2 30 25.08	0.023	−6 59 04.54	0.27	365	4055	78	0.775				[11]
	2 30 25.2	0.2	−6 59 04	3	408	3960	130					[15]
	2 30 25.10	0.02	−6 59 04.0	0.3	1400	1431.5	46.8					[10]
	2 30 25.33		−6 59 06.9						19.13	19.6	Gb	[9]
10	2 30 47.545	0.053	−3 34 05.28	0.22	365	2107	52	1.157				[11]
	2 30 47.1	0.2	−3 34 07	4	408	2010	70					[15]
	2 30 48.08	0.02	−3 34 05.4	0.3	1400	444.7	14.6					[10]
											EF	[9]
11	2 31 00.502	0.138	−7 26 43.63	1.90	365	493	68	2.08				[11]
	2 31 00.63	0.03	−7 26 40.5	0.4	1400	42.5	1.5					[10]
											EF	[9]
12	2 31 26.582	0.146	−5 20 57.99	1.13	365	272	24	0.995				[11]
	2 31 26.98	0.02	−5 20 56.1	0.4	1400	71.4	2.4					[10]
											EF	[9]
13	2 31 42.670	0.135	−6 17 09.05	1.16	365	338	30	0.894				[11]
	2 31 42.77	0.02	−6 17 07.9	0.3	1400	101.6	3.3					[10]
											EF	[9]
14	2 31 52.140	0.185	−5 36 42.25	1.40	365	251	29	1.259				[11]
	2 31 51.66	0.03	−5 36 43.7	0.4	1400	46.2	1.4					[10]
											EF	[9]
15	2 31 54.328	0.164	−6 58 34.55	2.86	365	714	78	1.4				[11]
	2 31 53.94	0.02	−6 58 25.6	0.3	1400	107.9	3.4					[10]
											EF	[9]
16	2 32 30.032	0.133	−7 49 24.08	1.11	365	337	33	0.966				[11]
	2 32 30.21	0.02	−7 49 25.2	0.3	1400	91.9	3.0					[10]
	2 32 30.35		−7 49 24.0						19.62	19.94	Gb	[9]
17	2 32 36.240	0.019	−4 15 09.78	0.19	365	4342	61	0.777				[11]
	2 32 36.5	0.2	−4 15 09	3	408	4060	90					[15]
	2 32 36.29	0.02	−4 15 09.8	0.3	1400	1528.1	48.0					[10]
	2 32 36.65		−4 15 10.0						16.00	16.29	Gb	[9]

Table. (Contd.)

1	2	3	4	5	6	7	8	9	10	11	12	13
18	2 33 26.708	0.099	−8 16 43.82	0.77	365	500	38	1.00				[11]
	2 33 26.81	0.02	−8 16 48.4	0.3	1400	129.5	4.1					[10]
	2 33 26.91		−8 16 47.4						<21.	22.08	Gb	[9]
19	2 33 31.69	0.03	−3 04 28.0	0.5	1400	37.8	1.6	<1.3				[10]
	2 33.31.6		−3 04 28.6						18.47	21.15	Gr	[9]
20	2 33 34.806	0.096	−3 03 13.16	0.82	365	441	49	1.5				[11]
	2 33 34.81	0.02	−3 03 12.7	0.4	1400	59.7	2.0					[10]
											EF	[9]
21	2 34 39.461	0.054	−4 01 25.17	0.47	365	824	56	1.05				[11]
	2 34 39.39	0.02	−4 01 25.6	0.3	1400	199.5	6.3					[10]
											EF	[9]
22	2 35 01.891	0.199	−7 27 19.60	1.46	365	231	30	0.656				[11]
	2 35 01.57	0.02	−7 27 21.6	0.3	1400	95.6	2.9					[10]
											EF	[9]
23	2 35 45.091	0.084	−6 41 46.96	0.76	365	693	74	0.938				[11]
	2 35 45.15	0.02	−6 41 49.9	0.3	1400	196.4	5.9					[10]
	2 35 45.29		−6 41 48.0						19.47	19.49	Gb	[9]
24	2 35 47.659	0.030	−3 43 15.85	0.25	365	1370	28	1.006				[11]
	2 35 47.7	0.2	−3 43 16	4	408	1340	50					[15]
	2 35 47.63	0.02	−3 43 16.2	0.3	1400	354.2	10.6					[10]
											EF	[9]
25	2 35 53.431	0.135	−6 29 14.51	0.63	365	831	72	1.06				[11]
	2 35 54.32	0.02	−6 29 15.4	0.3	1400	199.5	6.6					[10]
	2 35 54.23		−6 29 15.9						19.10	21.29	Gr	[9]
26	2 36 04.768	0.112	−4 45 38.62	0.85	365	335	24	0.846				[11]
	2 36 04.81	0.02	−4 45 37.9	0.3	1400	107.5	3.6					[10]
											EF	[9]
27	2 36 25.480	0.091	−3 08 02.90	0.69	365	425	24	0.906				[11]
	2 36 25.58	0.02	−3 08 04.1	0.3	1400	135.7	4.1					[10]
											EF	[9]
28	2 38 08.34	0.092	−7 36 06.49	0.79	365	645	0.71	0.849				[11]
	2 38 08.33	0.02	−7 36 07.3	0.3	1400	206.5	6.5					[10]
											EF	[9]
29	2 38 26.161	0.134	−5 17 32.00	0.97	365	349	28	0.286				[11]
	2 38 26.33	0.02	−5 17 31.7	0.3	1400	237.6	7.1					[10]
	2 38 26.36		−5 17 30.9						18.75	19.34	Q?	[9]
30	2 38 37.311	0.067	−8 28 09.22	0.53	365	640	31	−.275				[11]
	2 38 37.0	0.3	−8 28 16	4	408	840	40					[15]
	2 38 37.34	0.02	−8 28 09.4	0.03	1400	926.1	29.2					[10]
	2 38 37.48		−8 28 09.4						8.48	9.37	Gb	[9]
31	2 39 05.66	0.057	−4 31 09.31	0.57	365	904	57	0.792				[11]
	2 39 05.62	0.02	−4 31 09.7	0.3	1400	311.7	9.8					[10]
	2 39 06.12		−4 31 08.5						18.95	19.63	Gb	[9]
32	2 39 09.322	0.029	−7 00 18.15	0.29	365	2787	105	0.942				[11]
	2 39 09.5		−7 00 13	4	408	2490	90					[15]
	2 39 09.35	0.02	−7 00 17.9	0.3	1400	785.7	24.7					[10]
											EF	[9]
33	2 39 11.098	0.106	−4 02 29.93	1.00	365	496	53	1.22				[11]
	2 39 11.52	0.03	−4 02 25.8	0.4	1400	37.8	1.6					[10]
											EF	[9]
34	2 39 27.198	0.226	−6 19 56.10	1.35	365	316	56	1.086				[11]
	2 39 26.84	0.02	−6 19 59.0	0.3	1400	73.6	2.6					[10]
											EF	[9]
35	2 39 52.452	0.142	−4 21 48.57	1.06	365	317	28	0.944				[11]
	2 39 52.40	0.02	−4 21 47.3	0.3	1400	89.1	2.9					[10]
											EF	[9]

more than one galaxy. Additional observations with higher resolution are required. In addition, the NVSS coordinates are in good agreement with the coordinates of a bright red galaxy for which the redshift can be measured. Object no. 19 was also precisely identified with a red 18.47^m galaxy for which z can be measured.

4. CONCLUSION

(1) Strong radio sources with mean spectral index $\alpha_{mean} = 0.92 \pm 0.15$ are identified with faint blue galaxies (20.27 ± 1.66^m) with a mean optical size $5.7 \pm 2.2''$. The mean statistical redshift of this group of galaxies is $z = 0.1$–0.4. Using a Hubble constant $H = 100$ km s^{-1} Mpc, we find that the sizes of the galaxies are 8 to 30 kpc.

(2) The group of radio objects that were not identified with any optical counterparts have mean spectral index 1.1 ± 0.3. This may indicate that we are dealing here with more distant and optically faint galaxies at $z > 1.0$.

(3) The unidentified radio sources are, on average, a factor of 1.5 weaker than identified sources. However, these sources are still strong enough for radio observations with resolution 2–3$''$. Such observations are of considerable interest for refinement of the source coordinates and estimation of the size of the emitting region. Moreover, these observations could help elucidate whether the radio emission is related to the galactic coronas or to active nuclei and provide insight into the problem of galaxy formation.

ACKNOWLEDGMENTS

REFERENCES

1. E. Chavira, Rev. Mex. Astron. Astrofis. **7**, 109 (1989).
2. G. Haro, Bol. Obs. Tonantzintla Tacubaya **2** (14), 8 (1956).
3. A. Serrano, O. Cardona, E. Chavira, *et al.*, Preprint No. 116 (St. Petersburg, 1996).
4. E. Chavira, O. V. Kiyaeva, N. M. Lipovka, *et al.*, Astron. Astrophys. Trans. **10**, 161 (1996).
5. H. Butcher and A. Oemler, Jr., Astrophys. J. **219**, 18 (1978).
6. W. J. Couch and R. M. Sharoles, Mon. Not. R. Astron. Soc. **229**, 423 (1987).
7. O. Cardona, E. Chavira, and N. M. Lipovka, *Proc. of the Meeting "The Universe as Seen by ISO,"* 1998 (htth://www.iso.vilspa.esa.es/meetings/paris/proceedings/).
8. L. Fullmer and C. Lonsdale, *Catalog of Galaxies and Quasars Observed in the IRAS Survey. Version 2* (1989).
9. M. Irwin, http://www.ast.cam.ac.uk/@apmcat/ (1998).
10. J. J. Condon, W. D. Cotton, E. W. Greisen, *et al.*, *The NRAO VLA Sky Survey*, http://www.nrao.edu (1996).
11. J. N. Douglas, F. N. Bash, F. A. Bozyan, *et al.*, Astron. J. **111**, 1945 (1996).
12. O. V. Verkhodanov, S. A. Trushkin, H. Andernach, *et al.*, *Astronomical Data Analysis Software and Systems VI* ASP Conf. Ser., **125**, 322 (1997).
13. Yu. N. Pariĭskiĭ, N. S. Soboleva, A. V. Temirova, *et al.*, Preprint No. 121 (St. Petersburg, 1997).
14. Yu. N. Pariĭskiĭ, W. M. Goss, A. I. Kopylov, *et al.*, Bull. Spec. Astrophys. Obs. **40**, 5 (1996).
15. M. J. Larg, B. Y. Mills, A. G. Little, *et al.*, Mon. Not. R. Astron. Soc. **194**, 693 (1981).

Translated by A. Serber

The Luminosity Function of the Cluster Palomar 1—Testing a New Technique

A. F. Seleznev[1], G. Carraro[2], G. Piotto[2], and A. Rosenberg[3]

[1]*Astronomical Observatory, Ural State University, pr. Lenina 51, Ekaterinburg, 620083 Russia*

[2]*Dipartimento di Astronomia, Università di Padova, vicolo dell'Osservatorio 5, I-35122 Padova, Italy*

[3]*Telescopio Nazionale Galileo, vicolo dell'Osservatorio 5, I-35122 Padova, Italy*

Received January 20, 1999

Abstract—The luminosity function of the globular cluster Palomar 1 is determined together with its confidence interval by applying an adaptive kernel estimator to data from the Isaac Newton Telescope. The luminosity function of Palomar 1 has two minima in the *V* band and one in the *I* band. The cluster core contains a relatively high fraction of bright stars, indicative of mass segregation. © *2000 MAIK "Nauka/Interperiodica"*.

1. INTRODUCTION

Palomar 1 is a very faint and poorly populated globular cluster. According to the catalog of Webbink [1], it is located at a heliocentric distance of 13.7 kpc and a Galactocentric distance of 20.3 kpc, and lies 4.5 kpc above the Galactic plane. It is the position of Palomar 1 in the Galaxy that led to its classification as a globular cluster.

Rosenberg *et al.* [2] performed a detailed analysis of Palomar 1 using deep *V* and *I* CCD images ($V_{lim} \approx 24.5^m$) obtained with the 2.5-m Isaac Newton Telescope. They estimated the color excess of the cluster, $E(V - I) = 0.20^m \pm 0.04^m$, and refined its distance modulus, $(m - M)_m = 15.25^m \pm 0.25^m$. These results indicate a Galactocentric distance of 17.3 ± 1.6 kpc and a distance from the Galactic plane of 3.7 ± 0.4 kpc. Comparison of the color–magnitude diagram of Palomar 1 with theoretical isochrones yielded an age between 6.3 and 8 Gyr, making it the youngest Galactic globular cluster identified thus far.

Rosenberg *et al.* [2] discuss the nature of Palomar 1 and conclude that it is a globular cluster. Both the position of the cluster in the Galaxy and its structural properties support this conclusion (the King concentration parameter [3] is $c = 1.6$, well above typical values for open clusters [2]). Rosenberg *et al.* [2] assigned Palomar 1 to a small group of relatively young Galactic globular clusters with metallicities [Fe/H] $\approx$ –0.6, which includes Palomar 12, Rup 106, Arp 2, Terzan 7, and IC 4499.

The luminosity and mass functions (LF and MF, respectively) of Palomar 1 were also obtained in [2] separately for the cluster core ($r = 30''$) and halo ($30'' < r < 270''$). The differences between the two LFs provided evidence for mass segregation. The LF was calculated using the classical histogram method of com-bining stars into 1^m bins. The overall LF consisted of five data points, preventing analysis of smaller-scale features.

In the current paper, we use the observational data of [2] to perform a more detailed analysis of the LF of Palomar 1. We use a nonparametric method for the estimation of distribution functions, referred to as an adaptive kernel estimator, described by Silverman [4]. Seleznev [5] suggested that this method could be used to estimate the LFs and MFs of star clusters from data obtained with large telescopes with relatively small fields of view and used kernel function methods to estimate MFs in terms of several star cluster models. Here, too, we analyze the potential of the new technique for extracting cluster LFs from observations.

2. BRIEF DESCRIPTION OF THE OBSERVATIONAL DATA

The data were obtained on November 8, 9, and 10, 1994 on the Isaac Newton 2.5-m Telescope of the Roque de los Muchachos Observatory on La Palma (Canary Islands, Spain), using a 1242×1152 EEV CCD. The CCD scale was 0.54″/pixel, and the field of view was 11.2×10.3 arcmin^2.

The resulting catalog contains the Cartesian coordinates (in arcmin) and *V* and *I* magnitudes for 1540 stars within a field centered on the cluster, as well as the coordinates and *V* and *I* magnitudes for 1251 stars in a neighboring background field, slightly overlapping ($\approx$1 arcsec) with the central field. The fields cover a modest area ($\approx$1′). The limiting magnitude is $V_{lim} \approx 24.5^m$. According to [1], the cluster has a limiting radius of 19.9 pc, which corresponds to an angular radius of

5 arcmin. It follows that nearly the entire cluster falls within the first field.

3. THE CONFIDENCE INTERVAL FOR THE ESTIMATED LUMINOSITY FUNCTION

A detailed description of the application of the kernel function method to estimating distribution functions can be found in [4, 5]. To determine the confidence interval for the resulting LF, we used the method briefly described in [6].

In this method, the estimated LF $\hat{f}(V)$ is used to obtain a sufficiently large number of secondary quasi-random samples of V (or I) values distributed as $\hat{f}(V)$. General considerations suggest that the sizes of these secondary samples should be equal to the size of the initial sample. We generated our secondary samples using the Neumann algorithm described by Sobol' [7]. We then obtained for each secondary sample a new estimate of the distribution function, $\hat{f}_{si}(V)$, where $i = 1, \ldots, n$ and n is the number of secondary samples. We estimated $\hat{f}_{si}(V)$ using the same adaptive kernel method with the same kernel halfwidth, $h = 0.3$, as for the primary LF. We determined for each LF $\hat{f}(V)$ the mean $\hat{f}_{si}(V)$ secondary estimate $\overline{\hat{f}_s(V)}$ and its dispersion:

$$\overline{\hat{f}_s(V)} = \frac{1}{n}\sum_{i=1}^{n} \hat{f}_{si}(V),$$

$$\sigma_f^2 = \frac{1}{n-1}\sum_{i=1}^{n} [\hat{f}_{si}(V) - \overline{\hat{f}_s(V)}]^2.$$

Numerical simulations showed the variance σ_f to depend only slightly on the number of secondary samples. We therefore adopted $n = 20$ in all cases. Figure 1 shows the estimated LF for the central field [within $r = 30''$ from the cluster center $(0, 0)$]. The solid curve with large dots shows the initial LF estimate; the solid curve without dots, the mean secondary LF estimate averaged over the 20 secondary samples; and the solid curves with small dots, the $\pm 1\sigma_f$ confidence interval. Because σ_f corresponds to the mean secondary LF estimate, the edges of the confidence interval are not symmetric about the initial LF estimate.

Following [5], we always normalize the LF to the number of stars in the field studied:

$$\int_{V_{min}}^{V_{max}} f(V)dV = N.$$

The dimensions of the LF are then $[f] = 1$ star/magn.

According to [6], this technique for estimating the confidence interval for a LF takes into account all possible error sources, including fluctuations due to the finite
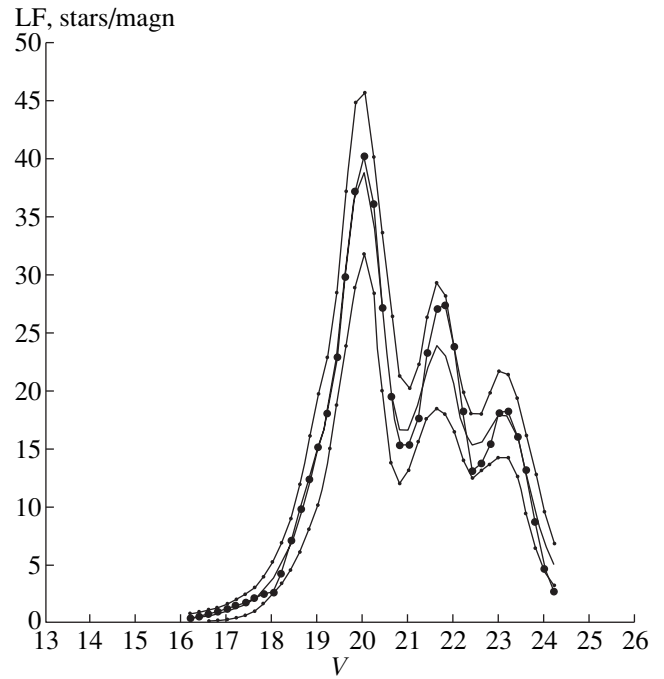
Fig. 1. LF for the central field of Palomar 1 (within $r = 30''$) estimated with smoothing parameter (kernel halfwidth) $h = 0.3$. The solid curve with large dots shows the initial LF estimate; the solid curve without dots, the mean secondary LF estimate averaged over 20 secondary samples; and the solid curves with small dots, the $\pm 1\sigma_f$ confidence interval.
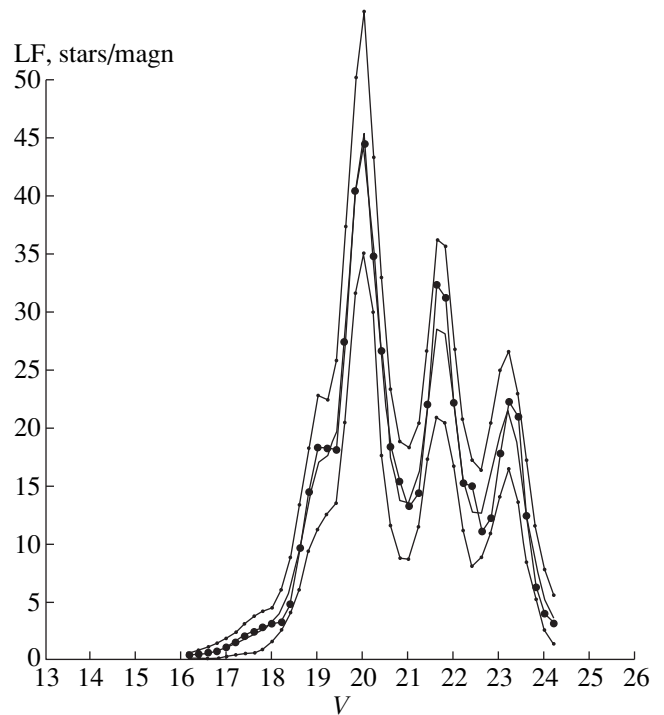
Fig. 2. LF for the central field of the cluster (within $r = 30''$) estimated with smoothing parameter $h = 0.2$. Notation is the same as in Fig. 1.
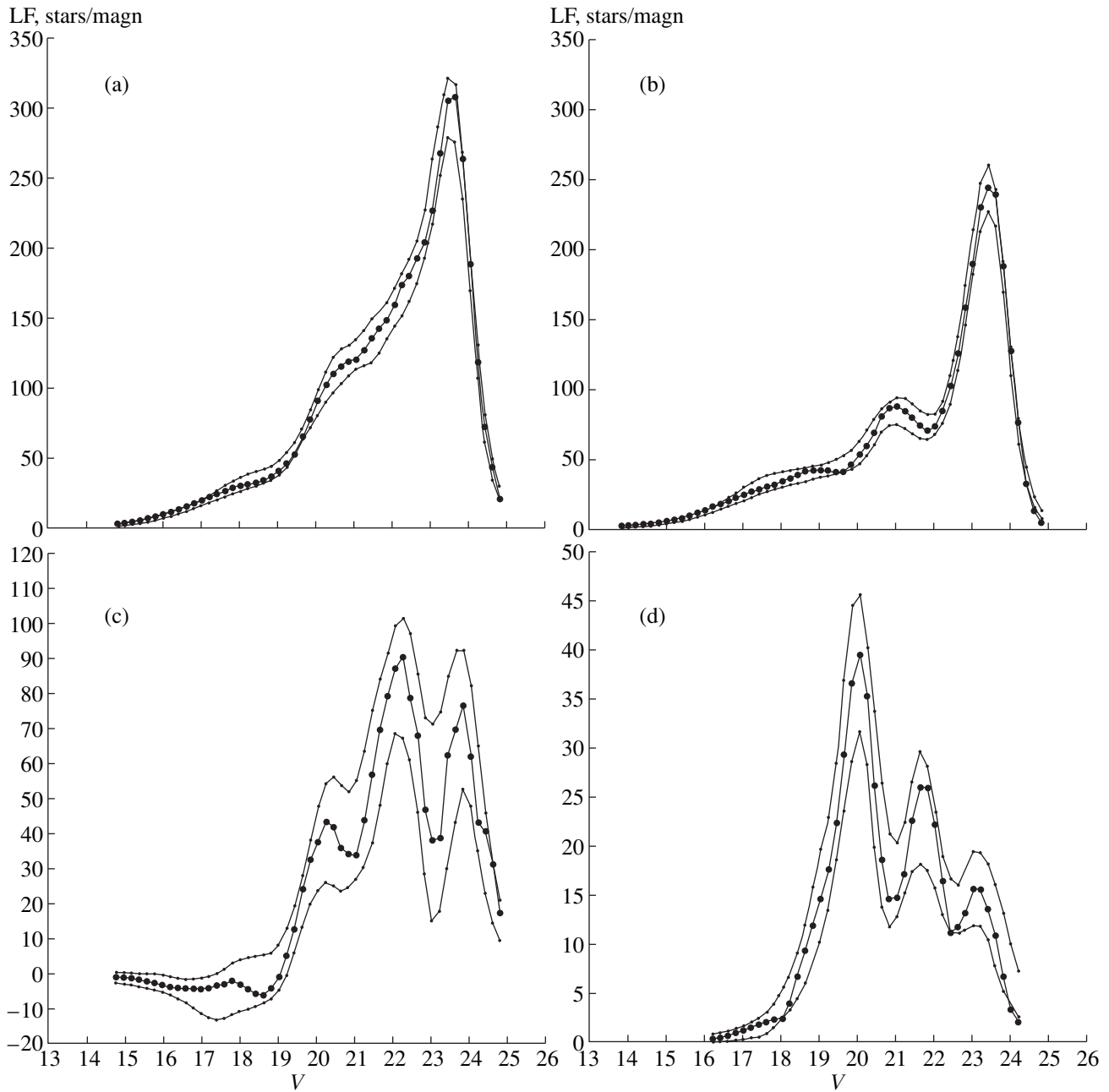
Fig. 3. Estimated *V* LFs of Palomar 1 for: (a) a ring with radii $r \in (30''; 270'')$ in the cluster field; (b) a ring of the same size in the comparison field; (c) the halo of Palomar 1 (inside the ring; background subtracted), and (d) the core of Palomar 1 (background subtracted). The solid line with large dots represents the estimated LFs, and the solid lines with small dots represent the confidence region of width $\pm 1\sigma_f$.

size of the initial sample and the bias due to the smoothing effect of the kernel function. Merritt and Tremblay [6] also point out that the resulting confidence interval does not correspond to the unknown distribution function but to the nonparameteric estimate. However, they believe that the confidence interval of the unknown function *f* is approximately the same as that of the estimate $\hat{f}(V)$, provided that the smoothing parameter *h* (the kernel halfwidth) is chosen correctly.

We investigated the dependence of the confidence interval on the kernel halfwidth. Recall that we adopted $h = 0.3$ in all estimates. We performed a number of experiments estimating the LF with $h = 0.1, 0.2, \ldots, 0.7$. The resulting maximum σ_f monotonically decreases with *h*, from 17.5 for $h = 0.1$ to 3.5 for $h = 0.7$ (while the degree of smoothing of the LF strongly increases). This is somewhat at variance with the results of Silverman [4], who gives formulas for the "optimum" *h* based on minimizing the integrated mean square error of the esti-
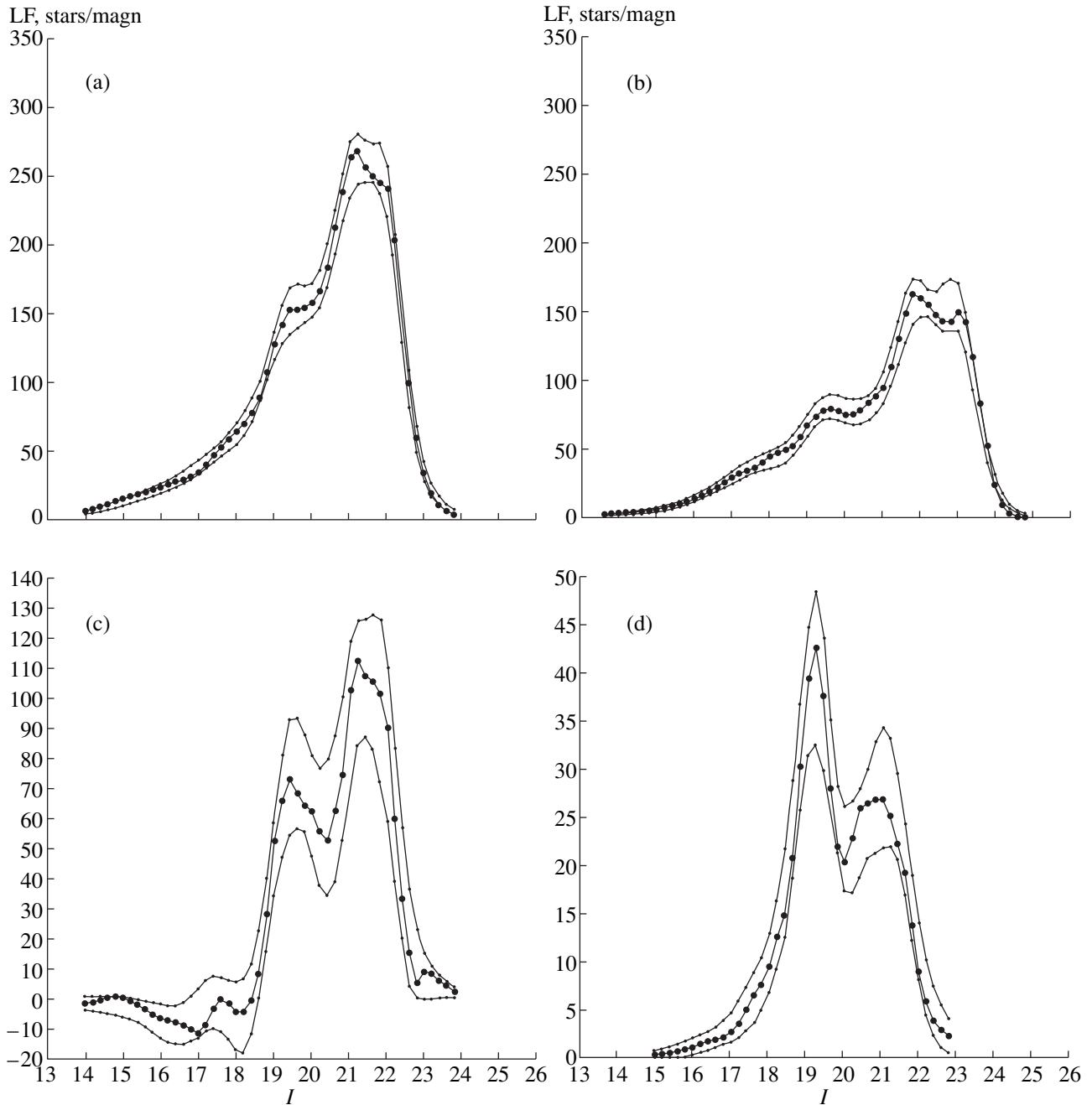
Fig. 4. Same as in Fig. 3 for the *I* LF.

mated distribution function. Silverman [4] found no minimum in the case of a LF. However, the significance of LF features was highest with $h = 0.2$. We used the ratio of the difference between the first LF maximum and first LF minimum to the maximum dispersion σ_f as a measure of this significance. Figure 2 shows the LF for a circular field of radius $r = 30''$ centered on the cluster and the corresponding confidence interval for $h = 0.2$.

4. LUMINOSITY FUNCTIONS OF PALOMAR 1. RESULTS AND DISCUSSION

We estimated the LFs for fields in Palomar 1 with various shapes and sizes.

(1) A circle with $r = 30''$ centered on the cluster [(0, 0); here and below, the coordinates are given in arcmin, in accordance with the initial catalog]. As comparison fields, we selected five background-field circles of the same radius centered on the coordinates (10.5, –0.5),
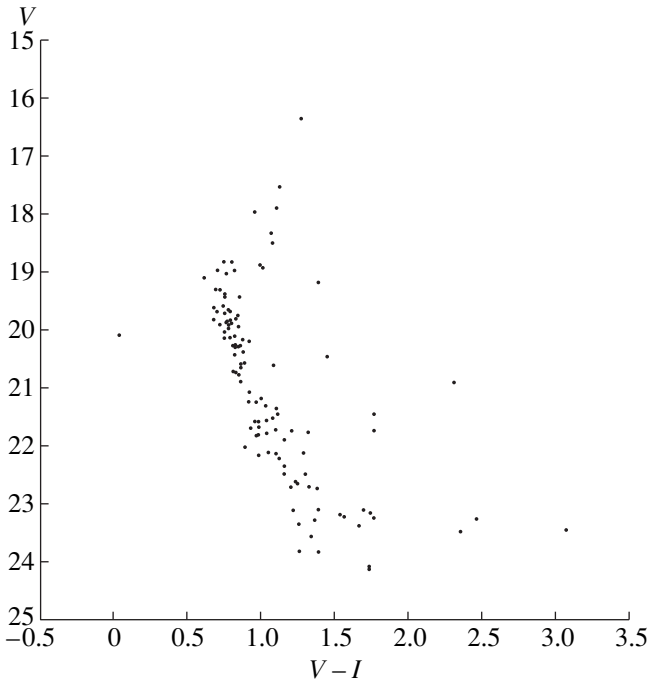
Fig. 5. Color–magnitude diagram for Palomar 1.

(8.2, 2), (12.6, 2), (8.2, –3), and (12.6, –3). The area of each circle is 0.79 arcmin^2.

(2) A ring with inner and outer radii $r \in$ (30″; 270″], also centered on the cluster. We used another such ring centered on (10.5, –0.5) as a comparison field. (The size of the ring prevented use of more than one comparison field). The outer radius of the ring is slightly greater than the limiting radius of the cluster indicated by Webbink [1]. The ring area is 62.83 arcmin^2.

We obtained LF estimates for other fields; however, our final choice was oriented toward facilitating a comparison of our results with those of Rosenberg *et al.* [2]. The first and second fields virtually coincide with the cluster core and halo, respectively. Figures 3 and 4 show the results obtained for the *V* and *I* filters. Figures 3a and 3b show the LF for the rings located in the cluster (939 stars) and background field (669 stars). The solid curve with large dots shows the estimated LF and the solid curves with small dots, the ±1σ$_f$ confidence intervals.

Figure 3c shows the Palomar 1 LF for the ring field, i.e., for the cluster halo. The number of stars in the ring is 939 – 669 = 270. We calculated the square of the halo LF confidence interval as the sum of the squares of the cluster and background confidence intervals. We took the halo LF to be the difference between the estimated cluster and background LFs (in accordance with [5]). Unfortunately, the confidence interval in Fig. 3c is very wide, making it impossible to prove the significance of the LF minima. The reason is that the LF for the cluster halo is the difference of two large quantities. The relative error of each of these quantities is small (see Figs. 3a

and 3b); however, the relative error of the difference (which is small in absolute value) is very large (Fig. 3c). This large increase of the relative error of the LF estimate imposes fundamental limitations on studies of the LFs of clusters as a whole, especially open clusters, whose LFs are comparable to those of the corresponding background fields. From this point of view, scanning of small cluster areas can provide more trustworthy information about their LFs.

Figure 3d shows the LF for the core of Palomar 1 calculated by subtracting the mean LF averaged over five comparison fields from the estimated cluster-field LF (Fig. 1). The number of stars in the cluster core field is 119 – 8 = 111. We calculated the mean LF for the background fields as a weighted average with weights inversely proportional to the mean squared errors of the individual LF estimates. We took the square of the confidence interval to be the sum of the squared error of the cluster LF and the mean squared error of the weighted average of the background LFs.

A comparison of Fig. 3d and Fig. 1 clearly shows that taking into account the background contribution has virtually no effect on the LF for the cluster core. The minima in the LF have a confidence level of ~1.8 for $h = 0.2$, and can therefore be considered rather significant (~93%).

Figure 4 shows the *I* LF of Palomar 1. The sequence of plots is the same as for the *V* LF shown in Fig. 3. A comparison of the Palomar 1 LFs shown in Figs. 3c, 3d, 4c, and 4d leads us to the following conclusions.

First, the *V* LF exhibits two minima, whereas the *I* LF has only one. The first minimum of the *V* LF corresponds to about $V \approx 21^m$ and is rather conspicuous in the *V*, *V–I* color-magnitude diagram for the cluster core (Fig. 5). The significance of this minimum is ≈93%. The second minimum corresponds to about $V \approx 22.5^m - 23^m$ and is also highly significant, though less conspicuous.

Second, as is evident from a comparison of the LFs for the cluster core and halo, the former is characterized by a higher fraction of bright stars. This indicates mass segregation, since nearly the entire LF is determined by cluster main-sequence stare (Fig. 5).

The comparison field contains a higher fraction of bright stars, making the cluster LF negative in the intervals $V \in$ [14.8^m, 19^m] and $I \in$ [14^m, 18.4^m]. The LF cutoff at the faint end is due to the fact that the incompleteness of the catalog increases toward the limiting magnitude. This is confirmed by the fact that the cluster and background LFs behave in the same way at their faint ends (Figs. 3a, 3b, 4a, and 4b).

It is desirable to have a minimum of two comparison fields located symmetrically about the cluster center in order to obtain a more statistically significant LF estimate for the cluster. This would make it possible, in particular, to exclude possible background star-density gradients across the cluster.

In conclusion, we summarize the advantages of kernel-function methods over the histogram technique. First, the kernel-function method yields continuous distribution functions [4, 5]. Second, the form of the estimated distribution function depends only on the kernel width, whereas the form of the histogram depends on both the width of the bin and the initial bin location [4]. Third, kernel-function methods allow estimation of the confidence interval for the resulting distribution function. Fourth, kernel-function distribution-function estimates are free of binning bias [8].

The kernel-function method allowed us to identify statistically significant features in the LF of Palomar 1 and confirm the presence of mass segregation in this cluster. These results testify to the value of this new technique for studies of star-cluster luminosity functions.

REFERENCES

1. R. F. Webbink, in *IAU Symp. 113: Dynamics of Star Clusters* (Reidel, Dordrecht, 1985), p. 541.

2. A. Rosenberg, I. Saviane, G. Piotto, *et al.*, Astron. J. **115**, 648 (1998).

3. I. R. King, Astron. J. **71**, 64 (1966).

4. B. W. Silverman, *Density Estimation for Statistics and Data Analysis* (Chapman & Hall, London, 1986).

5. A. F. Seleznev, Astron. Zh. **75**, 180 (1998).

6. D. Merritt and D. Tremblay, Astron. J. **108**, 514 (1994).

7. I. M. Sobol', *Monte Carlo Methods* (Nauka, Moscow, 1985).

8. P. N. Kholopov, *Star Clusters* (Nauka, Moscow, 1981).

Translated by A. Dambis

A Sky Survey at 102.5 MHz:
Radio Sources at Declinations 27.5°–33.5° and 67.5°–70.5°

R. D. Dagkesamanskiĭ, V. A. Samodurov, and K. A. Lapaev

Pushchino Radio Astronomy Observatory, Astro Space Center, Lebedev Physical Institute, Moscow, Russia

Received December 24, 1998

Abstract—The results of observations on the Large Phased Array of the Lebedev Physical Institute made as part of a survey of the northern sky at 102.5 MHz are reported. Survey source lists for the declination ranges 27.5°–33.5° and 67.5°–70.5° are given, together with their coordinates, flux densities, and identifications with 4C objects. In total, there are 920 sources with flux densities $S_{102.5} \geq 3.0$ Jy in the two zones, which cover 0.73 star. The observing and data-reduction methods are described, and the reliability and completeness of the catalog are estimated. © *2000 MAIK "Nauka/Interperiodica"*.

1. INTRODUCTION

In recent years, there has again been a growth in interest in low-frequency observations in radio astronomy. For example, the VLA (USA) and WSRT (Netherlands) aperture synthesis systems, originally intended for work at centimeter wavelengths, have recently begun to be used at meter wavelengths as well. In the last ten years, the 6C [1–6], 7C [7–10], and 8C [11, 12] Cambridge low-frequency surveys, Texas catalog at 365 MHz [13], and Miyun catalog at 232 MHz [14] have been published. Finally, the new GMRT (India) multielement, meter-wavelength, radio telescope is approaching completion and can be expected to open excellent opportunities for investigations of radio sources at meter wavelengths with high angular resolution. Of course, this has not happened by chance: high quality observations at meter and long decimeter wavelengths are very important for many questions concerning the formation and evolution of nonthermal radio sources.

In the case of Galactic supernova remnants, such observations are key for studies of the final stages of evolution of these objects and their interaction with the circumstellar gas. Observations at low frequencies are also very useful for investigations into the nature of giant looplike structures that have been detected against the Galactic radio background emission. Such observations are also important in studies of the radio halos of galactic clusters or of normal spiral galaxies.

The objects detected in low-frequency observations of powerful extragalactic radio sources are, as a rule, so-called kiloparsec jets and still more extended components (lobes), whose sizes often exceed the typical sizes of optical galaxies, i.e., the region containing most of the stellar population of a galactic system. In most cases, the extended lobes are essentially hugh res-

ervoirs of energy ($E_{\rm tot} > 10^{60}$ erg) accumulated over millions or even tens of millions of years of activity in the galactic nucleus. One of the characteristic properties of these extended extragalactic sources is the isotropy of their radiation. In contrast to the radio emission from the nuclei of active galaxies, the observed luminosity of these lobes is virtually the same in all directions. This circumstance substantially simplifies statistical analysis of the observational data, in particular, construction of the radio luminosity function, interpretation of radio source counts, etc.

Here, we report the first results of observations carried out in 1991–1993 on the Large Phased Array of the Lebedev Physical Institute as part of a complete survey of the northern sky at 102.5 MHz. We describe the methods used to obtain and reduce the data and present a large fraction of a catalog of radio sources in declination intervals $27.5° \leq \delta \leq 33.5°$ and $67.5° \leq \delta \leq 70.5°$. In contrast to other deep surveys published over the last ten years [1–14, 17] carried out using interferometers and aperture-synthesis systems, all the observations described here were obtained on a filled-aperture antenna and contain information not only about discrete sources with comparatively small angular sizes, but also about more extended sources down to 1°. In view of their substantial extended components, such sources are usually not included in catalogs compiled based on aperture-synthesis observations.

2. OBSERVATIONS

The Large Phased Array of the Pushchino Radio Astronomy Observatory is a phased antenna grid with sizes $D_1 = 187$ m east–west and $D_2 = 374$ m north–south. The antenna beam of this transit instrument can be steered only in declination, within the meridian plane. During the survey observations, the central receiver frequency was

102.5 MHz (λ = 2.93 m). A multibeam regime made it possible to simultaneously record the signals corresponding to eight different beam positions, with the declinations of neighboring maxima separated by

$$\Delta\delta = \frac{\lambda}{D_2\cos Z}\,\text{rad} = 27'\sec Z, \qquad (1)$$

where $Z = 54°49' - \delta$ is the zenith distance corresponding to the declination δ. A beam-switching feeder tract could be used to shift the position of all beams by half of the indicated interval, i.e., by $13.5'\sec Z$. The antenna beam shape can with sufficiently good accuracy be represented in the form

$$F(\alpha, \delta)$$

$$= \frac{\sin^2\left(\pi\dfrac{D_1\cos Z}{\lambda}(\alpha - \alpha_0)\right)\sin^2\left(\pi\dfrac{D_2}{\lambda}(\delta - \delta_0)\right)}{\left[\left(\pi\dfrac{D_1\cos Z}{\lambda}(\alpha - \alpha_0)\right)\left(\pi\dfrac{D_2}{\lambda}(\delta - \delta_0)\right)\right]^2}, \qquad (2)$$

where (λ_0, δ_0) are the equatorial coordinates corresponding to the maximum of the radio telescope beam.

The observations, data recording, and "on-line" preliminary data reduction were carried out in an automated regime controlled by a Mera-125 computer. The direct output of the observations are scans obtained with the multibeam antenna beam of the Large Phased Array. Over a 25-hour session, observations with the eight neighboring beams covered a strip of sky with a width of $216'\sec Z$ in declination. The "extra" hour extending the session beyond one day was used to check for, and, in a number of cases, decrease, the effects of drifts in the zero level and the receiver amplification. Each of the strips was observed a second time but with the positions of the beams shifted by half the distance between them. In this way, we obtained information about the sky brightness distribution with discrete steps in declination equal to $0.5\Delta\delta = 13.5'\sec Z$ for an antenna beam of the form $\sin^2 X/X^2$ with the full width of its main lobe (to the zero level) equal to $54'\sec Z$. It is easy to show that this step satisfies the theorem of Kotel'nikov, so that there is no significant loss of information about the brightness distribution due to the discrete character of the measurements.

Each 25-hour session was made up of a collection of 15-s cycles. In the first 10 s of each cycle, the output voltages in each of the eight receiver channels (corresponding to the eight radio telescope beams) were read out with a frequency of 10 Hz. In the last 5 s, the Mera-125 personal computer was used to clean all the datasets from quasi-impulsive interference and determine the mean values and dispersions of the readouts. These readouts were then recorded in an observing file, after which the entire 15-s procedure was repeated. The first 15 s of each hour were divided into two short (7.5-s) analogous

cycles for recording two standard signals in order to monitor the amplification of the entire tract and receivers. Thus, the result of a single 25-h session was:

—8 × 5975 mean response values (divided into 25 datasets [239 × 8]),

—8 × 5975 response dispersions (divided into 25 datasets [239 × 8]),

—8 pairs of datasets of standard signals with 25 readouts in each ([25 × 8] datasets),

—8 pairs of dispersion datasets for the standard signals with 25 readouts in each ([25 × 8] datasets).

3. DATA REDUCTION

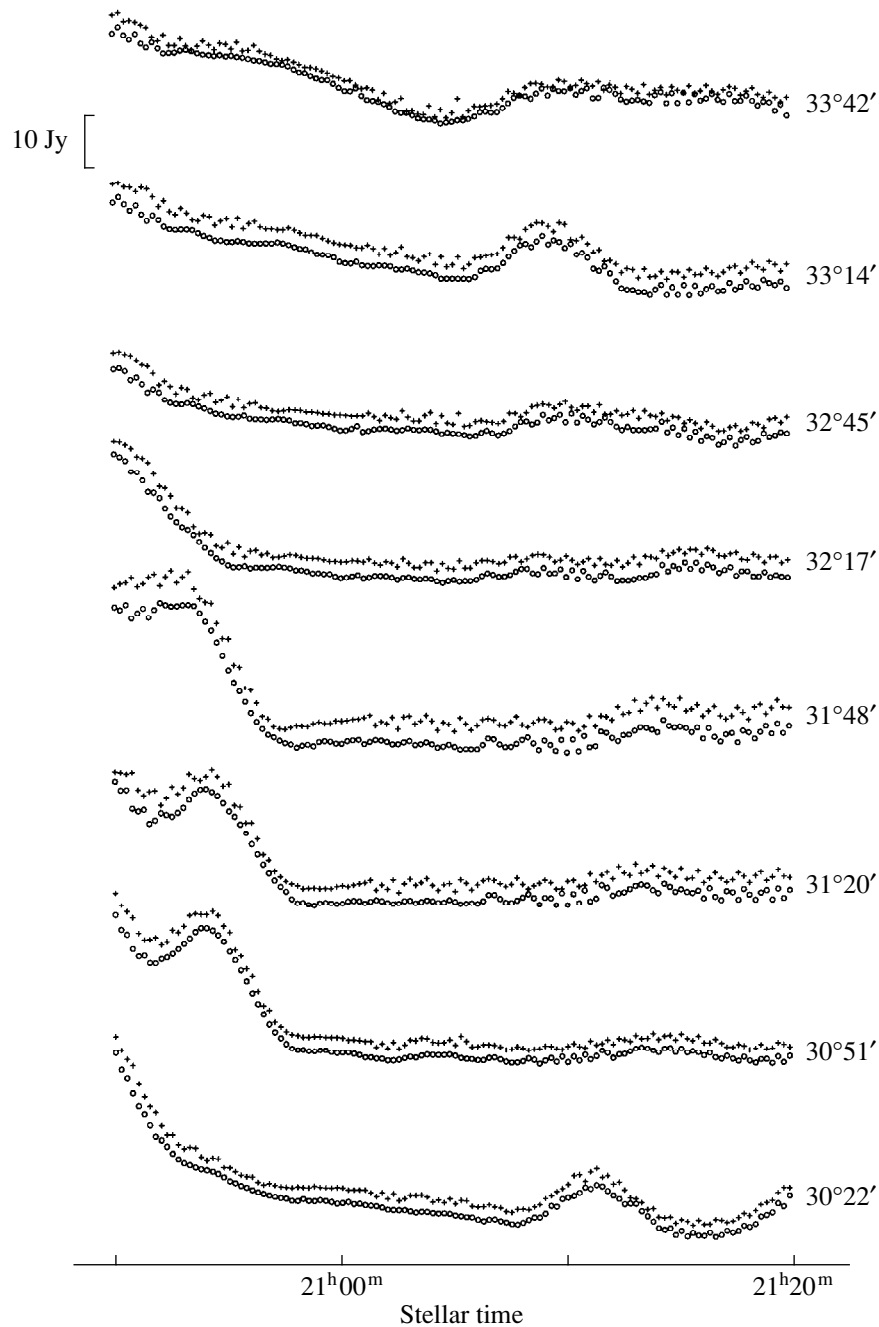We can separate the reduction of the observational data into four main stages:

(a) preliminary calibration and editing of the data;

(b) reduction of individual scans;

(c) comparison of results for neighboring scans;

(d) refinement of parameters derived for radio sources.

We will now consider each stage of the reduction in more detail.

3.1. Preliminary Calibration and Editing

As noted above, the preliminary calibration of the recordings is based on two calibration signals. The first of these (E_1) corresponds to the output voltage level when matched loads are switched on the inputs of all 256 upper-level antenna amplifiers; its magnitude was comparable to the response of the antenna to the background far from the Galactic plane. The second calibration signal (E_2) was recorded while matched loads were switched on to the inputs of the 32 intermediate-level amplifiers and in practice was close to the zero level.

Figure 1 presents an example of observations of the same area on the sky on different days. On the whole, the repeatability of the data is not bad. The observed differences between the recordings are due to errors in their preliminary calibration. Such comparisons show that the accuracy of our procedure for the preliminary calibration increases as the scatter in the "steps" (i.e., the difference $E_1 - E_2$) over the course of a day decreases. In most cases, this scatter was no more than ±10–15%; experience has shown that this corresponds to a calibration accuracy of no worse than ±7%. Employing a special procedure to select recordings with minimum scatter in their calibration signals can reduce the final relative accuracy of the calibration to roughly ±3%. It is clear that this will be reflected in the accuracy of the flux densities presented in our catalog. However, the error ascribed to the

10 Jy

33°42′

33°14′

32°45′

32°17′

31°48′

31°20′

30°51′

30°22′

21$^\mathrm{h}$00$^\mathrm{m}$ 21$^\mathrm{h}$20$^\mathrm{m}$

Stellar time

Fig. 1. Examples of recordings of the radio flux from the same area of sky; the crosses show data for October 8, 1992 and the circles for October 10, 1992.

data presented in graph five of the catalog (see below) does not include this error.

In addition to the calibration procedure, in the first stage of the analysis, we identified and excluded from subsequent processing and analysis recordings that were strongly distorted by interference. These were replaced by other recordings of the same area of sky with better quality obtained in other observing sessions. In this way, after the first data-reduction stage, the observational

data were calibrated in conditional units and cleaned of obvious defects that were clearly visible by eye.

3.2. Reduction of Individual Scans

At this stage, we produced each of the eight scans for a 25-h observing session separately, with the aim of separating out features with sizes of the order of the antenna beam and a smoother "background" component in the recordings obtained. To decrease the effect

of noise and ionospheric fluctuations, each of the recordings $X_0(\alpha)$ was passed through a "matched filter" of the form

$$
\begin{cases}
F(\alpha) = \dfrac{\sin^2\left(2\pi\dfrac{D_1\cos Z}{\lambda}\alpha\right)}{\left[2\pi\dfrac{D_1\cos Z}{\lambda}\alpha\right]^2} - C, \\[20pt]
\text{at} \quad \alpha \in \left[-\dfrac{\lambda}{2D_1\cos Z}, \dfrac{\lambda}{2D_1\cos Z}\right] \\[16pt]
F(\alpha) = 0, \quad \text{at} \quad \alpha \notin \left[-\dfrac{\lambda}{2D_1\cos Z}, \dfrac{\lambda}{2D_1\cos Z}\right].
\end{cases} \tag{3}
$$

Here, the constant C is determined from the condition

$$
\int_{-\lambda/2D_1}^{\lambda/2D_1} F(\alpha)\,d\alpha = 0. \tag{4}
$$

In this way, we formed a new dataset in the form of the convolution integral

$$
Y_0(\alpha) = X_0(\alpha)F(\alpha), \tag{5}
$$

in which the current linear background component is filtered out. Afterwards, we used a CLEAN procedure to separate out features with characteristic sizes of the order of the antenna-beam width, namely:

—In the dataset $Y_0(\alpha)$, we determined the position and amplitude A_1 of the maximum deviation from zero α_1.

—In the original dataset $X_0(\alpha)$, we subtracted the response to a point source with amplitude gA_1 at the position α_1 of the maximum deviation, forming a new dataset $X_1(\alpha)$.

—We used the dataset $X_1(\alpha)$ to construct a new convolution integral $Y_1(\alpha)$.

After this, a new maximum deviation from zero was found in the new dataset $Y_1(\alpha)$, and the procedure was repeated until the magnitude of the maximum deviation from zero became less than some specified value A_{min}. This value A_{min} was chosen to be small enough (~0.3 Jy) so that the error in the flux estimates for sources with $S_{102} \sim 3$ Jy introduced by the CLEAN procedure did not exceed 10%. The parameter g, which has a direct analogue in the classical CLEAN procedure, was, in our case, variable, and took on values from 0.3 in the first iterations to 1.0 as the amplitude A approached the limiting value A_{min}.

The list of "point sources" (δ functions) formed as a result of this modified CLEAN procedure were transformed so as to merge δ-function components separated by less than the angular resolution of the radio telescope. A specially developed "competitive" method used to merge the responses of the system to the δ function components is described in detail in [15]. In brief, this method merges the "point sources" over a series of several iterations, taking into account not only their rel-

ative positions, but also their relative flux densities. Tests of this procedure on model brightness distributions demonstrated that it is stable and that the resulting solutions are not ambiguous, even when a more usual merging procedure (see, for example, [16]) will tend to give rise to false sources in the final list. We then attempted to identify the list of δ functions obtained for each scan as a result of several iterations of the "merging" procedure, determining the declinations and flux densities for the corresponding sources.

The background component of each scan was determined after subtracting calculated point-source responses corresponding to the final list of δ functions from the original recording. The data were then smoothed in order to average out fluctuations on scales smaller than the width of the main lobe of the antenna beam.

3.3 Comparison of Results for Neighboring Scans

The reduction procedure described above was applied to both a given 25-h session and to a second 25-h session with the positions of the eight beams shifted by $\Delta\delta/2$ (see Section 2). After this, we used the results for the 16 pairs of scans separated by $13.5'\sec Z$ to identify corresponding sources in the neighboring scans. We used the relative amplitudes of the radio-telescope responses to the same source in two or more neighboring scans to derive the declination of the source and estimate its flux density. In this way, we obtained a list of detected sources, with first approximations to the source parameters in the final catalog.

3.4. Refinement of the Radio Source Parameters

To determine the final source parameters for the catalog, we fitted the resulting recordings (after subtracting the background component) with two-dimensional gaussians to refine the coordinates, flux densities, and major and minor axes of the sources. When the source dimensions corresponded to a small fraction of the antenna-beam width, or when the resulting agreement factors were only slightly different from those for point-source fits, we present in the catalog the coordinates and flux densities corresponding to the point-source fits.

The final flux-density scale was determined using observations of several relatively bright sources whose spectra have been well studied at meter wavelengths. The table presents a list of 32 calibration sources for the area with declinations in the interval 27.5°–33.5°, with the corresponding flux densities taken from the literature. Note that these sources were also observed in two sessions. When using these sources to construct the flux-density scale at 102.5 MHz, we relied on the flux densities of Kellermann [18] (presented in the table). The tie between the measured flux densities for all the sources in our catalog and the constructed scale is such that the median ratio of the flux densities in the table to those in our catalog is equal to unity. The accuracy of

Calibrator sources for declinations 27.5°–33.5° with published S 102.5 MHz values and 4C coordinates (1950.0)

Name	R.A.	Dec.	Flux, Jy
3C19	0^h 38^m 14.0^s	+32° 52.8′	19.4
3C31	1 4 42.4	+32 8.4	29.2
3C34	1 7 33.5	+31 31.2	23.4
3C41	1 23 55.3	+32 56.1	17.3
3C42	1 25 43.4	+28 46.8	18.8
3C48	1 34 49.9	+32 53.5	77.6
3C55	1 54 20.1	+28 35.8	38.0
3C67	2 21 18.3	+27 36.1	20.6
3C68.2	2 31 25.3	+31 21.6	27.5
3C92	3 37 1.0	+31 58.8	19.1
3C123	4 33 55.1	+29 34.4	323.6
3C131	4 50 11.4	+31 24.7	27.5
3C139.2	5 21 19.2	+28 10.5	28.5
3C141	5 23 27.2	+32 47.6	29.9
3C200	8 24 21.8	+29 28.9	20.2
3C210	8 55 11.7	+28 2.6	18.0
3C213.1	8 58 6.1	+29 14.0	16.2
3C234	9 58 57.1	+29 0.9	57.5
3C265	11 42 53.0	+31 50.4	35.0
3C268.2	11 58 25.8	+31 48.4	14.6
3C277.3	12 51 46.8	+27 54.0	22.4
3C284	13 8 42.4	+27 43.2	18.8
3C286	13 28 49.9	+30 45.7	29.5
3C293	13 50 3.5	+31 40.9	23.7
3C332	16 15 48.0	+32 28.6	18.2
3C341	16 26 3.1	+27 48.3	20.7
3C357	17 26 27.3	+31 48.8	18.2
3C382	18 33 13.2	+32 38.6	41.2
3C399.1	19 14 0.0	+30 13.4	21.3
3C410	20 18 3.5	+29 32.6	61.0
3C436	21 41 58.8	+27 56.3	34.7
3C441	22 3 50.4	+29 14.3	23.7

the tie of our flux scale to the scale of Kellermann is approximately 3%. As was the case for the residual relative calibration errors, this scale error is not reflected in the errors ascribed to the data (see column 5 of the catalog). Therefore, it is important to remember that our flux densities could include this systematic error.

There are substantially fewer sources with declinations 67.5°–70.5° with well studied spectra. Therefore, we decided to construct the flux density scale for the sources in this area using the data for a single reliable calibrator, namely 3C27, whose 102.5 MHz flux density we took to be 37 Jy. An additional argument in favor of this tie is that the difference between the nec-

essary calibration factors for the two areas is consistent with the expected dependence of the effective area of the radio telescope on the zenith distance.

Thus, the flux density scale for our catalog is close to that of Kellermann [18] at meter wavelengths and, as a whole, corresponds to the scale used in [17].

4. THE CATALOG OF RADIO SOURCES

We do not present the radio-source catalog here; an electronic version is accessible over the interned at the address http://astra.prao.psn.ru/SAM/WIN/catalog.htm. The catalog is comprised of two tables—one for each of the two declination intervals. These tables contain:

column 1—source number, with separate numbering for sources in each of the two declination intervals;

column 2—right ascension (h, min, s) at epoch 1950.0;

column 3—declination (deg, arcmin) at epoch 1950.0;

column 4—flux density in Jy (in the case of extended sources, this is the integrated flux density);

column 5—relative error in the flux density measurement E_{flux}, determined from the residual deviations when the calculated response is fit to the recording;

column 6, 7, and 8—angular sizes (arcmin) for the major axis, minor axis (both FWHM), and position angle of the two-dimensional gaussians fit for extended sources;

column 9—identification of sources from our catalog with objects in the 4C catalog.

5. ERROR ESTIMATES

The main source of random error in the measured coordinates and flux densities for comparatively weak sources is fluctuations due to the random distribution on the sky of even weaker sources (confusion). The rms value of these fluctuations for the Large Phased Array is usually estimated to be 1 Jy (see, for example, [19]). However, the modified CLEAN procedure used in the data reduction somewhat (by roughly a factor of two) decreases these fluctuations, since the "working lists" of δ functions derived from the recordings include "point sources" with flux densities from one to three Jy, some of which are fluctuations associated with confusion. This is also warranted by the fact that it enables us to more correctly estimate the background component. The analysis of [22] shows that taking weak sources into account makes it possible to lower the magnitude of confusion fluctuations to ~0.6 Jy. An independent experimental estimate of this value using our data yields 0.59 ± 0.05 Jy [23].

For relatively strong sources, errors due to scintillation in ionospheric inhomogeneities and inaccuracy of the tie between the amplifications for separate scans are more important. The magnitude of random fluctuations

due to system noise is much lower than the effect of confusion. This is precisely why the reduction of the data accumulation time by one-third in order to clean the input signals from interference and estimate their mean values and dispersions (see Section 2) does not decrease the final accuracy of the measured source flux densities and coordinates.

The relative flux-density errors presented in column 5 of the catalog reflect to some degree each of the possible sources of random errors. However, we must keep in mind that our estimate of the magnitude of this error should not be lower than the rms residual fluctuations associated with confusion, which are about 0.59 Jy. In addition, when comparing our flux densities with those in other catalogs, there is a possible systematic error in the ties of the data of each catalog to the flux-density scale used (as noted above, for our data, the error in the tie to the scale of Kellermann [18] does not exceed 3%).

A detailed analysis of possible errors and ways to decrease them during the data reduction are described in [23]. Here, we only note that the final relative error in the integrated flux densities is determined by the error in fitting E_{flux} (or the rms fluctuations due to confusion, if the latter exceeds SE_{flux}) and the residual calibration error discussed in Section 3.1 (about 3%); i.e.,

$$\frac{\delta S}{S} = 0.03 + \max\left\{E_{flux}; \frac{0.59}{S}\right\}. \tag{6}$$

Note that this error does not exceed the systematic error in the tie of our data to the scale of Kellermann (~3%), which must be kept in mind when comparing our data with measurements from other studies.

Figure 2 shows our 102.5-MHz flux-density measurements ($S_{102.5}$) as a function of the 102-MHz flux densities of these same sources obtained via a linear extrapolation based on their flux densities S_{80} and S_{160} from the Culgoora-3 catalog [17]. The least-squares line fit (on a logarithmic scale) indicates that there is a good correspondence of the flux density scales of the two catalogs.

The rms errors in the coordinates for sources reliably identified with objects in the 4C [20, 21] and Culgoora-3 catalogs grow somewhat as the source flux densities decrease, from $\varepsilon_\alpha = 18^s$ and $\varepsilon_\delta = 3'$ when the 102.5-MHz flux density is larger than 10 Jy to $\varepsilon_\alpha = 40^s$ and $\varepsilon_\delta = 6'$ when it is from 3 to 4 Jy. When two or more sources are located comparatively nearby on the sky (compared to the antenna-beam size), the errors in their coordinates can be even larger. Nevertheless, the resulting coordinate accuracy is sufficient to obtain trustworthy identifications for our sources with most sources from the 4C catalog.

6. COMPLETENESS AND RELIABILITY

We have included in the catalog only sources with measured flux densities at 102.5 MHz greater than 3 Jy, i.e., with flux densities exceeding the rms fluctuations
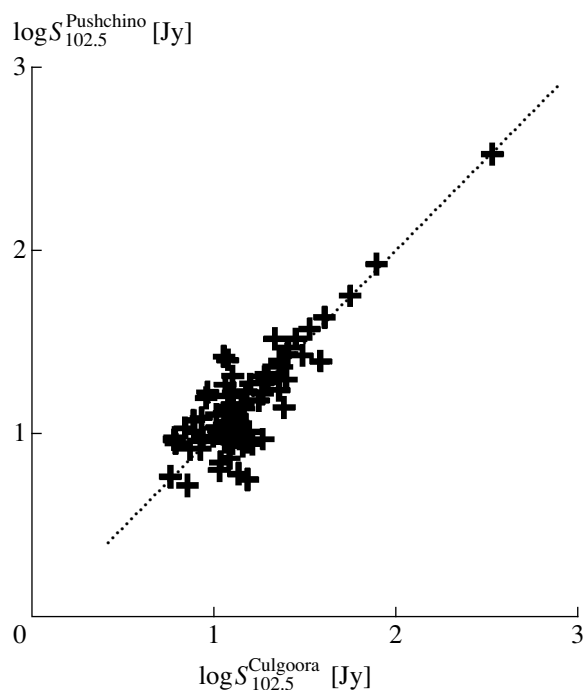

Fig. 2. Comparison of source flux densities in the Pushchino and Culgoora-3 catalogs.

due to confusion by at least a factor of three. In this case, the probability of false sources appearing in the catalog is rather small; we estimate that it does not exceed 10^{-2} for the weakest sources and 10^{-3} for sources with flux densities greater than 4 Jy. We estimate that the catalog is about 85% complete to $S_{102.5} = 3.5$ Jy and more than 97% complete to $S_{102.5} \geq 4.5$ Jy.

To a first approximation, these fairly crude *a priori* estimates obtained assuming a normal distribution for the fluctuations due to confusion are consistent with the statistics of our identifications of our catalog sources with 4C objects. Indeed, 84% of the 4C objects with declinations from 28° to 33° are identified with sources from our catalog, and about 85% of sources in our catalog with flux densities greater than 5 Jy are identified with 4C sources. Although this last value is somewhat lower than expected from the estimates presented above, this does not represent serious contradiction. In fact, when comparing identification statistics with our *a priori* estimates, we should bear in mind that some of the sources in our catalog could be relatively extended (with sizes of several arc minutes), while others have anomalously steep spectra and, therefore, are absent from the 4C catalog. In addition, like our catalog, the 4C catalog is characterized by some reliability and completeness. Taking all this into account, we believe that the statistics of mutual identification of sources in our catalog and the 4C catalog, as a whole, confirm our *a priori* estimates of the catalog's completeness.

Note also that our estimates for the completeness of the catalog and the probability of false sources appear-
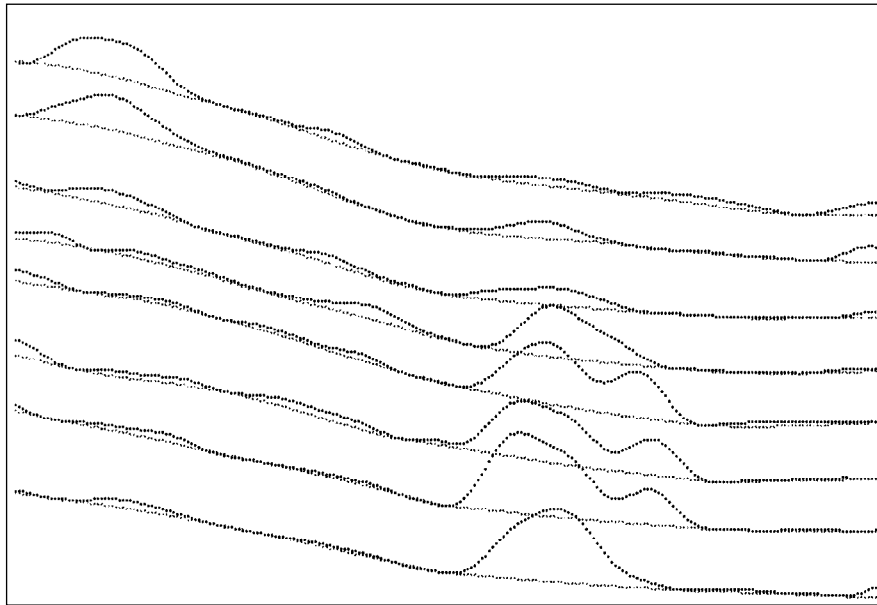
Fig. 3. Example of dividing the data into scans with background and scans with sources with sizes no more than 1.5° (the Cygnus Loop zone from observations in the eight beams; a fragment of the computer screen display during processing of the daily recordings is shown).
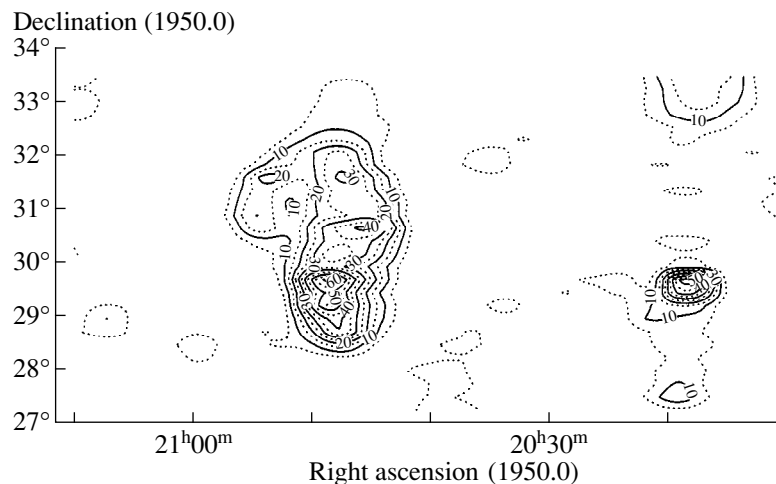
Fig. 4. A map of the Cyg Loop region. The levels of constant brightness are given in units of Jy/beam.

ing in it could be incorrect for extended sources with sizes comparable to the LPA antenna beam. The reduction procedure used can distinguish isolated sources with sizes of the order of or less than the antenna-beam size rather reliably, but in the case of more extended sources, close groups of radio sources, and small-scale fluctuations of the background, this procedure could lead to erroneous determination of the relative contribution of the sources and the background. It is obvious that all procedures connected with detailed problems in data reduction without *a priori* information are subject to such limitations to some degree.

In a number of cases, sources with sizes a factor of a few larger than the antenna beam are represented in our catalog by a collection of several closely-spaced radio sources. One example of this is the Cygnus Loop region (sources nos. 635–647 in the first table of the catalog). Figure 3 shows the appearance of part of the display screen during the procedure for separating out the contribution of sources from the background component in this region for one of the observing sessions. Figure 4 presents isophotes of this region after subtraction of the contribution of the smooth background component. A comparison of Fig. 4 with our catalog shows that the main shell structure of the Cygnus Loop is represented in our catalog as a collection of closely spaced sources whose sizes are comparable to the LPA beam. Of course, more complete information about the bright-

ness distribution in extended sources could be obtained from an analysis of the entire dataset, including the distribution of the background component and, more generally, from an analysis of the input antenna-temperature distribution. Information about the distributions of the antenna temperature and the background component of the brightness distribution will be presented in a separate paper.

ACKNOWLEDGMENTS

REFERENCES

1. J. E. Baldwin, R. C. Boysen, S. E. G. Hales, *et al.*, Mon. Not. R. Astron. Soc. **217**, 717 (1985).
2. S. E. G. Hales, J. E. Baldwin, and P. J. Warner, Mon. Not. R. Astron. Soc. **234**, 919 (1988).
3. S. E. G. Hales, C. R. Masson, P. J. Warner, *et al.*, Mon. Not. R. Astron. Soc. **246**, 256 (1990).
4. S. E. G. Hales, C. J. Mayer, P. J. Warner, *et al.*, Mon. Not. R. Astron. Soc. **251**, 46 (1991).
5. S. E. G. Hales, C. R. Masson, P. J. Warner, *et al.*, Mon. Not. R. Astron. Soc. **262**, 1057 (1993).
6. S. E. G. Hales, J. E. Baldwin, and P. J. Warner, Mon. Not. R. Astron. Soc. **263**, 25 (1993).
7. A. E. Visser, J. M. Riley, H. J. A. Roettgering, *et al.*, Astron. Astrophys., Suppl. Ser. **110**, 419 (1995).
8. E. M. Waldram, J. A. Yates, J. M. Riley, *et al.*, Mon. Not. R. Astron. Soc. **282**, 779 (1996).
9. S. J. Vessey and D. A. Green, Mon. Not. R. Astron. Soc. **294**, 607 (1998).
10. D. M. Pooley, E. M. Waldram, and J. M. Riley, Mon. Not. R. Astron. Soc. **298**, 637 (1998).
11. N. Rees, Mon. Not. R. Astron. Soc. **244**, 233 (1990).
12. S. E. G. Hales, E. M. Waldram, N. Rees, *et al.*, Mon. Not. R. Astron. Soc. **274**, 447 (1995).
13. J. N. Douglas, F. N. Bash, F. A. Bozyan, *et al.*, Astron. J. **111**, 1945 (1996).
14. X. Zhang, Y. Zheng, H. Chen, *et al.*, Astron. Astrophys., Suppl. Ser. **121**, 59 (1997).
15. V. A. Samodurov, Preprint FIAN (Lebedev Physical Institute) (in press).
16. J. A. Hogbom, Astron. Astrophys., Suppl. Ser. **15**, 417 (1974).
17. O. B. Slee, Aust. J. Phys. **48**, 143 (1995).
18. K. I. Kellermann, Astrophys. J. **140**, 969 (1964).
19. R. D. Dagkesamanskiĭ, A. G. Gubanov, A. D. Kuz'min, *et al.*, Mon. Not. R. Astron. Soc. **200**, 971 (1982).
20. J. D. H. Pilkington and P. F. Scott, Mem. R. Astron. Soc. **69**, 183 (1965).
21. J. F. R. Gower, P. F. Scott, and D. Wills, Mem. R. Astron. Soc. **71**, 49 (1967).
22. R. D. Dagkesamanskiĭ, Candidate's Dissertation in Physical and Mathematical Sciences (Moscow, 1969).
23. V. A. Samodurov, Preprint FIAN (Lebedev Physical Institute) (in press).

Translated by D. Gabuzda

The Effect of Viscosity on the Flow Morphology in Semidetached Binary Systems. Results of 3D Simulations. II

D. V. Bisikalo[1], A. A. Boyarchuk[1], O. A. Kuznetsov[2], V. M. Chechetkin[2]

[1]*Institute of Astronomy, Russian Academy of Sciences,*
ul. Pyatnitskaya 48, Moscow, 109017 Russia
[2]*Keldysh Institute of Applied Mathematics, Russian Academy of Sciences,*
Miusskaya pl. 4, Moscow, 125047 Russia
Received February 25, 1999

Abstract—We present the results of three-dimensional simulations of matter flows in semidetached binary systems with various viscosities. In low-viscosity systems, the flow structure displays the same qualitative features as in high-viscosity computations. A self-consistent solution shows the absence of a shock interaction between the stream flowing from the inner Lagrange point and the forming accretion disk (or hot spot) for any viscosity. © *2000 MAIK "Nauka/Interperiodica"*.

1. INTRODUCTION

We have studied the flow morphologies in semidetached binary systems in a number of previous papers [1–6]. In the framework of our three-dimensional numerical model, we found that the presence of rarefied intercomponent gas results in substantial variations of the structures of gaseous streams in such systems. In particular, a self-consistent solution of the problem yields no shock interaction between the stream flowing out from the inner Lagrange point L_1 and the forming accretion disk (i.e., there is no "hot spot"). However, these solutions were obtained for a relatively high disk viscosity, since the limited ability of the computers used necessitated the use of coarse grids in the computations. In terms of an α disk, the numerical viscosity corresponded to $\alpha \sim 0.5$ [5]. At the same time, the flow structure for lower viscosity is of considerable interest. This is primarily due to the fact that current models for novae explosions assume the existence of two accretion-disk states, one with low and the other with high viscosity [7–10]. These models are supported by observations (see, for example, [10, 11]).

The present study aims to analyze the general morphology of the flows in semidetached binary systems with low viscosities. We will pay the most attention to the question of whether or not the flow structure is maintained as the viscosity is decreased and, in particular, if the stream–disk interaction will remain shockless, as shown in [1, 2], for relatively high viscosities. Study of the stream–disk interaction and, accordingly, of the presence or absence of a hot spot is extremely important for interpretations of the observational data.

As in [1–6], we describe the gas flow using a system of Euler equations without including physical viscosity. The fact that only numerical viscosity is present in the model restricts the possibilities for detailed study of the problem; nonetheless, the qualitative behavior of the solution for various viscosities can be obtained. Since the numerical viscosity (for the chosen differential scheme) depends on the temporal and spatial resolution, we used a computation sequence with decreasing grid step in order to derive the dependence of the solution on the viscosity.

2. THE MODEL

We considered a semidetached binary system consisting of a donor star with mass M_1 that fills its Roche lobe and an accretor with mass M_2. The mass ratio for the components of the system was taken to be unity.

To describe the flow, we used a 3D system of gas dynamical Euler equations:

$$\frac{\partial \rho}{\partial t} + \frac{\partial \rho u}{\partial x} + \frac{\partial \rho v}{\partial x} + \frac{\partial \rho w}{\partial z} = 0,$$

$$\frac{\partial \rho u}{\partial t} + \frac{\partial (\rho u^2 + P)}{\partial x} + \frac{\partial \rho u v}{\partial y} + \frac{\partial \rho u w}{\partial z} = -\rho \frac{\partial \Phi}{\partial x} + 2\Omega v \rho,$$

$$\frac{\partial \rho v}{\partial t} + \frac{\partial \rho u v}{\partial x} + \frac{\partial (\rho v^2 + P)}{\partial y} + \frac{\partial \rho v w}{\partial z} = -\rho \frac{\partial \Phi}{\partial y} - 2\Omega u \rho,$$

$$\frac{\partial \rho w}{\partial t} + \frac{\partial \rho u w}{\partial x} + \frac{\partial \rho v w}{\partial y} + \frac{\partial (\rho w^2 + P)}{\partial z} = -\rho \frac{\partial \Phi}{\partial z},$$

$$\frac{\partial \rho E}{\partial t} + \frac{\partial \rho u h}{\partial x} + \frac{\partial \rho v h}{\partial y} + \frac{\partial \rho w h}{\partial z}$$

$$= -\rho u \frac{\partial \Phi}{\partial x} - \rho v \frac{\partial \Phi}{\partial y} - \rho w \frac{\partial \Phi}{\partial z}.$$

Here, ρ is the density, $\mathbf{u} = (u, v, w)$ is the velocity vector, P is the pressure, $E = \varepsilon + \mathbf{u}^2/2$ is the total specific energy, $h = \varepsilon + P/\rho + \mathbf{u}^2/2$ is the total specific enthalpy, ε is the specific internal energy,

$$\Phi(\mathbf{r}) = -\frac{GM_1}{|\mathbf{r} - \mathbf{r}_1|} - \frac{GM_2}{|\mathbf{r} - \mathbf{r}_2|} - \frac{1}{2}\Omega^2(\mathbf{r} - \mathbf{r}_c)^2$$

is the Roche potential, $\Omega = 2\pi/P_{orb}$ is the orbital angular velocity of the binary system, $\mathbf{r}_1$ and $\mathbf{r}_2$ are the centers of the two components, and $\mathbf{r}_c$ is the center of gravity of the system. The gas-dynamical equations were written in a coordinate system rotating with the binary. The origin of the coordinate system coincides with the center of the donor star, the x axis is directed along the line connecting the centers of the stars from the outflowing component to the accretor, the z axis is directed along the rotation axis, and the y axis is chosen to make a right-handed coordinate system. To complete the system of gas-dynamical equations, we add the ideal gas equation of state $P = (\gamma - 1)\rho\varepsilon$. In order to take radiative losses into account, we assumed the adiabatic index to be $\gamma = 1.01$, which corresponds to the nearly isothermal case. This, in turn, makes it possible to consider our model with $\gamma \sim 1$ as a energy-losing system [12, 13].

To solve the system of equations, we used a high-order Roe–Osher TVD scheme [14, 15] with the modification of Einfeldt [16]. We wrote the initial system of equations in dimensionless form; the distance between the components A and the inverse angular velocity of rotation of the system Ω^{-1} were used to normalize spatial and temporal quantities, while the density was made dimensionless by dividing it by its value at the inner Lagrange point L_1 (since the system of equations scales in both density and pressure, the density scale was chosen purely for convenience).

As noted above, we decreased the numerical viscosity by changing the step of the computational grid. Unfortunately, the limited capacity of the computer used prevented us from modeling the flow in a larger region (substantially exceeding the distance between the components [1–6]) on the fine grid. For this reason, following [17–20], we modeled the gas flow in a limited parallelepiped $[0.5A..1.5A] \times [-0.5A..0.5A] \times [0..0.25A]$ (the computations were carried out only in the upper half-space, since the problem is symmetrical relative to the equatorial plane). A sphere of radius 0.01 representing the accretor was cut out of the computation region. Figure 1 presents the parameters for the computation region in the equatorial plane (solid); the Roche equipotentials (dashed) and computation region used in [1–6] (dash–dot) are also shown.

As the initial condition, we adopted a rarefied gas with $\rho_0 = 10^{-5}$, $P_0 = 10^{-4}/\gamma$, and $\mathbf{u}_0 = 0$. The boundary conditions were determined as follows. The conditions for matter injection into the system were specified at a fictitious node corresponding to the inner Lagrange point: $\rho(L_1) = 1$, $P(L_1) = 10^{-2}/\gamma$, $u(L_1) = 10^{-2}$, $v(L_1) = w(L_1) = 0$. The sound velocity in this cell was equal to
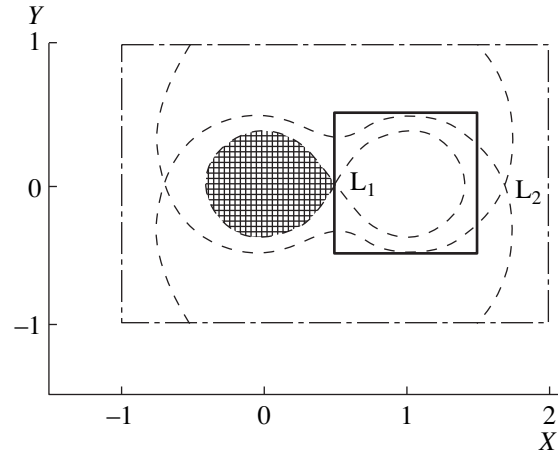

Fig. 1. Computation regions for the "full" (dash–dot) and "limited" (solid) cases. The shaded area denotes the donor star. The dashed curves show the Roche equipotentials.

$(L_1) = 10^{-1}$. At fictitious nodes inside the accretor, as well as on the rest of the outer boundary, the initial (background) values for parameters were maintained throughout the computation. Finally, we specified the boundary conditions using the solution of the decay problem (Riemann's problem) for the discontinuity between the gas parameters at the fictitious node and at the nearest computation node.

3. RESULTS

In [1–6], we investigated the flow morphology in a full computation region that was several times larger than the characteristic size of the system A and contained both components (Fig. 1). These studies revealed the important role of the intercomponent envelope in the formation of the flow structure. If a limited computation region is used in the simulations, this makes it impossible to adequately take into account the intercomponent envelope, and the "limited" solution can differ appreciably from the "full" one. In order to consider the influence of the restricted size of the computation region on the solution, we will compare the flow structures for the full model [6] with the results obtained for the same grid in the limited region.

Figures 2 and 3 present density contours and velocity vectors in the equatorial plane of the system for the full and limited computations, respectively. These figures also present the limiting (outer) stream lines along which the matter reaches the disk directly. Comparison of the results presented shows that, in the limited treatment, the flow morphology in the circum-disk area reflects the same basic flow features seen for the full treatment. In particular, an accretion disk is formed with approximately the same linear size; the shock waves I and II also arise due to the interaction of the intercomponent envelope gas with the stream flowing out from L_1 (note that the locations of the shock waves
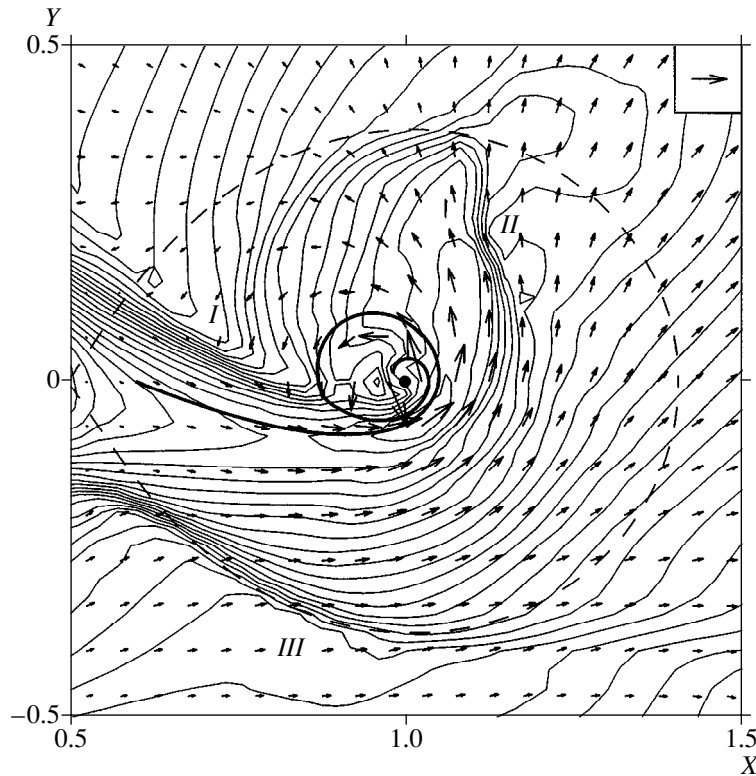
Fig. 2. Density contours and velocity vectors in the equatorial plane for the computation in the "full" area from [6]. The filled circle shows the accretor, and the dashed curves the Roche equipotentials. The vector in the upper right corner corresponds to a dimensionless velocity of $u = 3$. The thick line displays the limiting ("last") stream lines along which the flowing matter directly reaches the disk.

are indicated by the steepness of the density contours and the presence of a stream passing through the surface). At the same time, in the limited treatment, the role of the intercomponent envelope is not taken into account adequately. In particular, no streams can be seen along the Roche lobe of the donor star, while in [2], such streams disrupt the atmosphere of the outflowing star and substantially increase the mass transfer rate in the system. This appreciably changes the parameters of the stream in the limited treatment. This is illustrated in Fig. 4, which plots the density distribution in the equatorial plane of the system along the line containing L_1 and parallel to the Y-axis.

We can see from Fig. 4 that, in the limited treatment, the stream flowing from L_1 expands to a characteristic size $\epsilon = c(L_1)/A\Omega$ [21], and the density in the stream cross section decreases exponentially [21], while, in the full treatment, the density of matter in the stream is determined to a large extent by the disruption of the donor-star atmosphere. In addition, in the limited treatment, there is no stream of intercomponent gas returning under the action of the Coriolis force (from the side of the stream opposite to the direction of orbital motion). As a result, shock wave *III* in the full formulation disappears in the limited case. Summarizing our comparison between the full (the main features of the flow in this case are presented in the schematic diagram in Fig. 5) and limited treatments, we conclude:

(1) In the limited treatment, the effect of the common envelope on the solution is not taken into account entirely correctly. This results in both qualitative (there are no intercomponent gas streams in the system, as can be seen from stream lines *a* and *b* in Fig. 5; consequently, shock wave *III* disappears) and quantitative (the parameters of the stream vary since the atmosphere of the donor star was not taken into account; in particular, the stream width decreases substantially) changes in the solution.

(2) The flow morphologies in the vicinity of the accretor are qualitatively similar in the limited and full treatments. The fact that the intercomponent envelope was partially taken into account in the limited treatment (i.e., the matter that makes a turn around the accretor and interacts with the stream, shown by stream line *c* in Fig. 5) makes it possible to obtain a solution that coincides with the full one near the accretor. In particular, as can also be seen in the full treatment [1–6], in the limited solution, after the stream is deflected by the intercomponent envelope, it approaches the disk edge tangentially and does not lead to a shock interaction (hot spot) at the edge. The region of release of excess energy is located along the edge of the stream facing
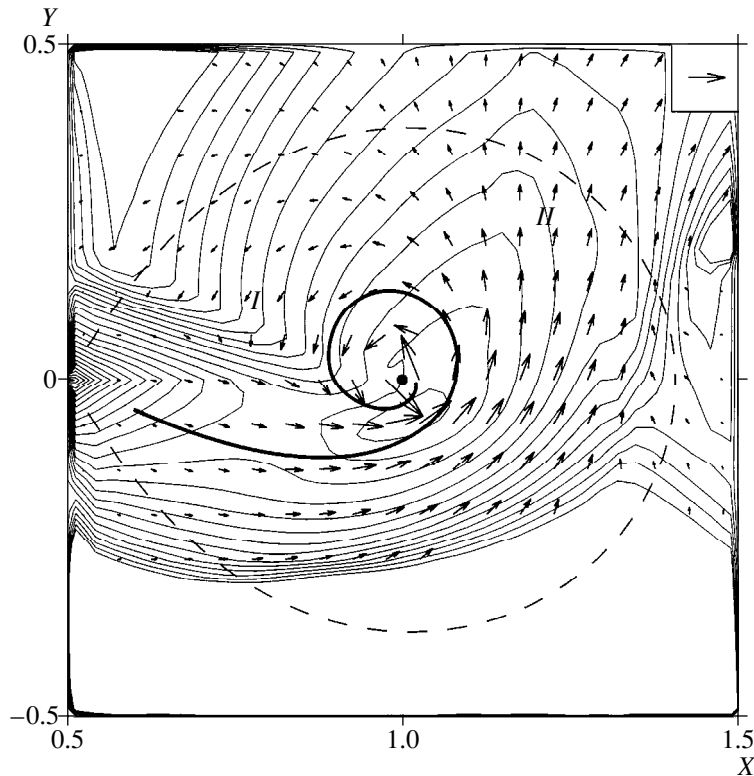
Fig. 3. Same as Fig. 2 for computation in the "limited" region on the same grid as the computation presented in Fig. 2.

the orbital motion, where the interaction of the common envelope and the stream forms the extended shock wave *I* (Figs. 2–5).

Our comparison between the limited and full treatments indicate that, with some reservations, consideration of the interaction between the stream and accretion disk is also possible in the limited formulation. This makes it possible to carry out computations on more detailed grids, i.e., for lower viscosities. It also enables us to study the effect of viscosity on the flow structure in the vicinity of the accretor, as well as the question of whether there exists a hot spot in the low viscosity case.

We have performed three sets of computations with different spatial resolutions for the grids: $31 \times 31 \times 17$, $61 \times 61 \times 17$, and $91 \times 91 \times 25$ (thereafter computations A, B, and C). In all cases, the grid was uniform. In terms of an α disk, the numerical viscosities in cases A, B, and C roughly corresponded to $\alpha \sim 0.08$–0.1, 0.04–0.06, and 0.01–0.02.

Comparisons of the results of computations A, B, and C with each other and with the results obtained in [20] (where a $200 \times 200 \times 50$ grid was used in the same formulation) can be used to study the effect of viscosity on the solutions. Figures 6–8 present the density fields and velocity vectors in the equatorial plane of the system for cases A, B, and C, together with stream line *a*, which delimits the accretion disk. Numerical analysis

of the solutions obtained indicates that the interaction between the stream and disk is shockless in all cases. The stream and accretion disk display the same morphology and, consequently, no hot spot is formed in the system. This is illustrated in Fig. 9, which shows for case C (with minimum viscosity) the distribution of the
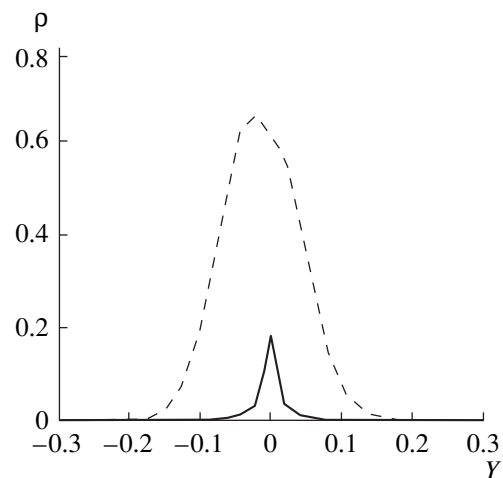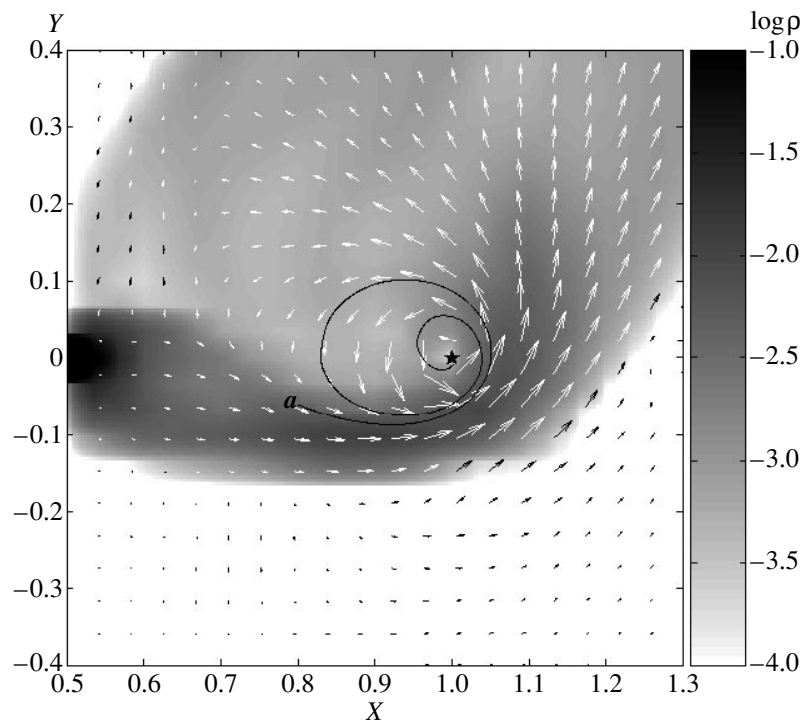

Fig. 4. Density distribution in the equatorial plane along the line containing L_1 ($x = 0.5$, $y = 0$, $z = 0$) and parallel to y axis for the "full" (dashed) and "limited" (solid) cases.
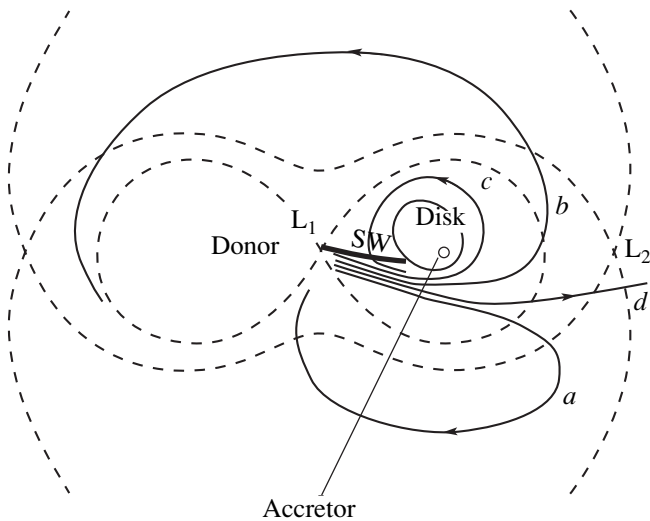
Fig. 5. Schematic representation of the main features of the gas-dynamical flow pattern in semidetached close binary systems. The Roche lobe (dashed curves), location of the accretor and Lagrange points, and quasi-elliptical accretion disk are shown. The shock wave resulting from the interaction of the common-envelope gas with the stream is marked SW and is plotted by a thick line. The stream lines *a*, *b*, *c*, and *d* display the main directions of gaseous flows in the system. Streams denoted *a*, *b*, and *c* form the common envelope of the system. The stream leaving the system is denoted *d*.

dimensionless temperature in the *xy* plane for four values of *Z*: $z = 0$ (equatorial plane) and $z = h$, $2h$, and $3h$, where *h* (the height of a computation cell) corresponds to $0.01A$. The dimensionless temperature at the point L_1 is 10^{-2}. In order to obtain the physical temperature, we must multiply the dimensionless values by GM/AR, where *G* is the gravitational constant, *M* the total mass of the system, *A* the distance between the components, and *R* the gas constant. The temperature fields in Fig. 9 provide evidence for the absence of a region of energy release at the place where the stream and the disk come into contact, i.e., for the absence of a hot spot for all *z* values. Examination of the variation of the gas parameters along the stream lines confirms this conclusion. In particular, Fig. 10 presents the variation of the dimensionless temperature along stream line *b* (Fig. 8), which shows that there is no hot spot at the stream–disk contact point (section "*1–2*") and that there is a region of energy release in the place where shock wave *I* forms (section "*3–4*" in Figs. 8 and 10).

Comparison of the solutions obtained indicates (see, for example, Figs. 6–8) that the increase of spatial resolution of the grid and associated decrease of numerical viscosity decrease diffusion blurring of the stream flowing out from the inner Lagrange point. In the computations with a thinner stream (versions B and C and the computation from [20]), the role of the intercomponent envelope gas flowing around the stream from
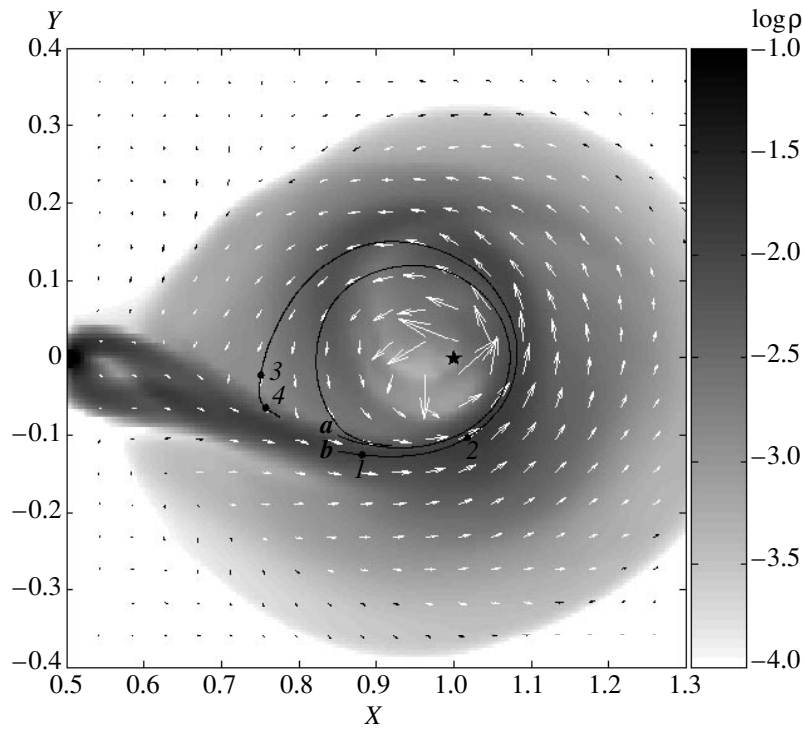

Fig. 6. Density distribution in the equatorial plane for computation A ($31 \times 31 \times 17$ grid). The arrows display the velocity vectors. The asterisk marks the position of the accretor. The stream line *a*, which delimits the accretion disk, is also shown.
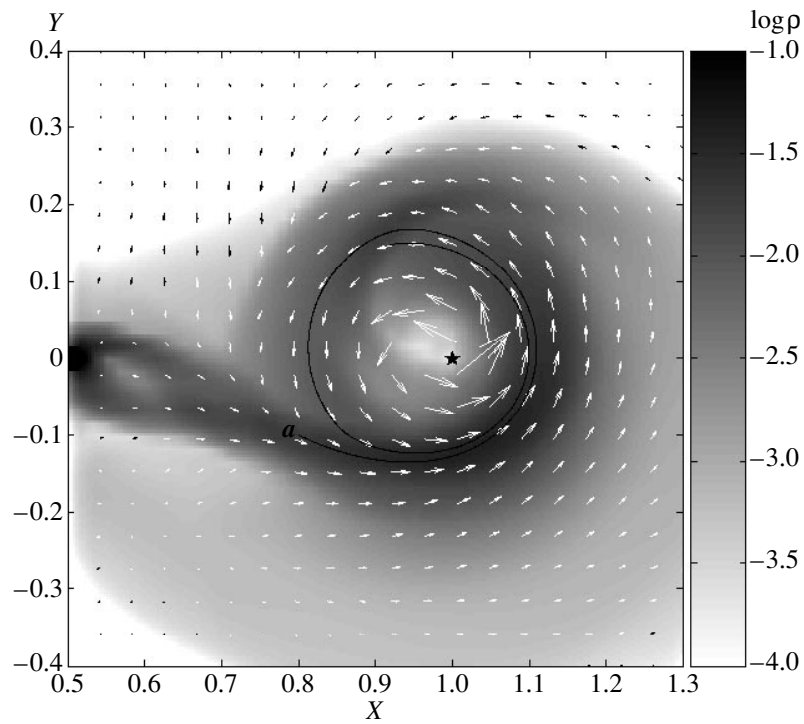
Fig. 7. Same as Fig. 6 for computation B ($61 \times 61 \times 17$ grid).

Fig. 8. Same as Fig. 6 for computation C ($91 \times 91 \times 25$ grid). In addition to stream line *a*, which delimits the accretion disk, the stream line *b* passing through the shock wave is shown. Section "*1–2*" in stream line *b* corresponds to the point of contact of the stream flowing out from L_1 with the accretion disk, and section "*3–4*" corresponds to the zone of interaction of the intercomponent gas with the stream (shock wave *I*).
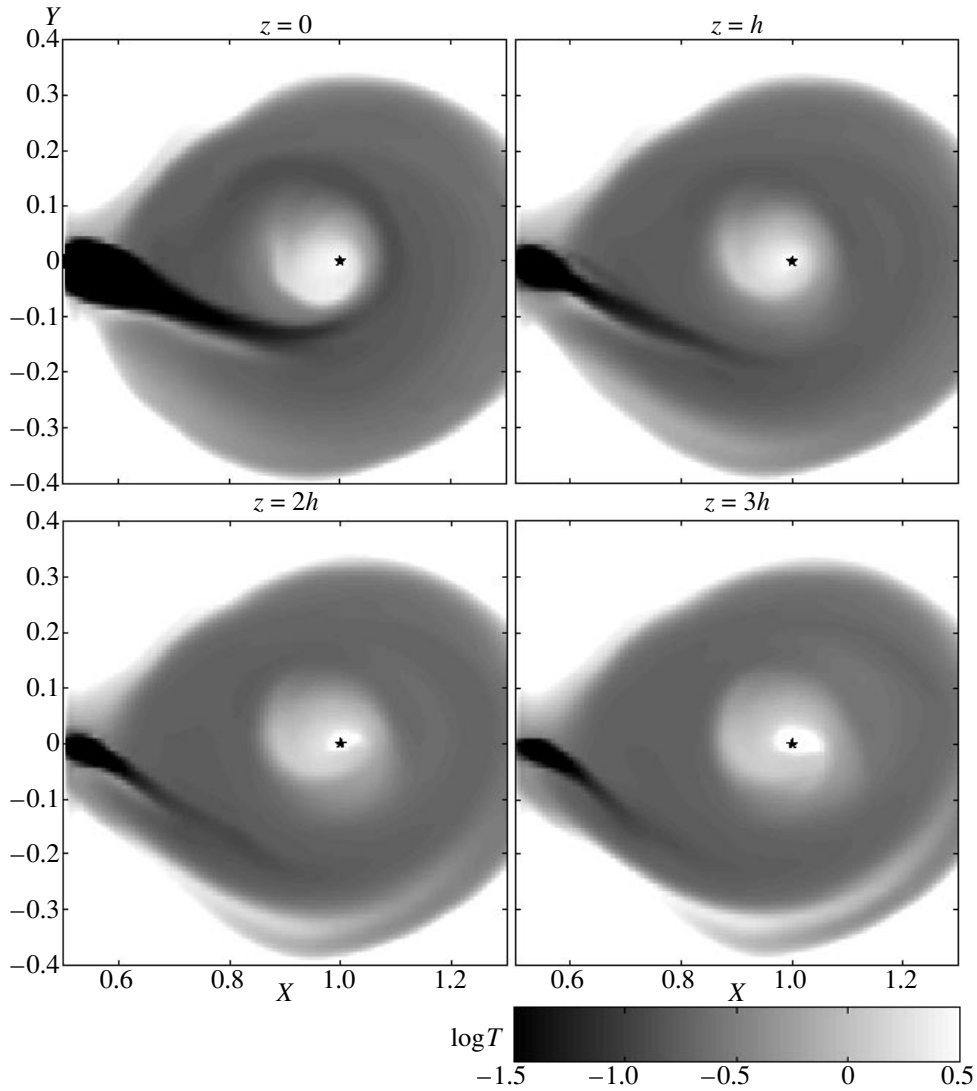
Fig. 9. Dimensionless temperature distribution for computation C ($91 \times 91 \times 25$ grid) in the equatorial plane ($z = 0$), and also in the parallel planes $z = h$, $2h$, and $3h$, where $h \approx 0.01$ is the height of a computation cell. The asterisk marks the position of the accretor.
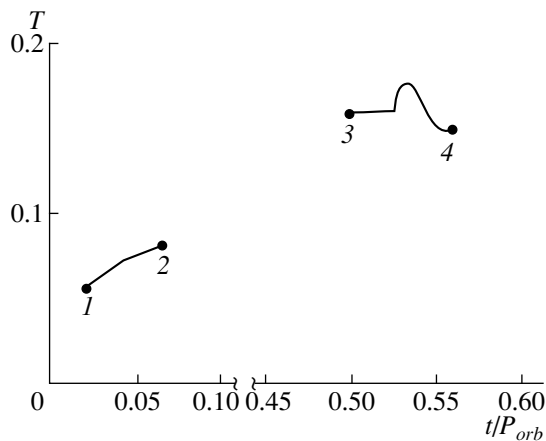
Fig. 10. Variations of dimensionless temperature along stream line *b* shown in Fig. 8. Section "*1–2*" corresponds to the place of contact of the stream and the accretion disk, and section "*3–4*" to the shock wave *I*.

above and below becomes substantial. This is illustrated by Fig. 11, which shows the density field and velocity vectors in the *YZ* cross section containing the point (0.9, 0.0, 0.0) for case C. The variation of the density (increase of the flow width) in the region where the envelope gas flows around the stream can also be seen in Fig. 12, which displays the density field in the frontal (*XZ*) plane (also for version C). The presence of the gas flowing around the stream can give the impression of a shock interaction between the stream and disk (see, for example, the 3D images of the surfaces of constant density in Fig. 13 and in [20]), even though the solution unambiguously suggests that the character of the flow is smooth.

In our studies [1–6], we outlined the structure of the flow pattern as follows:
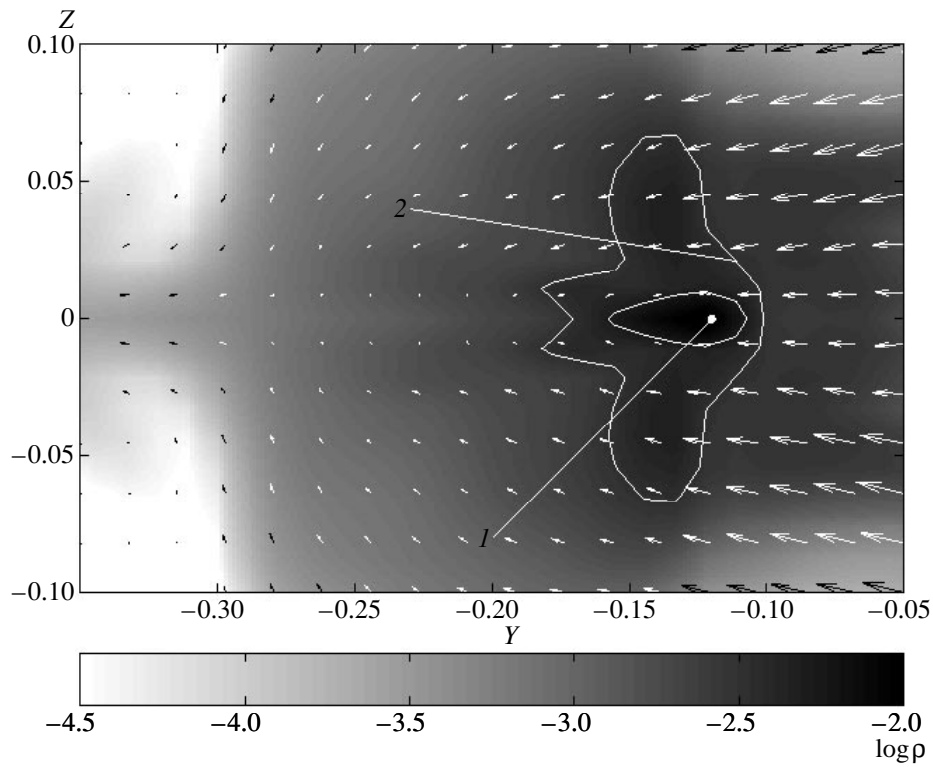
Fig. 11. Density and velocity-vector distribution in the *YZ* plane containing the point (0.9, 0.0, 0.0), for computation C (91 × 91 × 25 grid). "*1*" marks the position of the central portion of the stream, limited by the $\log\rho = -2.3$ contour; the "2" on the $\log\rho = -2.5$ contour marks shock wavefront *I*.
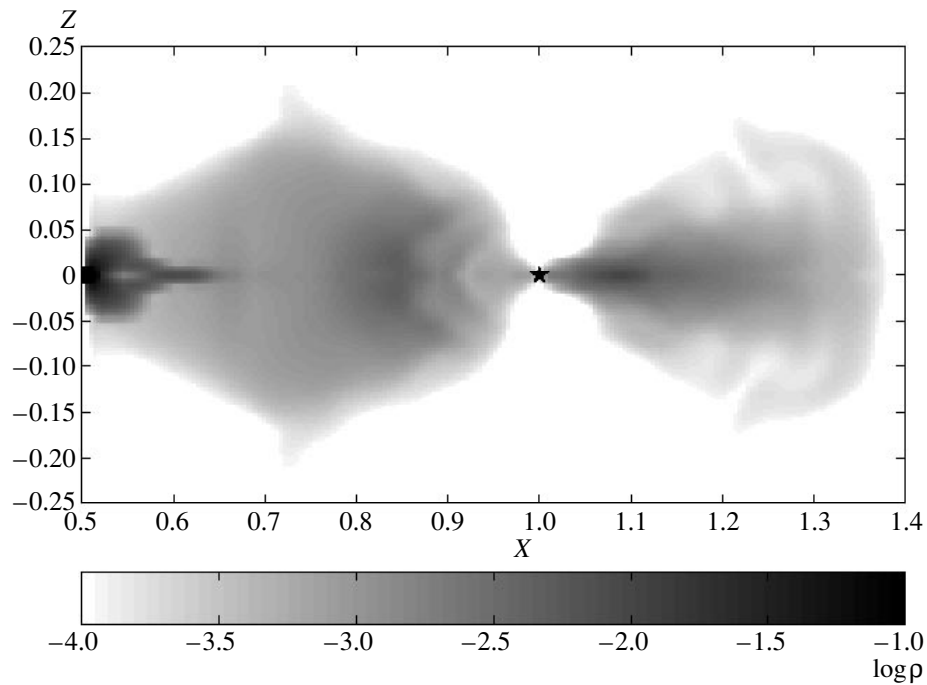
Fig. 12. Density and velocity-vector distribution in the frontal *XZ* plane for computation C (91 × 91 × 25 grid). The asterisk marks the position of the accretor.
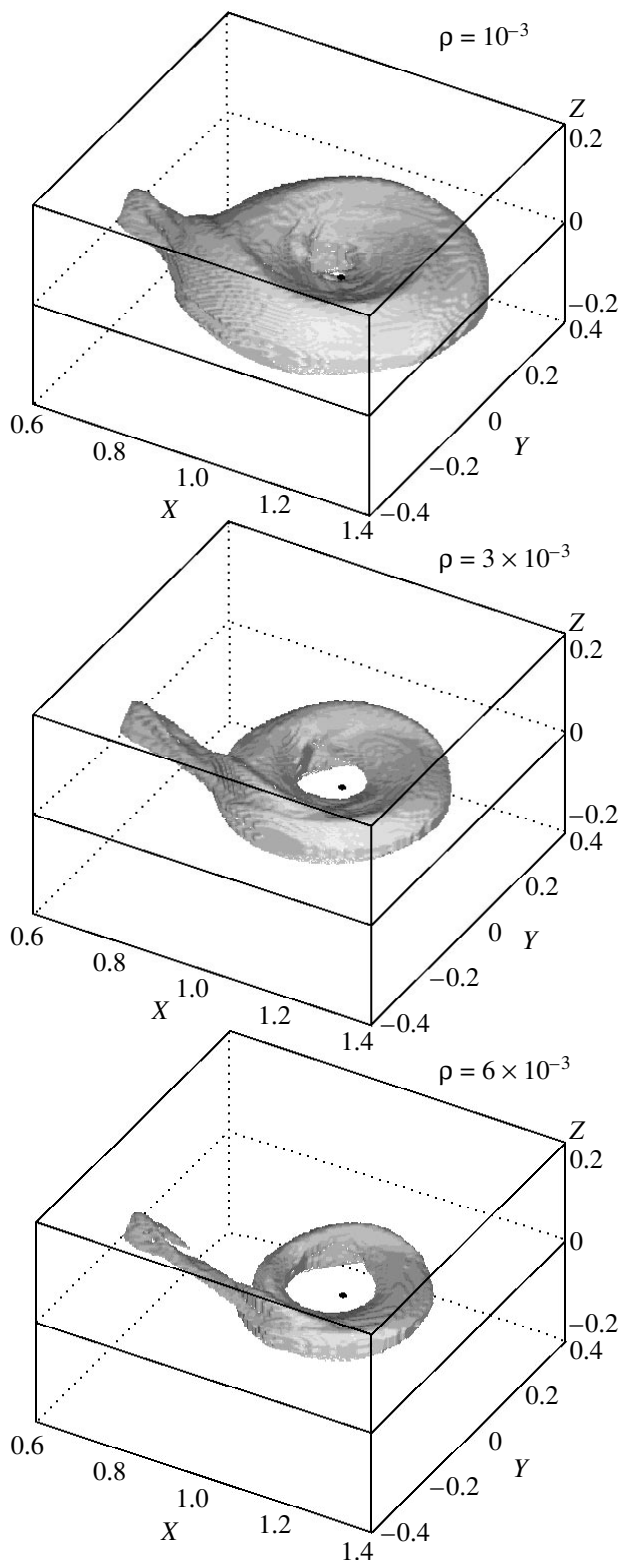
Fig. 13. 3D representation of the surface of constant density at the $\rho = 10^{-3}$ (top), 3×10^{-3} (center), and 6×10^{-3} (bottom) levels. The position of the accretor is marked by the filled circle.

(1) The disk, i.e. the stream material that is immediately captured by the gravitation of the accretor and is subsequently accreted;

(2) The intercomponent envelope, i.e., all remaining material; some fraction of this material makes a rotation around the accretor, interacts with the stream, and can then be accreted.

Therefore, we separated the stream material according to the physical situation: If gas leaves the system or later interacts with the initial stream, this material does not belong to the disk. In the solutions with low viscosity, another part of the envelope appears—material that flows around the stream from above and below. We can see from the stream lines that this part of the envelope does not belong to the disk. A larger fraction of this material leaves the system or, while moving around the accretor, gradually approaches the equatorial plane and then collides with the stream. In addition to the terms in [1–6], it seems appropriate to introduce the new term "circum-disk halo" to describe material that (a) makes a rotation around the accretor (i.e., is gravitationally bound), (b) does not belong to the disk (in a physical formulation), (c) interacts with the stream (collides or flows around), and (d) later (after the interaction) either joins the material being accreted or leaves the system.

Variation of the viscosity in the system must inevitably affect the accretion rate. Computation versions A, B, and C indicate that, as expected, the accretion rate decreases in computations with lower viscosity. Unfortunately, a detailed study of this problem requires enormous amounts of computation time, which substantially exceed our resources. The point is that, in the large-viscosity computations in [1–6], the viscosity time of the disk

$$\tau_{\text{disk}}^{\text{visc}} = R_{\text{disk}}^2/\nu = R_{\text{disk}}^2/\alpha c_s H,$$

where c_s is the sound speed and H is the characteristic width of the disk, did not substantially exceed the gas-dynamical timescale for the disk

$$\tau_{\text{disk}}^{\text{hd}} = R_{\text{disk}}/c_s,$$

which made it possible to achieve a steady-state solution within several orbital periods of the system. When the viscosity decreases, it becomes difficult to reach a steady-state solution, since our limited computer power prevents us from performing computations over times exceeding $\tau_{\text{disk}}^{\text{visc}}$. Version C, which investigates the time dependence of the masses of the disk and halo, indicates that, even for times exceeding 15 orbital periods, the solution was still not steady-state. This made it impossible to obtain reliable numerical estimates for the accretion rates in systems with low viscosities.

4. CONCLUSION

Our results for 3D simulations of the gas dynamics of the mass exchange in semidetached binary systems provide evidence for the absence of a hot spot in a self-

consistent solution of the problem. We first drew this conclusion for systems with high viscosities [1–6]. The computation results presented here have confirmed the absence of a shock interaction of the stream (flowing from L$_1$) with the forming accretion disk for solutions with various viscosities.

The obtained solutions indicate that, in systems with different viscosities, after the stream is deflected by the action of the intercomponent-envelope gas, it approaches the disk tangentially and does not give rise to a shock disturbance (hot spot) at the edge of the disk. The region of release of excess energy is located at a shock wave along the edge of the stream facing the orbital motion. This indicates that the flow patterns are qualitatively similar for different disk viscosities. At the same time, in the computations with low viscosities (where the diffusion is also low and, consequently, the stream width is small), the intercomponent-envelope gas flowing around the stream from above and below substantially influences the flow pattern. To describe this feature of the pattern, we have introduced an additional term, "the circum-disk halo."

ACKNOWLEDGMENTS

REFERENCES

1. D. V. Bisikalo, A. A. Boyarchuk, O. A. Kuznetsov, *et al.*, Astron. Zh. **74**, 880 (1997).
2. D. V. Bisikalo, A. A. Boyarchuk, O. A. Kuznetsov, *et al.*, Astron. Zh. **74**, 889 (1997).
3. D. V. Bisikalo, A. A. Boyarchuk, O. A. Kuznetsov, *et al.*, Astron. Zh. **75**, 40 (1998).
4. D. V. Bisikalo, A. A. Boyarchuk, O. A. Kuznetsov, *et al.*, Astron. Zh. **75**, 706 (1998).
5. D. V. Bisikalo, A. A. Boyarchuk, V. M. Chechetkin, *et al.*, Mon. Not. R. Astron. Soc. **300**, 39 (1998).
6. D. V. Bisikalo, A. A. Boyarchuk, V. M. Chechetkin, *et al.*, Astron. Zh. **76**, 905 (1999).
7. F. Meyer and E. Meyer-Hofmeister, Astron. Astrophys. **104**, L10 (1981).
8. J. K. Cannizzo, W. Chen, and M. Livio, Astrophys. J. **454**, 880 (1995).
9. F. Honma, R. Matsumoto, and S. Kato, Astrophys. J., Suppl. Ser. **210**, 365 (1993).
10. E. Szuszkievich and J. C. Miller, Mon. Not. R. Astron. Soc. **287**, 165 (1997).
11. J. K. Cannizzo, Astrophys. J. **419**, 318 (1993).
12. K. Sawada, T. Matsuda, and I. Hachisu, Mon. Not. R. Astron. Soc. **219**, 75 (1986).
13. D. V. Bisikalo, A. A. Boyarchuk, O. A. Kuznetsov, *et al.*, Astron. Zh. **72**, 367 (1995).
14. P. L. Roe, Ann. Rev. Fluid Mech. **18**, 337 (1986).
15. S. Osher and S. Chakravarthy, SIAM J. Numer. Anal. **21**, 955 (1984).
16. B. Einfeldt, SIAM J. Numer. Anal. **25**, 294 (1988).
17. D. Molteni, G. Belvedere, and G. Lanzafame, Mon. Not. R. Astron. Soc. **249**, 748 (1991).
18. G. Lanzafame, G. Belvedere, and D. Molteni, Mon. Not. R. Astron. Soc. **258**, 152 (1992).
19. P. J. Armitage and M. Livio, Astrophys. J. **470**, 1024 (1996).
20. M. Makita, K. Miyawaki, and T. Matsuda, Preprint astro-ph/9809003.
21. S. H. Lubow and F. H. Shu, Astrophys. J. **198**, 383 (1975).

Translated by K. Maslennikov

The Accretion Activity of the Ae Herbig Star CQ Tau

O. V. Kozlova[1], V. P. Grinin[1, 2], and A. N. Rostopchina[1]

[1]*Astrophysical Observatory, Nauchnyĭ, Crimea, Ukraine*
[2]*Astronomical Institute, St. Petersburg University, St. Petersburg, Russia*
Received January 27, 1999

Abstract—Results of spectral observations of the isolated Ae Herbig star CQ Tau obtained in 1995–1998 in the H_α line and near the sodium resonance doublet are presented, together with simultaneous photometric monitoring of the star. CQ Tau is a member of the family of young UX Ori stars with nonperiodic Algol-like brightness decreases. The star is surrounded by an accretion disk, in which its emission-line spectrum and part of its absorption-line spectrum are formed. The strong variability of the H_α, D NaI, and HeI 5876 Å lines testifies that the gaseous disk is appreciably inhomogeneous in both the radial and azimuthal directions. This inhomogeneity probably results from uneven feeding by the circumstellar material from the peripheral regions of the circumstellar disk. Over the four years of observations, we observed the star in deep minima three times ($\Delta V \sim 2$). On these nights, an increase in the H_α equivalent width followed the decrease in radiation flux. In the two deepest minima, the normally two-component line profile had only a single component with a nearly symmetrical profile. This behavior of the H_α line is in good agreement with the results of numerical modeling of Algol-like minima and can be used to estimate the parameters of the dust clouds eclipsing the star and inner accretion disk. These estimates suggest that the circumstellar dust clouds can approach very close to the star and be sublimated there. © *2000 MAIK "Nauka/Interperiodica"*.

1. INTRODUCTION

Ux Ori stars, whose ages usually do not exceed several million years, are one of the youngest star actively being studied. They are surrounded by nonuniform disk-like envelopes of gas and dust. Some of the circumstellar dust is concentrated in dust clouds. When these pass through the line of sight from time to time, they strongly decrease the observed brightness of the star by amounts reaching $2–3^m$. This mechanism, proposed at the end of the 1960s by Wenzel [1] and modified by Grinin [2], is currently considered to be the origin of the violent photopolarimetric activity of stars of this type (see the reviews [3–6] and reference therein). To an appreciable extent, this is due to the orientation of their circumstellar disks relative to the observer—edge-on or at a small inclination to the line of sight. Such an orientation is indicated by first, the high degree of linear polarization of UX Ori stars during deep brightness minima [3, 4]; second, the frequent occurrence of double H_α line profiles in their spectra [4, 7]; and third, the absence of a correlation between the amplitude of their optical variability and the masses of their circumstellar disks as determined from millimeter observations [8]. Due to the nearly edge-on orientation of their circumstellar disks, the radiation of UX Ori stars passes through the disk as it travels toward the observer and is partially absorbed in it. For this reason, investigations of the spectral activity of these stars and its connection with their photometric activity is of considerable interest for our understanding of the physical processes occurring in the regions near young stars.

We present here the results of simultaneous spectral and photometric observations of the isolated Ae Herbig star CQ Tau, which is one of the most active [9] UX Ori stars and is among the best studied spectroscopically. Table 1 presents the main parameters of the star from [10]. It is clear that CQ Tau occupies an intermediate position between Ae/Be Herbig stars and T Tauri stars. Studies of such transition objects present special interest, since they can be used to search for general behaviors and can reveal possible differences in the physical processes occurring near young stars with different masses.
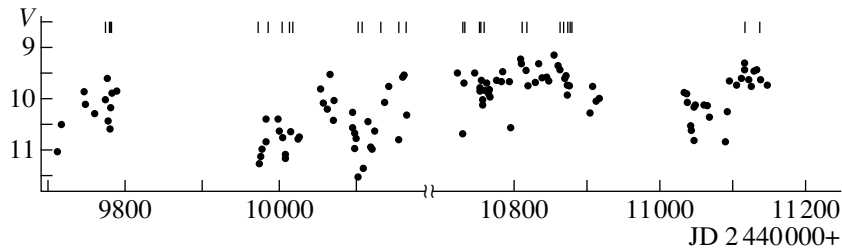
2. OBSERVATIONS

We obtained spectral observations of CQ Tau during the 1994–1998 observational seasons. The spectra were obtained on the 2.6-m telescope of the Crimean Astro-

Table 1. Main parameters of CQ Tau

Parameter	CQ Tau
r, pc*	99*
Sp	A8, F2IV
M_*, $M_\odot$	1.5
R_*, $R_\odot$	1.9
L_*, $L_\odot$	6.6
t, years	10^7

* From [11].

Fig. 1. Light curve of CQ Tau in the *V* band. The dates of the spectral observations are indicated above.

physical Observatory with a Coudé spectrograph and CCD camera. All the spectra near the *D* NaI lines and most of the H_α spectra had resolutions $R = 15\,000$ and $R = 20\,000$, respectively. Detailed information about the dates, exposures, and spectral resolutions of the observations is presented in Table 2.

Simultaneous with the spectral observations, we obtained photometric observations of CQ Tau on the 1.25-m CAO telescope, which was equipped with a photopolarimeter constructed according to the design of Piirola [12]. We used the usual observing method, including exposures of the background sky and standard stars. Table 2 presents the photometric data reduced to the Johnson *UBVRI* system and for the *V* band. These data testify to the high level of photometric activity of the star: Its brightness varies from $V = 9.31\text{--}11.51^m$. As we can see in Fig. 1, during our four years of observations, we were able to obtain spectra of CQ Tau covering essentially the entire interval of brightness variations for the star.

We cleaned the CCD spectra of cosmic rays, then corrected for the flat field. The reduction of the spectra (subtraction of the sky background, normalization, and so forth) were carried out using the SPE program developed by S.G. Sergeev. The spectra near the sodium resonance doublet were also cleaned of the numerous atmospheric water lines in this part of the spectrum. We did this using observations of the spectra of hot comparison stars for similar air masses. All the reduced spectra were corrected for the motion of the Earth around the Sun.

3. RESULTS

3.1. H_α Line

The CQ Tau H_α spectra are presented in Fig. 2. We can see that, in the vast majority of cases, the line has the asymmetric two-component profile that is typical for rotating circumstellar gas, with a ratio of the intensities of the blue (*V*) and red (*R*) components $V/R > 1$ that is characteristic of accretion. The opposite type of profile, indicating the motion of gas from the star toward the observer, is never observed in the spectra of CQ Tau.

We can see from Fig. 2 that the radial velocity of the blue emission wing changes only slightly and is usu-

ally less than 300 km/s. On the contrary, the red wing is strongly variable, and its maximum radial velocity reaches 400 km/s. The simplest explanation for this asymmetry is that some of the moving circumstellar gas is not observed because it is blocked by the star, and this is probably the situation we are dealing with in CQ Tau. In the case of accretion, the star screens from the observer gas falling onto it and reaching its maximum velocity near the stellar surface. It is precisely this part of the envelope (emitting in the blue wing of the H_α line) that the observer does not see.

Comparison with other H_α spectra of CQ Tau obtained in bright states [9, 13] shows that the parameters of the line profile and equivalent width were in the range observed by us for similar brightness states. In 1997–1998, the central absorption is slightly doubled in some spectra. On one night (December 28, 1997), an additional absorption component appeared in the red wing of the line, providing evidence that, at that time, the line of sight was intersected by an extended gaseous cloud moving toward the star with a velocity of ~150–300 km/s. As we can see in Fig. 2, the properties of the H_α line and, in particular, the *V/R* ratio change rather strongly with time. We observed the strongest variations during two deep minima (January 18, 1996, and January 24, 1996), during which the two-component line had one component, and its full width at half maximum appreciably decreased. The same transformation of a two-component to a one-component H_α profile has been observed twice in the spectrum of UX Ori itself during deep minima [14, 15]. Figure 2 also shows that, at times of minimum brightness, together with the variations of the H_α profile, there was an increase in its equivalent width EW; overall, the flux in the line decreased somewhat (see below).

3.2. The D NaI Sodium Resonance Doublet

The sodium resonance doublet observed in the spectrum of CQ Tau is a blend of three components: a rotationally broadened photospheric line ($V\sin i \approx 90$ km/s [16]), a narrow interstellar line, and a redshifted, variable circumstellar line. Their relative contributions are shown in Fig. 3, using the spectra of CQ Tau obtained on October 9, 1997, as an example. We calculated synthetic spectra using the SYNTH and ROTATE pro-

Table 2. Spectral observational data for CQ Tau

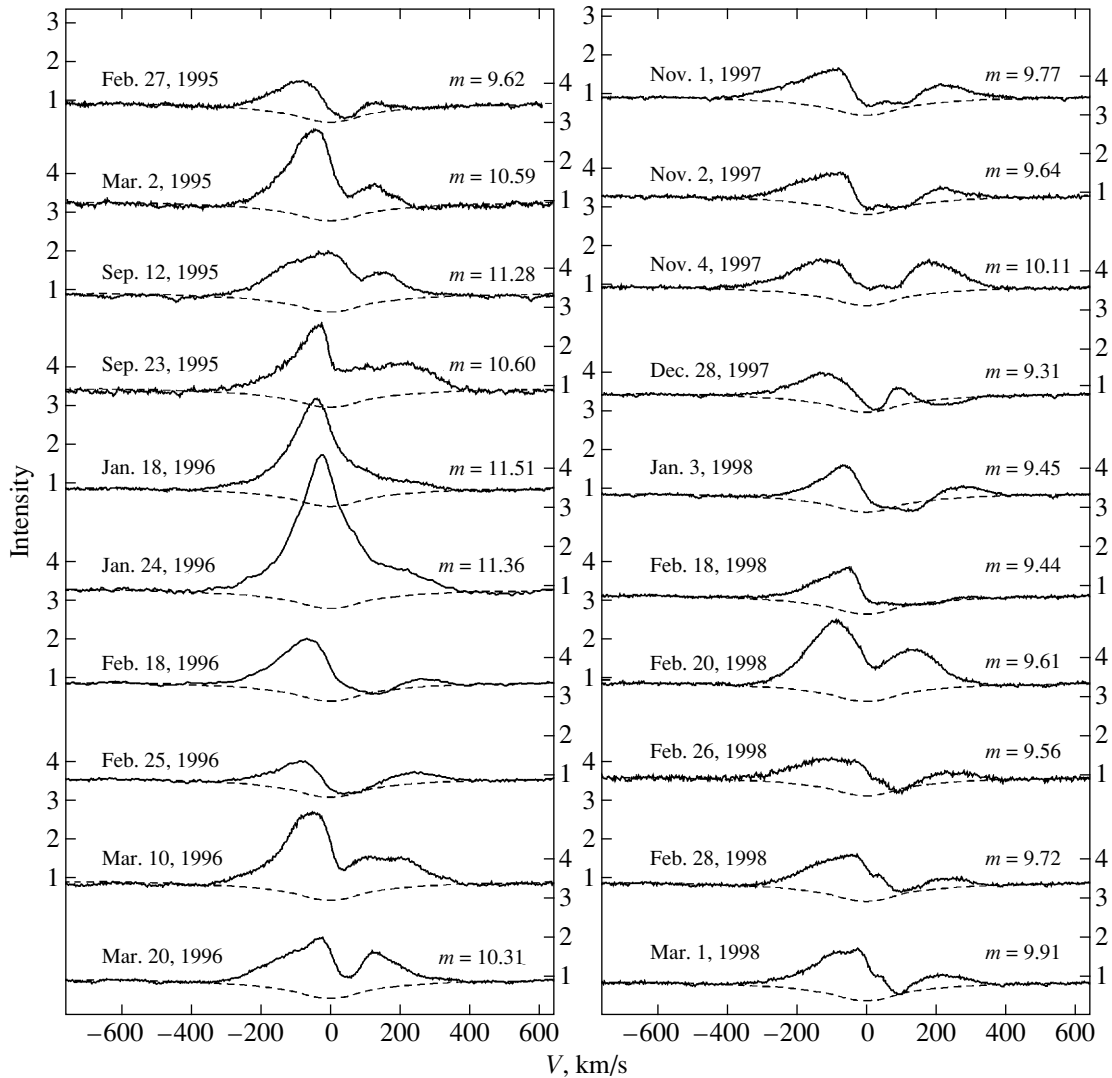| Data	V	Spectral interval	Exposure, min	Spectral resolution, Å	EW(H_α), Å	V_R (abs), km/s
30.01.1995	10^m40	H_α	30	0.64	5.5	76
27.02.1995	9.62	H_α	20	0.80	5.2	48
	–	D NaI	60	0.40		60
2.03.1995	10.59	H_α	5	0.64	9.9	59
	–	D NaI	60	0.32		52
3.03.1995	10.18	D NaI	70	0.32		54
4.03.1995	–	D NaI	57	0.32		57
5.03.1995	9.91	D NaI	60	0.32		51
12.09.1995	11.28	H_α	30	0.64	10.0	99
	–	D NaI	66	0.32		60
23.09.1995	10.40	H_α	14	1.00	13.9	47. 100
14.10.1995	11.10	D NaI	59	0.80		
23.10.1995	10.64	D NaI	120	0.40		52
26.10.1995	10.80	D NaI	117	0.40		45
18.01.1996	11.51	H_α	50	0.40	18.1	
	–	D NaI	60	0.40		51
24.01.1996	11.36	H_α	34	0.64	17.7	
18.02.1996	–	H_α	29	0.80	6.8	130
	–	D NaI	192	0.40		50
25.02.1996	–	H_α	65	0.80	4.6	58
	–	D NaI	170	0.40		
10.03.1996	9.57	H_α	20	0.64	13.4	43. 160
	–	D NaI	60	0.32		47
20.03.1996	10.31	H_α	17	0.32	9.3	57
	–	D NaI	120	0.32		
8.10.1997	10.68	D NaI	21	0.32		10
9.10.1997	9.69	D NaI	32	0.32		82
10.10.1997	–	D NaI	45	0.32		99
1.11.1997	9.77	H_α	20	0.32	6.7	13. 102
	–	D NaI	80	0.32		90
2.11.1997	9.64	H_α	20	0.32	5.0	14. 87
	–	D NaI	80	0.32		83
4.11.1997	10.11	H_α	20	0.40	8.6	16. 80
	–	D NaI	45	0.40		67
28.12.1997	9.31	H_α	15	0.32	4.2	32. 225
	–	D NaI	120	0.32		134
3.01.1998	9.45	H_α	25	0.32	4.2	51. 130
	–	D NaI	60	0.32		92
18.02.1998	9.44	H_α	18	0.32	4.2	34. 142
	–	D NaI	35	0.32		53
20.02.1998	–	H_α	40	0.32	12.6	30
26.02.1998	9.56	H_α	30	0.32	5.4	100
	–	D NaI	60	0.32		82
28.02.1998	9.72	H_α	35	0.32	6.2	103
	–	D NaI	57	0.32		82
1.03.1998	9.91	H_α	20	0.32	6.9	100
	–	D NaI	120	0.32		94

Fig. 2. H_α emission-line profile for the spectrum of CQ Tau.

grams of N.E. Piskunov [17] and the VALD database of atomic spectral-line parameters [18]. We took the model parameters from [19].

We can see from Fig. 4 that the circumstellar sodium line in the spectrum of CQ Tau is strongly variable with time. In the spectra of hotter UX Ori stars, such components are fairly weak, and their variability most likely reflects the sporadic falling of gas onto the star, rather than a more continuous process [6, 15, 20, 21]. In contrast, we observe in the spectrum of CQ Tau very intense absorption lines whose parameters resemble an inverse P Cyg profile blended with an interstellar absorption line, and differ from such a profile in the nearly complete absence of an emission component blueward of the absorption.

In some spectra, however, this component is clearly visible. These are the spectra obtained during the brightness minima of September 12, 1995, and January

18, 1996, and also on the night of February 18, 1996, when we were not able to obtain photometric observations due to poor weather conditions. In all three cases, the emission component in the sodium lines provides evidence for modest velocities of motion for the gas (~30–50 km/s).

We should note also two other interesting episodes observed on November 1, 1997, and October 8, 1997: In both cases, narrow circumstellar absorption components are clearly visible blueward of the interstellar lines. We can see from Table 2 that, on the first of these nights, the star was in a bright state ($V = 9.77$), while on the second, it was in a faint state ($V = 10.68$), only 0.6^m brighter than the deep minimum of September 12, 1995.

These observations suggest that the low-velocity sodium emission components observed in the two deep minima are not permanent features of these lines and are visible only at times of minimum brightness due to

Intensity

Oct. 9, 1997

5860 5870 5880 5890 5900 5910 5920

λ, Å
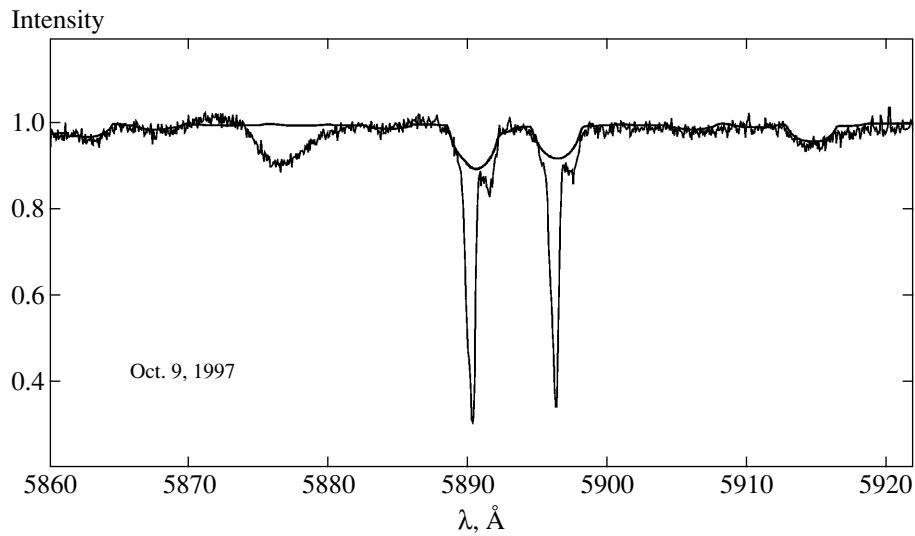
Fig. 3. Spectrum of CQ Tau near the sodium resonance doublet observed on October 9, 1997, and a synthesized spectrum for the star (see text).

Intensity

Feb. 27, 1995

Mar. 2, 1995

Mar. 3, 1995

Mar. 4, 1995

Mar. 5, 1995

Sep. 12, 1995

Oct. 14, 1995

Oct. 23, 1995

Oct. 26, 1995

Jan. 18, 1996

Feb. 18, 1996

Feb. 25, 1996

Mar. 20, 1996

Oct. 8, 1997

Oct. 9, 1997

5880 5890 5900

5870 5880 5890 5900

λ, Å
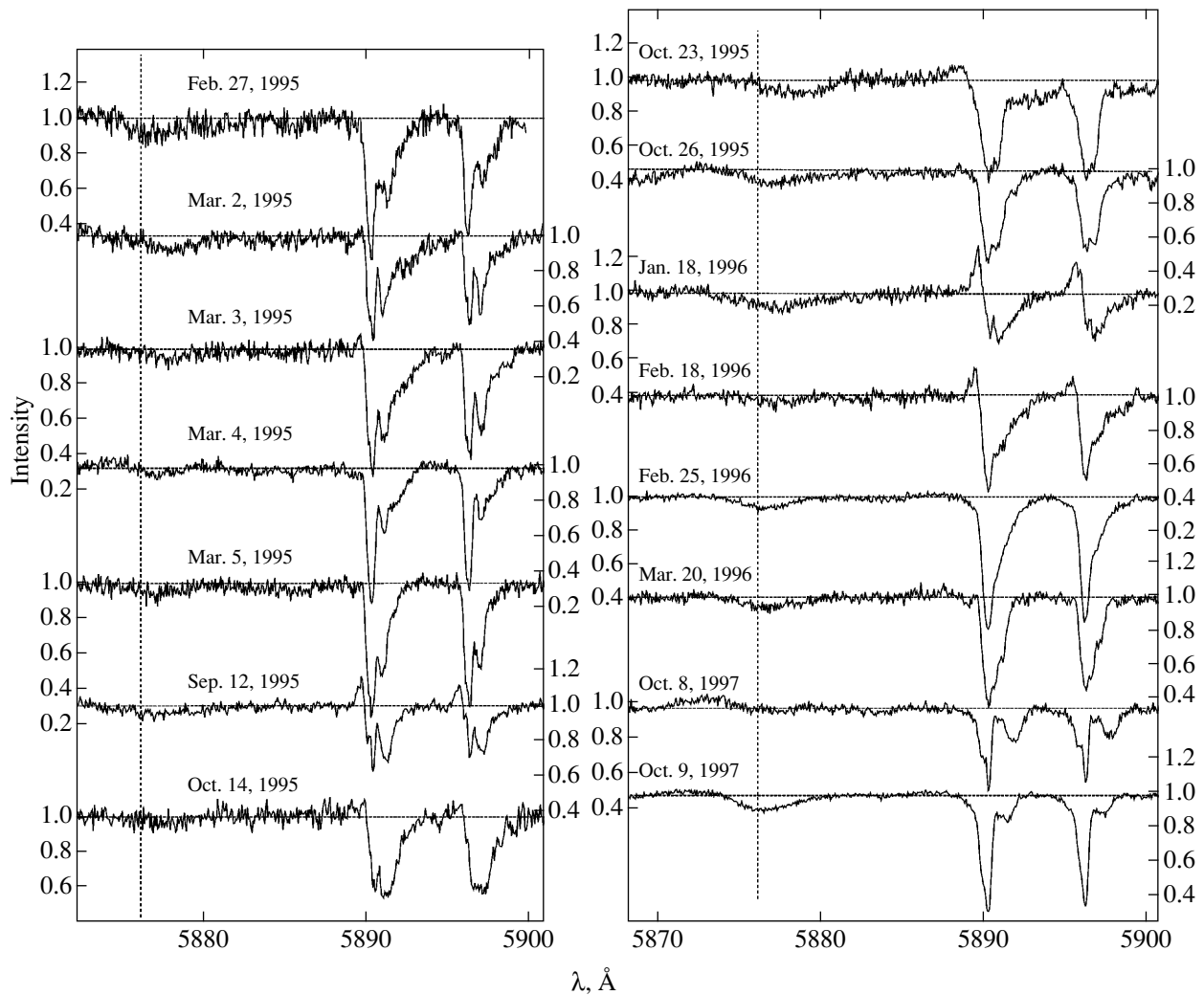
Fig. 4. Spectrum of CQ Tau near the *D* NaI sodium resonance doublet. To the left of the sodium line, the HeI 5876 Å line is visible. The vertical dashed line shows the wavelength of this line in the rest frame of the star (see text).

the decrease in the contrast of the continuous spectrum. (Otherwise we should also have observed them on October 8, 1997, when the star was already rather faint; however, instead, the narrow absorption components are visible in Fig. 4.) In addition, the appearances of these emission components at minimum brightness cannot be considered completely chance occurrences. The reason is that very similar sodium-line profiles with blue emission components have twice been observed in the spectrum of UX Ori during a deep brightness minimum in 1992 [15].

Taking this into account, we conclude that, at times when the star is eclipsed by a dust cloud, the probability increases that additional low-velocity emission or absorption features will appear in the sodium lines. This unequivocally indicates that these line components appear as a result of resonance scattering of the star's radiation in the eclipsing cloud itself, in which there is both dust and gas, including atomic neutral sodium.

We can see from Fig. 4 that the red wings of the circumstellar sodium absorption lines are time variable and, on some dates, extend up to velocities of 300 km/s

and more. We studied the dynamics of these variations in order to search for possible periodicities and for correlations between the maximum velocity with which neutral sodium falls onto the star and the ratio V/R characterizing the asymmetry of the H_α line but with no positive results.

Figure 4 also shows that the redshifted sodium-doublet absorption components observed on some dates (for example, October 14, 1995) are saturated. Recall that the oscillator strengths for various sodium-doublet resonance transitions differ by a factor of 1.5. Therefore, the fact that the residual intensities are equal indicates that the gas stream moving toward the star in which the absorption features form is opaque to sodium lines and blocks only part of the disk. Similar features were observed in the spectra of certain other UX Ori stars, in both sodium-doublet lines [20] and some other iron lines at UV wavelengths [21]. Still earlier, a similar effect was noted in the spectrum of β Pic and was interpreted using a model in which evaporating cometlike bodies fell onto the star [23, 24].
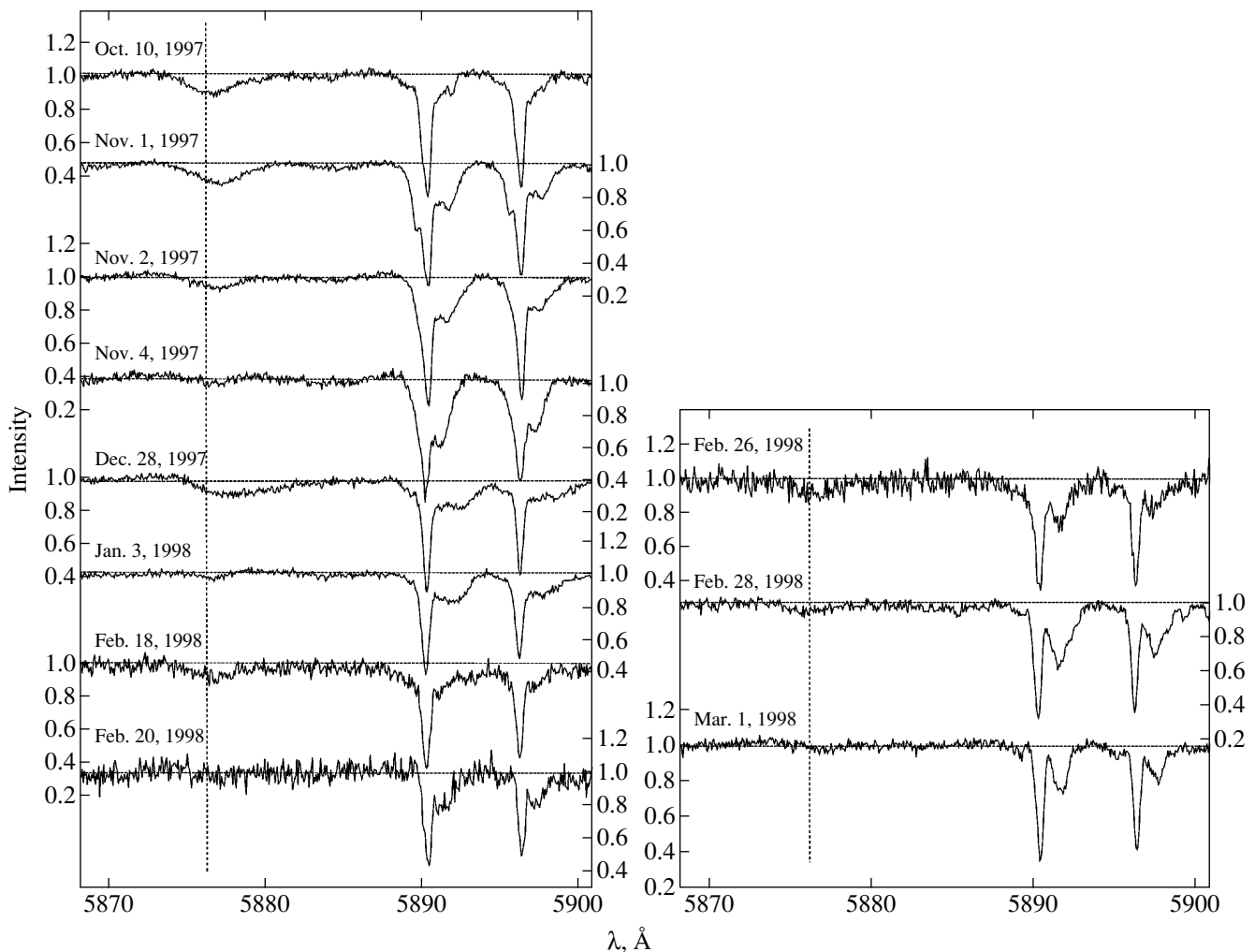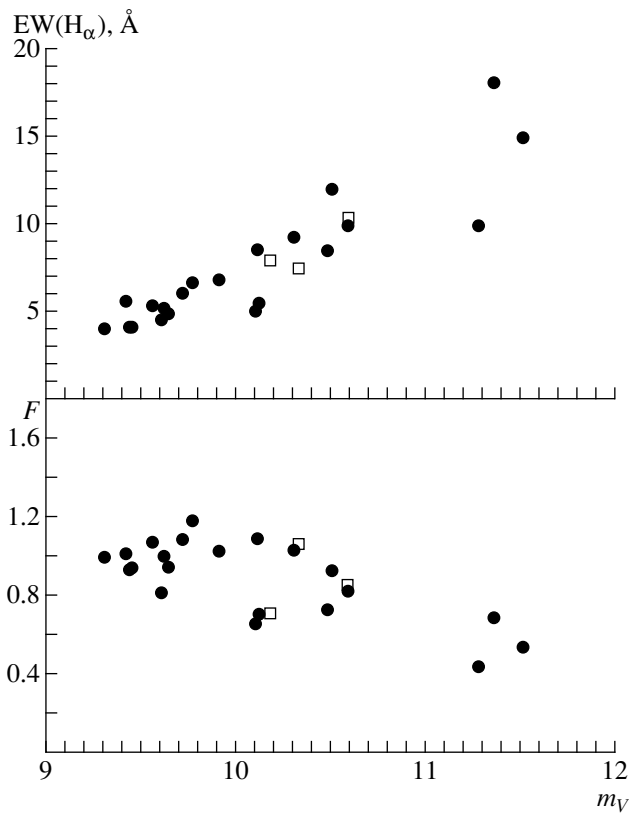

Fig. 4. (Contd.)

Fig. 5. Equivalent width EW and flux F of the H_α line as functions of the brightness of CQ Tau (see text for details).

3.3. The 5876 Å Helium Line

The presence of HeI 5876 Å absorption lines in the spectra of UX Ori stars has been noted in [13, 15, 20, 22]. This is rather unexpected, given that most of these stars have spectral types of A or later, while this helium line appears in the spectra of normal stars only at higher effective temperatures, corresponding to spectral types B5–B7. (For this reason, in some earlier studies of the spectra of Ae/Be Herbig stars, the presence of the 5876 Å line was considered a sign that the stars had earlier spectral types). According to [13–15], the appearance of this line in the spectra of UX Ori stars is associated with the formation of hot regions in the inner layers of the accretions disks around these stars. This can explain the rapid variability of this line, as well as the appearance in some spectra of a weak emission component blueward of the absorption.

As we can see from Fig. 4, the 5876 Å HeI line in the spectrum of CQ Tau is also strongly variable. In most cases, the emission blueward of the absorption is not appreciable, although the general asymmetry of the absorption line about the zero velocity in the star's rest frame[1] indicates that the hot gas is rotating and moving

---

[1] As shown by Finkenzeller and Jankovich [25], the interstellar sodium lines in the spectra of Ae/Be herbig stars correspond with high accuracy to the zero velocity in the star's rest frame.

toward the star. On some dates, the red wing of this line extends to velocities ~ 200–300 km/s. We did not detect any relation between the strengthening of this line and variations in the star's brightness or in the H_α ad D NaI line profiles.

The conditions for forming this line in the accretion disks of UX Ori stars were recently considered by Tambovtseva *et al.* [26], who showed that the temperature of the gas in this region must be no lower than 17000 K. It is natural to associate the appearance of hot gas in the direct vicinity of the star with the dissipation of shock waves that form during interactions between the accreting gas and the stellar magnetosphere.

4. DISCUSSION

The data presented above demonstrate that, during our monitoring of CQ Tau, the most substantial variations in its spectra were observed at times of minimum brightness, when the normally two-component H_α line had a nearly symmetrical single emission component. Simultaneously, there was an increase in the equivalent width EW of the line, with the flux in the line F slightly decreasing. (To estimate the EW and F values, we subtracted the photospheric profile calculated by Kurucz [19] for a model atmosphere for a star of the same spectral type from the observed spectrum.)

As noted above, similar variations of the profile and equivalent width of the H_α line were observed by Kolotilov [14] in the spectrum of UX Ori but were not interpreted. Later, similar variations of the H_α equivalent width at times of deep minima in other stars of this type were observed by Herbst *et al.* [27] and interpreted in the framework of the then-widespread surface-magnetic-activity model. In 1992, during a deep minimum in UX Ori's brightness, de Winter first observed the spectrum of this star with high resolution (see [15]) and confirmed the reality of the unusual variations of the H_α-line profile observed earlier by Kolotilov [14]. The calculations of [28] indicated that such variations could be explained by a model with variable circumstellar extinction if the dust cloud intersecting the line of sight was sufficiently large to block not only the star itself, but also the inner region of the more extended gaseous envelope in which the emission and part of the absorption spectrum are formed.

In this way, the variations of the H_α profile observed in two deep minima of CQ Tau could be due to blocking of the inner part of the star's gaseous envelope by a dust cloud. According to [28], the characteristic size of the cloud must be of the order of 5–6 R_*. In the case of CQ Tau, taking into account the data in Table 1, this corresponds to roughly 10^{12} cm.

Figure 5 presents the dependences of the equivalent width and flux of the H_α emission line on the brightness of CQ Tau for all dates on which we obtained simultaneous or quasi-simultaneous brightness measurements. (In addition to the data presented here, we used spectra

of CQ Tau we obtained on the Nordic Optical Telescope [16]). It is clear that both parameters vary systematically with the brightness: As the brightness decreases, the H_α equivalent width grows and the flux drops. Thus, the observed variations of EW and F with brightness are also consistent with a model with variable circumstellar extinction [28].

Based on the estimate for the size of the dust cloud presented above and the fact that the star's brightness can decrease by an entire magnitude over the course of a day (Table 2), we find that the tangential velocity of the cloud intersecting the line of sight is of the order of 50 km/s. In the case of circular Keplerian motion and a mass for the star of 1.5 $M_\odot$ (Table 1), the radius of the cloud's orbit is ~0.5 AU (if its orbit is not circular, this radius will be even smaller). It is straightforward to show that, to order of magnitude, this distance corresponds to the radius of the zone in which silicate particles will be sublimated in the radiation field of the star. This could explain the relation between the appearance of low-velocity emission and absorption sodium features in the spectra of CQ Tau and the star's Algol-like brightness decreases.

The formation of the sodium resonance doublet in the immediate vicinities of UX Ori stars (as is indicated by the velocity of the infalling material) is rather puzzling. The reason is that this element could be easily ionized by the star's radiation (its ionization potential is 5.17 eV). Even in CQ Tau—one of the youngest UX Ori stars—the photospheric neutral-sodium line is very weak (Fig. 3). This led to one of the hypotheses proposed to explain this observational fact, based on the idea that the circumstellar sodium line forms in dust clouds evaporated near the star [15, 29]. This hypothesis is supported by a number of observational facts (see the review [6] and references therein) and provides a rather close analogy with β Pic.

An alternative hypothesis [29] is based on the idea that the accretion of material onto UX Ori stars should be described using magnetospheric-accretion models of the sort applied to young low-mass T Tauri stars [30]. In this case, the accreting gas can have a normal chemical composition, but in order for a sufficiently large number of sodium atoms to be along the line of sight, the gas must have a high density and, consequently, a high accretion rate of the order of 3 × 10^{-7} $M_\odot$/yr; this substantially exceeds the estimate of [26], derived via modeling of the hydrogen lines. The D NaI profile observed in the spectrum of CQ Tau is also different from both the typical sodium-doublet profiles in the spectra of T Tauri stars and from theoretical profiles obtained using magnetospheric-accretion models [30]. In this latter case, the line has an intense emission component, which is virtually completely absent from the spectrum of CQ Tau (Fig. 3). This indicates that the gas falling onto the star and scattering its radiation at resonance-line frequencies occupies a solid angle that is small compared to 4π, which is also the case for β Pic.

Thus, neither of the accretion models considered can completely describe the observations. It is possible that this indicates that both mechanisms act simultaneously.

5. CONCLUSION

We will now briefly summarize our main results. Our estimates confirm the conclusion drawn earlier in [31] based on an analysis of the photopolarimetric activity of UX Ori stars: The circumstellar dust clouds giving rise to the observed Algol-like brightness decreases could approach rather close to the star. Falling into the dust-sublimation zone, they are evaporated by the star's radiation. As a result, the circumstellar material accreting onto the star, being locally enriched in heavy elements, can be very inhomogeneous in both its density and its chemical composition. This is probably a general property of many accreting young stars but is clearly observationally manifest only in the spectra of UX Ori stars, which are observed directly through the circumstellar-disk material. Thus, the inhomogeneity of the accreting material (including its chemical inhomogeneity) is one source of the spectral variability of CQ Tau.

Another type of spectral variability of CQ Tau is associated with a purely geometric effect—screening of the stellar disk and the inner part of the accretion disk, where the emission and part of the absorption spectrum is formed, by dust clouds. The clearest form of this variability was observed twice during deep brightness minima, when the usual two-component H_α emission profile had only one component. The effect of screening can also explain the increase in the H_α equivalent width observed during decreases in the star's brightness.

REFERENCES

1. W. Wenzel, *Non Periodic Phenomena in Variable Stars* (Academic, 1969), p. 61.
2. V. P. Grinin, Pis'ma Astron. Zh. **14**, 65 (1988).
3. V. P. Grinin, N. N. Kiselev, N. Kh. Minikulov, *et al.*, Astrophys. Space Sci. **186**, 283 (1991).
4. V. P. Grinin, Astron. Astrophys. Trans. **3**, 17 (1992).
5. P. S. Thé, *The Nature and Evolutionary Status of Herbig Ae/Be Stars* (ASPC **62**, San Francisco, 1994), p. 31.
6. M. R. Pérez and C. A. Grady, Space Sci. Rev. **82**, 407 (1997).
7. V. P. Grinin and A. N. Rostopchina, Astron. Zh. **73**, 194 (1996).
8. A. Natta, V. P. Grinin, V. Mannings, *et al.*, Astrophys. J. **491**, 885 (1997).

9. A. V. Berdyugin, S. V. Berdyugina, V. P. Grinin, *et al.*, Astron. Zh. **67**, 812 (1990).

10. A. N. Rostopchina, Astron. Zh. **76**, 113 (1999).

11. *The Hipparcos Catalog* (ESA, SP-1200, 1997).

12. V. Piirola, Ann. Acad. Sci. **418**, 61 (1975).

13. O. V. Kozlova, V. P. Grinin, and A. N. Rostopchina, Astron. Astrophys. Trans. **8**, 249 (1995).

14. E. A. Kolotilov, Astrofizika **13**, 33 (1977).

15. V. P. Grinin, P. S. Thé, D. de Winter, *et al.*, Astron. Astrophys. **292**, 165 (1994).

16. V. P. Grinin, A. Natta, O. V. Kozlova, *et al.*, 1999, in preparation.

17. N. E. Piskunov, *Stellar Magnetism*, edited by Yu. V. Glagolevskiĭ and I. I. Romanyuk (Nauka, St. Peterburg, 1992), p. 92.

18. N. E. Piskunov, F. Kupka, T. A. Ryabchikova, *et al.*, Astron. Astrophys., Suppl. Ser. **112**, 525 (1995).

19. R. L. Kurucz, *CD-ROM 13*, 1993.

20. V. P. Grinin, O. V. Kozlova, P. S. Thé, *et al.*, Astron. Astrophys. **309**, 474 (1996).

21. C. Grady, M. R. Pérez, A. Talavera, *et al.*, Astron. Astrophys., Suppl. Ser. **120**, 157 (1996).

22. D. de Winter, C. Grady, M. E. van den Ancker, *et al.*, Astron. Astrophys. **343**, 137 (1999).

23. R. Ferlet, A. M. Lagrange-Henri, H. Beust, *et al.*, Astron. Astrophys. **267**, 137 (1987).

24. A. M. Lagrange-Henri, A. Vidal-Madjar, and R. Ferlet, Astron. Astrophys. **190**, 275 (1988).

25. U. Finkenzeller and I. Jankovich, Astron. Astrophys., Suppl. Ser. **57**, 285 (1983).

26. L. V. Tambovtseva, V. P. Grinin, and O. V. Kozlova, Astrofizika **42**, 75 (1999).

27. W. Herbst, J. A. Holtzman, and R. S. Klasky, Astron. J. **88**, 1648 (1983).

28. V. P. Grinin and L. V. Tambovtseva, Astron. Astrophys. **293**, 396 (1995).

29. C. Sorelli, V. P. Grinin, and A. Natta, Astron. Astrophys. **309**, 155 (1996).

30. J. Muzerolle, L. Hartmann, and N. Calvet, Astron. J. **116**, 455 (1998).

31. V. P. Grinin, *the Nature and Evolutionary Status of Herbig Ae/Be Stars*, Edited by P. S. Thé, M. R. Pérez, and E. P. J. van den Heuvel (ASPC **62**, San Francisco, 1994), p. 31.

Translated by D. Gabuzda

The Unusual Profile of the Radio Pulsar Geminga

V. M. Malofeev and O. I. Malov

Pushchino Radio Astronomy Observatory, Astro Space Center of the Lebedev Institute of Physics,
Russian Academy of Sciences, Pushchino, Moscow oblast, 142292 Russia
Received December 9, 1998

Abstract—The results of observations of the radio emission profiles of the Geminga pulsar at 102.5, 87, 58, and 39 MHz are reported. Individual pulses are presented for the first time, and rare occasions of strong emission over the entire pulsar rotation period have been detected. A detailed analysis of the shapes, durations, and arrival phases of the pulses at 102.5 MHz is presented. These data reflect the unique character of the radio emission of Geminga. © *2000 MAIK "Nauka/Interperiodica"*.

1. INTRODUCTION

The nature of the first gamma-ray source Geminga [1] was revealed after the detection of a pulsar, first in X-rays [2] and then in gamma rays [3]. A preliminary identification of Geminga with a weak $25^{\mathrm{m}}.5$ optical object [4] was recently confirmed via measurement of its parallax, from which it was possible to determine the distance to the object, equal to $157 \pm^{59}_{34}$ pc [5]. Geminga is, thus, a nearby, young neutron star with all attributes typical of the rare group of "multiwavelength" objects, which includes the famous young Crab and Vela pulsars, which reside in supernova remnants. These objects radiate over the entire electromagnetic spectrum, from gamma to radio wavelengths. This made the lack of detectable radio emission in Geminga, which turned out to be the nearest object of this group, all the more surprising. Moreover, until recently, all pulsars had first been discovered at radio frequencies, including those that are more than ten times more distant than Geminga. Most "multiwavelength" pulsars are strong radio objects. Until recently, only Geminga remained the only "radio quiet" pulsar, in spite of numerous attempts to find either stationary or pulsed emission (see References in [6]), including observations using the largest radio telescopes in the world.

Finally, at the end of 1996, the uniquenesses of this object was put in doubt. Three research groups at the Pushchino Radio Astronomy Observatory independently detected pulsed radio emission from Geminga [6–8]. All three groups used the same radio telescope and receiving equipment but applied different observing and data-processing methods. They obtained different flux densities, shapes, and widths for the integrated pulse but similar values for the dispersion measure. We perform a more detailed comparison of the profiles and consider probable reasons for these discrepancies below.

The presence of pulsed radio emission at the nearby frequency of 103 MHz has already been confirmed by one group from India [9]. At the same time, attempts to detect the pulsar at the higher frequencies 317–410 MHz [10–12] and 1400 MHz [12], and at the lower frequency 35 MHz [11] have thus far been unsuccessful. In 1997–1998, we undertook intensive studies (partially reported in [6]) at 102.5 MHz and other meterwave frequencies using the DKR-1000, the other large radio telescope of the Lebedev Institute of Physics at Pushchino. These observations yielded positive results at the lower frequencies of 61 and 41 MHz [13]. In the current paper, we present integrated (group and individual) pulses of Geminga at four frequencies: 102.5, 58, 41, and, for the first time, 87 MHz. In addition, we present a detailed analysis of the profile shapes and their arrival phases at 102.5 MHz.

2. OBSERVATIONS

Detailed information about the antenna, receiving equipment, observation procedure, data processing, and probable flux-measurement errors is given in [14] and, in part, in [6]. Here, we will briefly present parameters relevant to our observations of the Geminga pulsar.

The observations were carried out regularly from December 1990 until July 1998 in 16 series with durations of 4 to 14 days. We used the LPA (Large Phased Antenna) meridian radio telescope and the East–West antenna DKR-1000 (Broadband Cross Radio Telescope). On the LPA operating at a frequency of 102.5 ± 2 MHz, the observation time is ~$3.5^{\mathrm{m}}/\cos\delta$ at the half-maximum level of the beam, where δ is the source declination. Thus, we could observe 954 individual pulses of Geminga each day. Due to its large geometrical area, the LPA is one of the most sensitive radio telescopes in the world. The antenna consists of 16 384 dipoles occupying an area of 384×187 square meters; i.e., it has an effective area

$$A_{\mathrm{eff}} \approx 3 \times 10^4 \ \mathrm{m}^2 \cos(\delta - 55°), \tag{1}$$

enabling us to achieve high sensitivity. A detailed calculation of this quantity is given in [14]. As an example, the flux density measured for PSR 0353+52 at 102.5 MHz is $S = 3.5$ mJy. The East–West DKR-1000 antenna operates at 30–110 MHz and has a geometrical area of $2 \times 10^4 \, \text{m}^2$. Due to the scanning system used, the observation time on this telescope is $15^m/\cos\delta$. The effective area depends on frequency and has a maximum at 80–90 MHz. The effective area is estimated to be $(8–10) \times 10^3 \, \text{m}^2$, enabling us to measure the fluxes and study the profiles of dozens of pulsars at low frequencies (see, for example, [15]). The possibility of using another large meter-wave radio telescope for studies of Geminga cannot be overestimated, since the observations at other frequencies not only allowed us to confirm the existence of pulsed emission from this object, but led to new and very important results.

The observations of Geminga were carried out in two regimes. In the first, we usually used 32, and sometimes 64, 96, or 128, channels of an AS-128 spectrum analyzer with a channel passband of 20 kHz. We employed a uniform procedure for the synchronous accumulation of the signal in selected channels during the transit of the pulsar through the radio-telescope beam. The daily time for the start of the signal recording was calculated beforehand in order to preserve the arrival phase of the pulse. For this calculation, we used the period and its derivative $(P, \dot{P})$, the coordinates given in the catalog of Taylor et al. [16], and the software of Shabanova [17]. During the observations, we used the time-service signals of our observatory [18]. Virtually all the observations in this regime were carried out with a receiver time constant of 3 ms and sampling interval of 2.56 ms. In order to precisely measure the pulsar flux, we fed in a noise-generator signal during the first 15 readings, which was calibrated against discrete radio sources with known flux densities (see details in [14]). The observations were carried out with a measuring complex based on an AT-486 personal computer [19]. To ensure certain identification of the pulsar pulse, all integrations were carried out with double or triple the observation period (i.e., $P_H = 0.237 \, s \times 2$ or $P_H = 0.237 \, s \times 3$). This procedure was thoroughly mastered during our survey of faint pulsars [14].

In the second regime, the individual pulses were recorded over a time window corresponding to 10 pulsar periods (i.e., $P_H = 0.237 \, s \times 10$). In a single observing session, we collected 90 such groups of pulses on the LPA and 410 on the DKR-1000 antenna. To improve the signal-to-noise ratio, we used a time constant of 10 ms and sampling interval of 7.68 ms. In approximately half the sessions, the recording regime was such that each of the ten periods in the time window itself represented the sum of two (or five) pulsar periods. In addition, to reduce the data volume, in the individual pulse mode, we used only 16 20-kHz channels at each frequency. This enabled us to study emission intensity variations within an observing session.

3. DATA PROCESSING AND RESULTS

The observations yielded files containing the pulsar signal, either accumulated with the observed period ($2P$ or $3P$) or in groups of pulses with $P_H = 10P$ in all channels. The data processing included a search for the "zero" level in each channel, gain equalization using a calibration signal, rejection of channels affected by interference according to two criteria (the gain factor and ratio of the noise σ in the current and reference channels, see [14] for details), elimination of the segment with the calibration signal, and summation of the signal in all channels taking into account the time shift due to the dispersion delay of the signal in the analyzer passband. We then determined the new "zero" level, calculated a moving average of either five or three points with a resolution of 2.56 and 7.68 ms, respectively, and calculated or estimated the pulse energy.

We now give some more details about the criteria used to remove channels with interference. We applied both a traditional procedure, comparing the σ in all channels with those in reference channels, and compared calibration signals. Both criteria frequently worked together, but in many cases, the latter was more sensitive to interference that raised the overall level but left σ nearly unchanged. Note that the removal of channels affected by interference is a very efficient way to battle stationary radio stations, but this procedure does not completely eliminate weak random pulsed industrial interference; therefore, a very important aspect of the processing was separating the pulsar signal from the remaining interference. For most of the pulsars in our survey [14], this procedure has been completed and yielded very good results. It was also applied to the Geminga observation, but here, we encountered some difficulties. Geminga's signal has an unusual character. Nothing similar has been observed for any other radio pulsar. First, its flux, pulse duration (over wide limits), profile shape [6], and pulse arrival phase (see details below) vary from day to day. Thus, in the case of Geminga, the standard procedure for detection of the phase of the pulsed signal via summation of several days of observations sometimes failed. Second, checking the dispersion delay of a pulse was possible only for strong signals. Third, the magnitude of the dispersion is very small (2.9 pc/cm^3 [6]), and the expected delay was only 4–5 sampling points (readings), even for the edge frequencies, when observing with 32 channels at 102.5 MHz (though it was measurable at 58 and 41 MHz). However, this procedure successfully selected interference whose amplitude was maximum and duration was minimum when the dispersion measure was set to zero.

3.1. The Integrated Profile

First we will spend some time on the 102.5-MHz observations, since they are the most numerous. Analysis of profiles integrated over several hundred periods per day and then summed over several days (i.e., thou-

sands of periods) showed that the profile shape is not stable [6]. There remained the hope that the summed profile obtained by integrating some 27507 periods (from the data of the first half-year of observations) would prove stable and provide an identity card for Geminga, as is the case for profiles obtained for other pulsars after accumulation over several hundred periods. To check this hypothesis, we continued observations of Geminga at 102.5 MHz.

Figure 1 presents the mean profiles obtained over four observing sessions, carried out during the seven subsequent months. As earlier, the summed profiles for individual sessions demonstrate a wide variety of shapes and durations. Furthermore, in two sessions (August and December), we observed an interpulse at the end of the period, which was not clearly visible in the summed profiles in any of the sessions in the first half-year of observations. Note that, in all four sessions, the mean profile has two or more components, and the summed profile width at half-maximum is larger.

In the August session, the dashed curve shows a comparison signal accumulated over eight days of observations in a direction close to Geminga with the same parameters as for Geminga. This noise signal was reduced to the same gain as the observation of Geminga and clearly demonstrates the noise level and the level of probable weak interference. We can see that, in this session, the amplitude of the signal from Geminga is from 3σ (left-hand components) to 5σ for the interpulse (right components). The most surprising thing, however, is that the sum of all the sessions in the second half of the year (28560 periods) yielded a profile that was again different from that obtained from approximately the same number of periods accumulated in the first six months [6]. Thus, 30000 periods appear to be insufficient to obtain a stable profile. This amazing fact obviously separates out Geminga from other radio pulsars. At first, it seemed that our receiving passband was insufficiently wide to smooth signal frequency variations due to scintillations on inhomogeneities of the interstellar medium. But two facts show that this is not the case.

First, broadband observations (with 64, 96, and 128 channels; i.e., 1.28, 1.92, and 2.56 MHz, respectively) also do not yield a stable profile shape and pulse width. Second, for strong pulses, we observed a signal even in individual groups of channels separated by hundreds of kHz. An estimate of the characteristic scale of scintillations on the three days with strong pulses yields 400–800 kHz; recalculating it to the radius of frequency correlation gives a value close to 80–160 kHz. This is fairly typical for nearby pulsars in our wavelength range [20], and, consequently, the behavior of the profile of Geminga should be similar to that of other pulsars—for example, PSR 0950+08, in which, from time to time, a minor change of the profile shape is
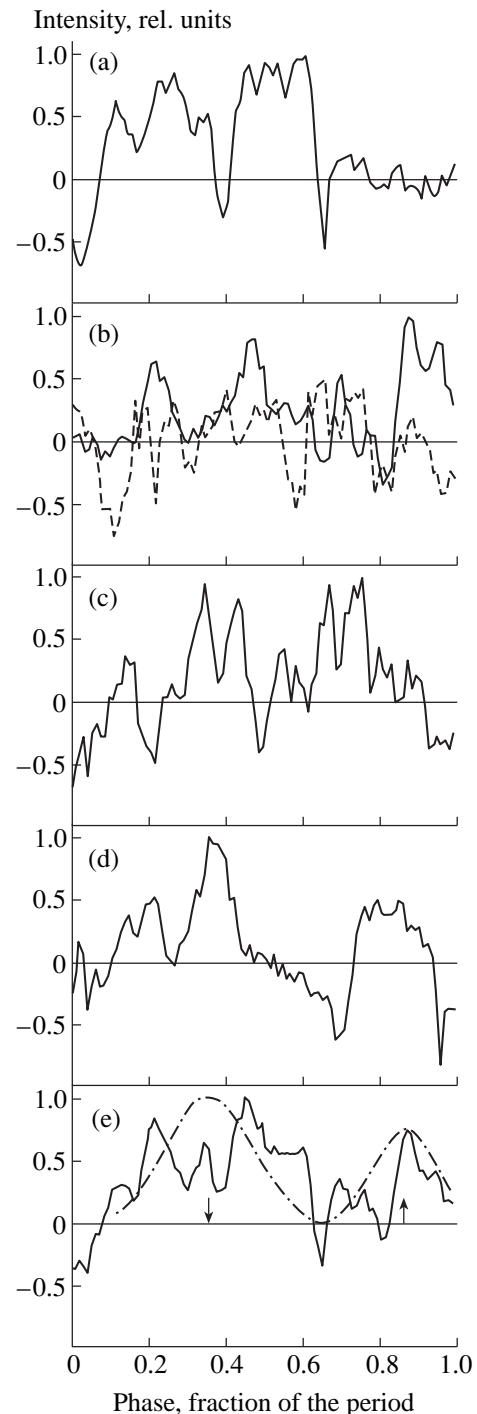
Fig. 1. Integrated profiles of Geminga at 102.5 MHz obtained in four observational sessions: (a) July 6–7, 1997 (7 days, 6700 periods); (b) August 1997 (14 days, 8904 periods), the dotted curve shows the summed signal for 8 days of test observations; (c) November 1997 (4 days, 2864 periods); (d) December 1997 (6 days, 10092 periods); (e) the total of the four sessions (31 days, 28 560 periods), the dashed curve describes the envelope of the main pulse (the downward arrow shows the mean phase) and interpulse (the upward arrow shows the mean phase). The width of the envelope corresponds to 2σ of the distribution of the durations of the main pulse and interpulse, which are presented in Figs. 4a, 4b; the distributions of the arrival phases of the centers of the main pulse and interpulse are given in Figs. 4c, 4d.

Number of days
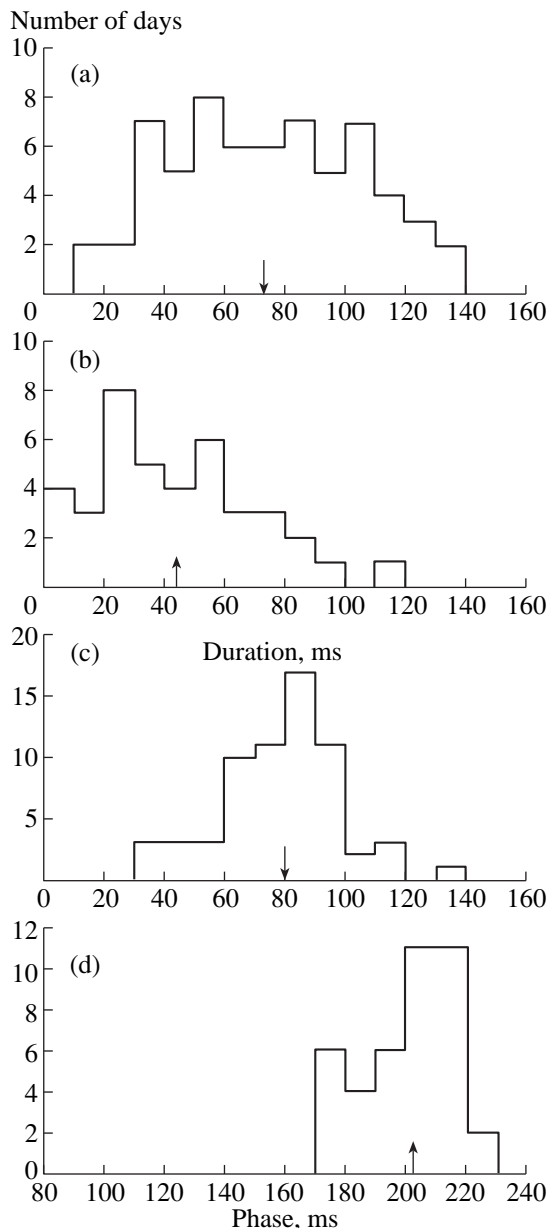
Fig. 2. Histograms of the durations of the (a) main pulse and (b) interpulse at 102.5 MHz and the arrival phases of the centers of the (c) main pulse and (d) interpulse. The arrows on the axis show the (a) and (b) mean durations and (c and d) mean arrival phases of the main pulse and interpulse.

observed, but the duration varies only by about ten milliseconds.

Shitov and Pugachev [8] estimated the probable radius of frequency correlation at 102.5 MHz using the statistical correlation of pulse broadening due to scattering in the interstellar medium with the dispersion measure; it proved to be 100 kHz. They also estimated this quantity to be 180 kHz for one day (November 15, 1996). Both values are close to our measurements. We already noted in [6] that the profiles accumulated over 300 to 900 periods over one day substantially differ in

both duration and shape. New observational sessions confirm this. In 23% of 83 days without strong interference (there were 105 days of observation in all), we saw only a noiselike signal, when the pulsed component did not exceed $(2–3)\sigma$. In 19% of cases, there was a narrow pulse with approximately the same phase as in the summed profile in Fig. 1. Broad profiles with two or more components were observed in 44% of cases. Very broad profiles, which, as a rule, had large fluxes, were visible on 14% of days. Finally, an interpulse with a phase near $0.75P–1.0P$ was recorded on 39 of 83 days, when the signal exceeded 3σ, and, on some days, the intensity of the interpulse exceeded that of the main pulse.

In order to identify the signal of Geminga with certainty, we always used observations with double or triple the accumulation period. As controls, we observed strong and weak pulsars in a similar mode. For normal pulsars, two or three independent accumulated profiles very seldom differed in the details of their shape or by more than 20% in amplitude, but Geminga again presented a surprise. In only 39% of cases did we observe two of two or three of three pulses. Moreover, quite frequently, the pulse shape and duration differed appreciably.

The histograms in Figs. 2a and 2b can be used to obtain a more complete picture of the distributions of the main pulse and interpulse durations at 102.5 MHz. These distributions are unusually broad, occupying about half the period and only vaguely resembling a normal distribution. Figures 2c and 2d present histograms of the arrival phases for the centers of the main pulse and interpulse, measured at the half-maximum pulse amplitudes. These are already closer to normal distributions, especially that for the main pulse, but they are also unusually broad and occupy up to one-third of the period. The statistical averages of the arrival phases of the main pulse and interpulse are 80 ms and 208 ms, respectively, so that the separation between the main pulse and interpulse is 0.51 ± 0.07 pulsar periods; this is quite similar to the situation at gamma-ray energies [21]. For comparison, the scatter of the period durations and arrival phases for PSR 0950+08, observed as a reference pulsar over 30 days at the same frequency and using the same method as for Geminga are $\Delta W_{0.5} = 12$ ms $= 0.05P$, $\Delta\Phi \sim 30$ ms $\approx 0.12P$. Note that this pulsar is not typical, since it has a composite pulse shape with a high degree of linear polarization and complicated behavior of the polarization position angle [22]. At our frequency, since the antenna receiver is sensitive to linearly polarized radiation, the pulsar shape changes strongly from day to day, so that the pulse centroid also shifts. In most pulsars, these quantities vary within one percent of the period.

Figure 3 presents examples of the mean profiles at 87 MHz (Figs. 3a, 3b), 58 MHz (Fig. 3c), and 39 MHz (Fig. 3d). The profile in Fig. 3a is presented with the double period for one day of observations. This example of very strong emission demonstrates the rare recurrence, in detail, of the two shapes of the mean pulses

near 240° and 600°, independently accumulated over 1372 periods. Figure 3b presents a convolution of the upper profile. This is a broad, composite profile, occupying more than half the period and probably containing three to four components.

Examples of summed mean profiles for several days of observations at 58 and 39 MHz are presented in Figs. 3c and 3d. In spite of the poor statistics (13–18 days of observations at each frequency), the duration of the profile remains, on average, constant as the frequency changes, though a tendency for increasing duration with decreasing frequency was observed earlier. In the table, we list these quantities at the 0.5 amplitude level, with the number of periods accumulated indicated.

The emission of pulsars differs from that of other radio sources in two ways: The periodicity and frequency dispersion of the signal. Figures 1 and 3 present examples of summed periodic signals; however, to be fully convinced of the presence of pulsar-type emission, we present in Fig. 4 a magnificent example of strong emission from Geminga at 40.9 MHz on August 21, 1997, demonstrating the frequency dispersion of the signal. The observations were carried out with the double accumulation period, and each profile is a signal compensated and summed over eight frequency channels (in each case 318 double periods were combined).

3.2. Individual Pulses

The very unusual behavior of the shape and phase of the Geminga mean profile could most likely be explained in two ways. The first is the presence of rare but very strong pulses, and the second is a permanent random wandering of the arrival phase of the pulses in two windows, each covering one-third of the period (Figs. 2c, 2d). To test these possibilities, we carried out at least two observing sessions at each of the four frequencies (102.5, 87, 60, and 41 MHz) in the group (sometimes individual) integration regime. These observations yielded very valuable additional information about the radio emission of Geminga.

However, before proceeding to the results for Geminga, we show the profile of the test pulsar PSR 0950+08 for May 12, 1998, obtained in the same recording regime. Figure 5a presents a group of pulses accumulated using 10 pulsar periods, i.e., $P_{obs} = 10P$. Each pulse in the window represents the sum of six periods. Figure 5b shows a convolution of the upper profile with a period of $2P$. Note the surprising stability of the phase and duration of the pulses in the upper panel. At the same time, we can see wide scatter of the pulse amplitudes for an integration over six pulsar periods. However, the profiles accumulated over 24 periods (Fig. 5b) are already virtually indistinguishable. At phases of 200° and 560°, we can see a weak interpulse with an amplitude of about 4% of the main pulse.

Surprisingly, in the observations of Geminga, among the huge number of pulse groups considered, we
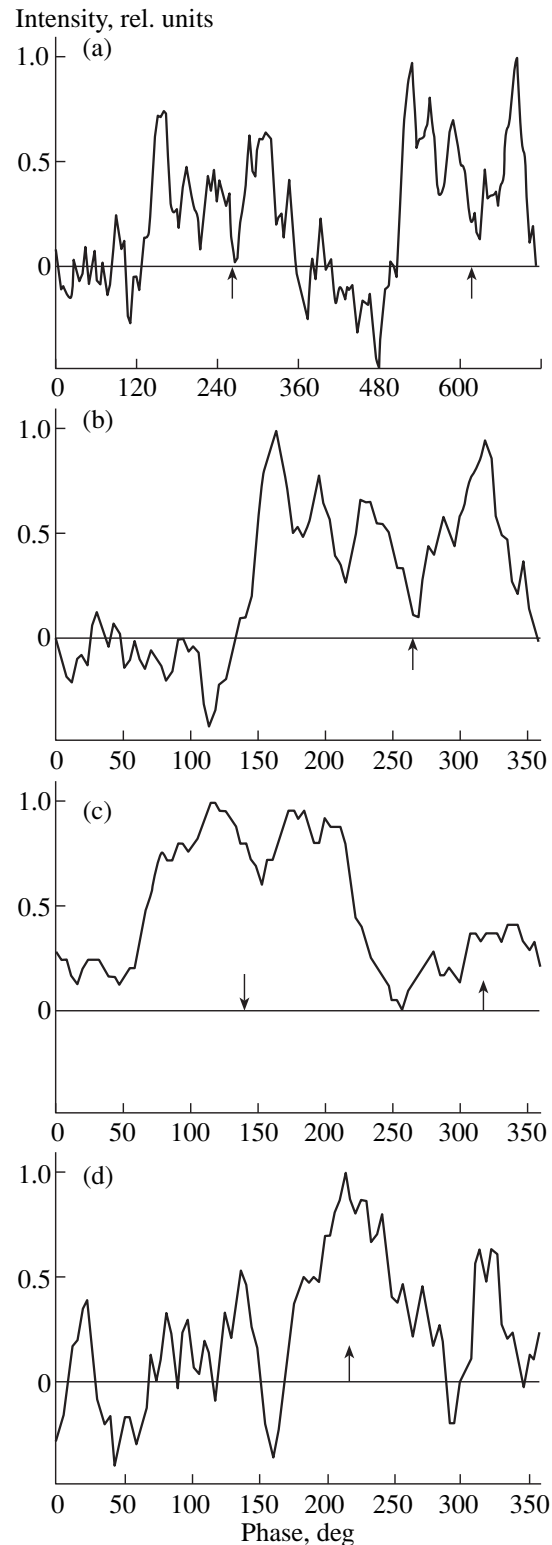
Fig. 3. Examples of integrated pulses at three frequencies: (a) double period, 87 MHz, January 27, 1998, total 1372 periods; (b) period of profile (a) convolved with the total over 2744 periods; (c) total of five days, or 9472 periods, 58.746 MHz; (d) total of four days, or 9920 periods, 39.046 MHz. The downward and upward arrows indicate arrival phases of the centers of the main pulse and interpulse, respectively.

Intensity, rel. units
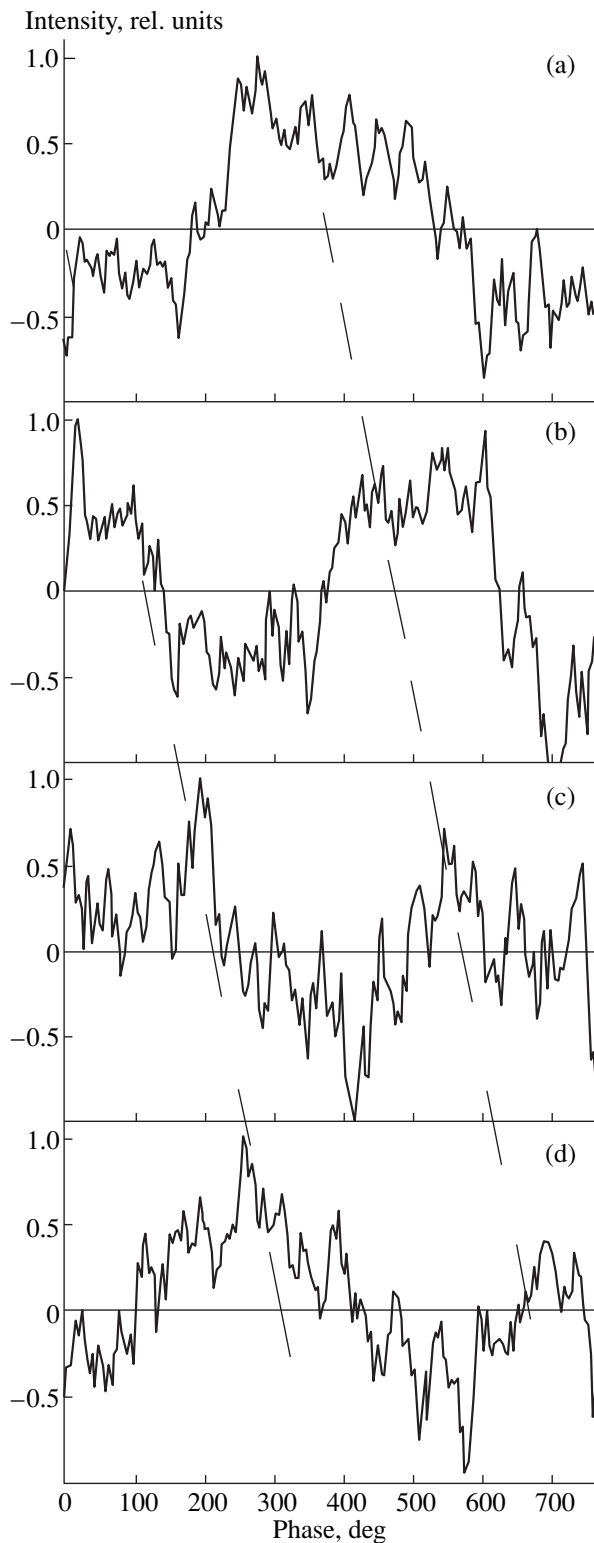
Fig. 4. Example of pulse dispersion at frequencies of about 40.7 MHz for August 21, 1997. From top to bottom, pulses integrated with the double period obtained by integrating 318 pulses and summing over channels are shown: (a) channels 1–8 (40.977–40.817 MHz); (b) 9–16 (40.817–40.657 MHz); (c) 17–24 (40.657–40.497 MHz); (d) 25–32 (40.497–40.337 MHz). The dotted curve shows the expected position of the pulses for a dispersion measure of 2.9 pc/cm³.

Intensity, rel. units
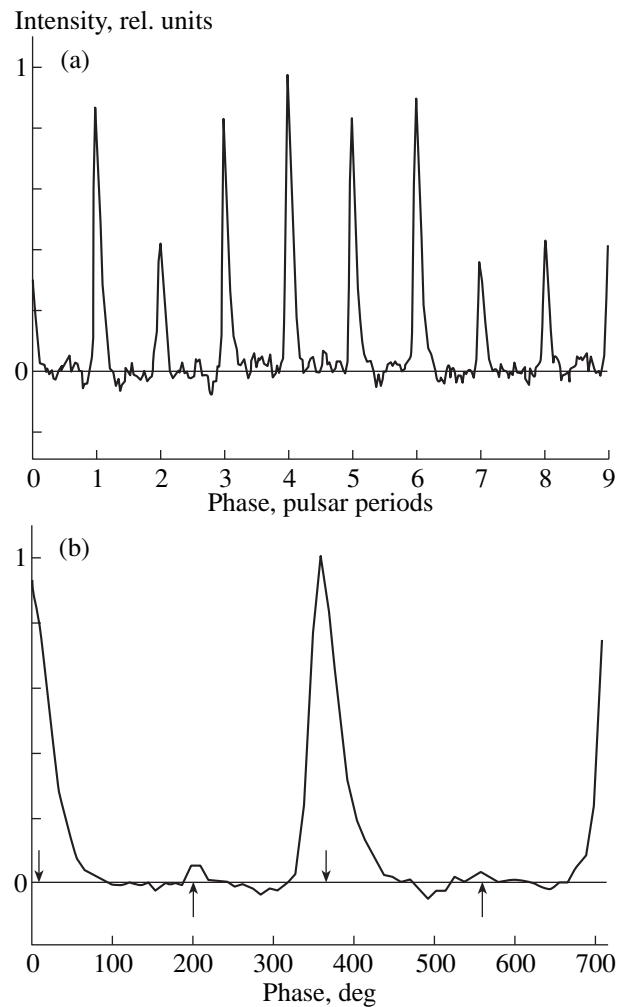
Fig. 5. Observation of PSR 0950+08 at 102.5 MHz for May 15, 1998: (a) Group 31 contains a time interval P_H equal to 10 pulsar periods, and the integration carried out over $6P_H$; (b) integrated profile of the same group obtained by convolving the data with P_H equal to two pulsar periods. The downward and upward arrows on the X axis show the arrival phases of the centers of the main pulse and interpulse, respectively.

found several obviously strong groups with an appreciable periodic signal at all four frequencies. The pulse appeared not only in short integrations (5 periods), but, in some cases, even in the individual pulse recording regime.

Figure 6 shows pulses of a group with period $P_H = 10P$ (at 102.5 MHz) accumulated on May 11, 1998. We can see five to six pulses with the period of Geminga (Fig. 6a). Figure 6b shows the convolution of the upper profiles over nine Geminga periods. The downward arrows show the phase of the main pulse (aligned with the phases of the integrated pulses in Fig. 1) and the upward arrow the phase of the interpulse in Fig. 6. Though we talk about summing five periods in Fig. 6a and 45 in Fig. 6b, in fact, we do not know how many actual pulses participated in the sum. There could be from one to five for the top

Durations of integrated pulses at the half-maximum (N is the number of integration periods, M is the number of days of observation)

Frequency, MHz	Main pulse			Interpulse		
	duration, ms	$N, 10^4$	M	duration, ms	$N, 10^4$	M
102.5	73 ± 31	4.4	64	44 ± 27	2.3	39
87.5	71 ± 24	3.5	13	70 ± 37	3.8	15
58.7	63 ± 23	3.5	18	63 ± 28	3.2	16
40	69 ± 33	2.2	14	62 ± 27	3.3	16

panel and from five to 45 for the bottom panel. We can speak more definitely about individual pulses at 58 MHz, where it was possible to find a group (number 162) of six individual pulses on July 23, 1998. Even at 41 MHz on July 22, 1998 (Fig. 7), we could find a group of four strong individual interpulses and main pulses. Gener-

ally, the double-period profile (Fig. 7b) for this group is one of the best examples of two strong main pulses and two slightly weaker interpulses (in a sum of only nine pulsar periods). All the above examples (Figs. 6, 7) convincingly demonstrate the existence of nonrandom radio emission with the period of Geminga.
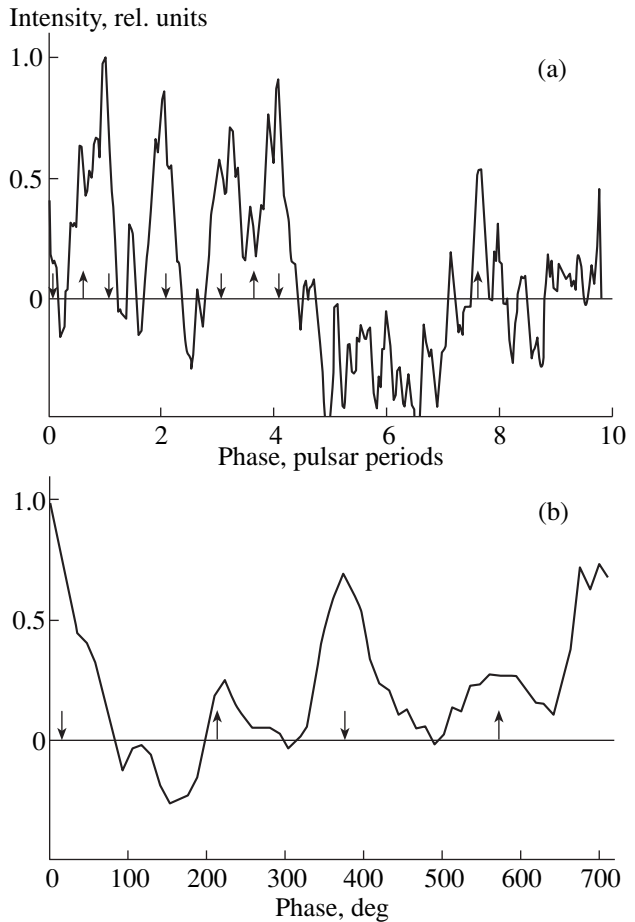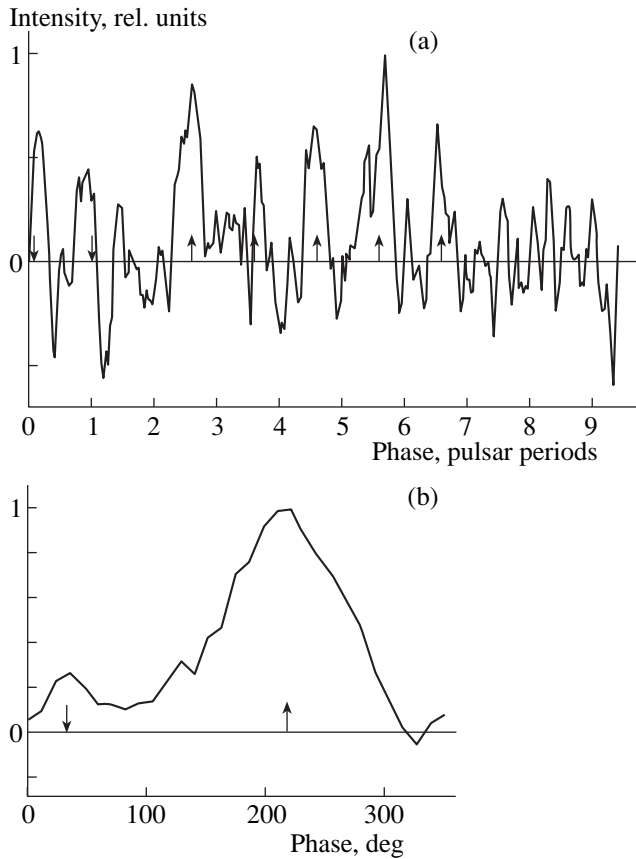
Fig. 6. Observation of Geminga at 102.5 MHz for May 11, 1998: (a) group 50 contains a segment $P_H = 10P$, and the integration is carried out over $5P_H$; (b) integrated profile of the same group obtained by convolving the data with the pulsar period. The downward and upward arrows on the X-axis show the centers of the arrival phases of the main pulse and interpulse, in accordance with the notation and alignment with the phases presented in Figs. 1 and 4.

Fig. 7. Observation of individual pulses of Geminga at 40.976 MHz for July 22, 1998: (a) group 211 contains a segment $P_H = 10P$, and the integration is carried out over $5P_H$; (b) integrated profile of the same group obtained by convolving the data with $P_H = 2P$. The arrows on the X-axis mark the centers of the arrival phases of the main pulse and interpulse, in accordance with Fig. 5d. The pulse arrival phases at 40.976 MHz were recalculated from 39.046 MHz using a dispersion measure of 2.9 pc/cm^3.

Intensity, rel. units
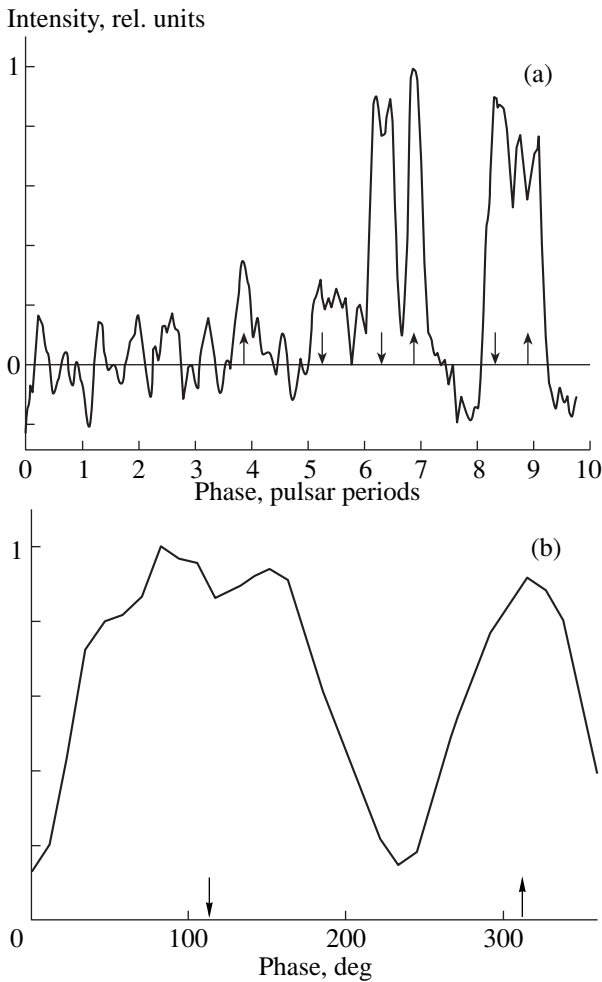
Fig. 8. An example of a group of very strong and broad pulses at 87 MHz for May 12, 1998: (a) group 23 includes a segment containing $P_H = 10P$ (the integration was carried out over $5P_H$); (b) integrated profile of the same group (the main pulse and interpulse were obtained by summing over 45 Geminga periods). The arrows in the upper panel correspond to the centers of the arrival phases of the main pulse and interpulse indicated in the lower panel, which, in turn, are aligned with the mean arrival phases at this frequency for all the days.

Returning to the unusual behavior of the phase and shape of the integrated profile of Geminga, we have established the existence of changes of the arrival phase of pulses and of rare, but very strong, pulses. Several times, we observed a shift of the integrated pulses by 0.1–0.3 of the period in short integrations of 45 periods, separated by an interval of 50–100 Geminga periods; i.e., 12 or 24 s later. The examples in Figs. 6 and 7 show a small shift of the pulse or interpulse arrival phase compared to the expected phase of the integrated pulse (Figs. 1 and 3). While the estimated flux for the previous examples of groups or individual pulses is several Janskys, the estimated flux for the giant pulses and interpulses for May 12, 1998 (group 23) presented in Fig. 8 is tens of Janskys at 87 MHz. This unique record-

ing among many thousands of groups testifies to a strong burst of emission from Geminga lasting from 4 to 20 periods. We observed two giant pulses, repeated after one pulsar period. The first pulse (or the sum of five pulses) had both the main pulse and interpulse, while the second provided a completely unique example of very strong emission during the entire period of revolution of the pulsar. It is natural that, in this case, the summed profile (Fig. 8b) contains the main pulse and interpulse with almost identical amplitudes and a raised zero level. The presence of emission throughout the period can also be traced at 41 MHz (Fig. 7a), though with decreased intensity at the phase of the main pulse (pulse number 3). These examples demonstrate the first case of a pulsar having such strong emission throughout its period. It is known that PSR 0950+08, PSR 0826-34 [23, 24], and some other pulsars [25] display interpulse emission, but this emission has at most about 35% of the main pulse amplitude (in PSR 0826-34), and even then, is present only during about half the period; in the remaining objects, it is smaller than 1% at 400 MHz [25] and smaller than 2% at 102.5 MHz [26]. Below, we summarize the data obtained for groups and individual pulses.

(1) The strong emission of Geminga occurs in portions from one to 50–100 pulses long, since prominent pulse groups (when the signal-to-noise ratio exceeds four) appear in several percent of the (several thousand) recordings. In addition, there are long-term fluctuations with a timescale of several days and, probably, months (details will be given in a forthcoming paper).

(2) Both the main pulse and interpulse are observed in different combinations, either separately or together, with approximately identical signal amplitudes. Therefore, our division into the main pulse and interpulse is purely conventional.

(3) The durations of individual pulses (and integrated pulses as well) vary over a wide range from ~0.1 to 1.0 period (Figs. 7a, 8a).

(4) The arrival phase of both the main pulse and interpulse varies continually and over a wide range, covering up to one-third of the period. At times, this happens in an interval of only several dozen periods.

4. DISCUSSION

One effective criterion for the presence of a periodic signal from Geminga, rather than a random periodic noise signal, is that there be extreme in the dependences of the amplitude and pulse width on a period specified by hand when the pulses within groups are summed. The largest amplitude and shortest duration for a summed pulse should occur at the period of Geminga—i.e., 237 ms—or every 31 readings (one reading = 7.68 ms). We have analyzed the dependences of the amplitude and pulse duration on the specified period, which varied from 28 to 35 readings (from 215 to 269 ms). On almost all these curves, the maximum of the amplitude and minimum of the pulse duration

occur at a period close to 237 ms. The same procedure was used for double and triple periods, when two or three pulses were visible, and, in most cases, the maximum (minimum) was at the period of Geminga. Because of the large ratio of the pulse width to its period, the amplitude maximum and duration minimum are not as sharp as, for example, those of PSR 0950+08.

We should say a few words about the differences in the mean pulse shape at 102.5 MHz obtained by the three Pushchino teams [6–8] (the data on fluxes and dispersions will be discussed in a subsequent paper). From the data of 35 observational sessions considered in [7], the duration of the main pulse was found to be 46 ms—i.e., a factor of 1.6 smaller than our value—and the duration of the main pulse derived from the data for the eight best sessions in [8] is 120 ms, which is also a factor of 1.6 larger than our value. How can this discrepancy be explained? First, if we look at the distribution of durations presented in Fig. 2a, the presence of a significant number of cases with a duration of about 46 ms is obvious, and there are also 16 cases with durations from 100 to 140 ms; this even exceeds the number of similar cases in [8]. Second, as indicated in [7], the mean profile is obtained by summing the profiles for the best cross-correlation for separate days, that is, with a shift of the arrival phase, and this naturally results in an artificial narrowing of the mean profile. Furthermore, some of these data (it is difficult to tell how many, but it is probable that it is rather large fraction, given the recent situation with interference on the LPA) certainly contain pulsed interference, because no information about any cleaning of the data is given in [7]. The presence of strong interference should also appreciably distort the true pattern. Third, Shitov and Pugachev [8] gave examples of integrated pulses with a composite profile, for example, for July 12, 1992, and November 13, 1996, which were obtained using a small time constant (about 2 ms) and consist, in our view, of several components with durations that are considerably shorter than 120 ms. Some profiles for 1998 (for which the duration of 120 ms was measured) were obtained with a large time constant of 19.3 ms, which, naturally, smoothed all the narrow features and broadened the profile of Geminga. Thus, we conclude that there are no real inconsistencies between the different results obtained, and our more varied and rich data set contains all cases presented in [7, 8]. Given the extensive set of pulse shapes and widths shown by Geminga, we suggest that we are dealing with different pulse shapes observed at different epochs.

We should also add a few words about the pulse shapes obtained by other groups at other observatories. One group in India [9] reported only a confirmation of emission from Geminga at the nearby frequency of 103 MHz. Another Indian group [11] concluded that they had not detected radio emission from Geminga, but presented two integrated profiles at 35 MHz. The three criteria they used to test seven 10-minute data sets (their term), in fact, were the same as for our groups: the presence of a pulse when integrated with the Geminga period, the presence of two pulses when integrated with the double
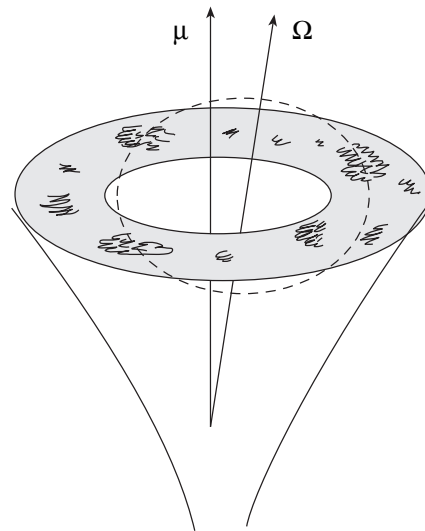
Fig. 9. Schematic representation of a coaxial rotator. The dashed curve shows the trajectory of the observer's line of sight.

period, and the appearance of a spectral feature in the Fourier analysis of a group of ten pulses. For their data set 3, all three criteria yielded a positive result. Nevertheless, they concluded that the signal had a noiselike nature, only because they did not see a certain feature in the second pulse that is present in the first pulse when integrated with the double period over 10 min. We believe that this pulse, as well as the pulse in their data set 7, are pulses from Geminga. This suggestion is based on our above analysis of the emission of Geminga. In almost 60% of successful observations, the strong variability of this object results in an absence of features, and of the second pulse, when integrating with the double period. If we measure the duration of the two profiles presented in [11], it turns out to be ~50 ms at the half-maximum level. This is close to, but slightly smaller than the duration measured by us at the nearby frequency of 40 MHz, where $W_{0.5} = 69$ and 62 ms for the main pulse and interpulse, respectively (table), though we had a larger number (14–16) of 15-min integrations (data sets in the terminology of the Indian group).

The extremely unusual behavior of the radio emission of Geminga, which can appear at different phases of the period (Fig. 2c, 2d) or even occupy the entire period (Fig. 8), forces us to speak more cautiously about stability of the period. There is the impression that the main pulse and interpulse are only the most probable phases of emission, in contrast to the behavior of the overwhelming majority of radio pulsars, in which these phases are strictly fixed. In this sense, the behavior of the radio and gamma-ray emission [21] is very similar; i.e., the emission comes from almost any phase of the period, but the most probable arrival phases lie inside the envelope shown in Fig. 1 by the dot-and-dash curve.

One possible model for the radiating region could be an almost coaxial rotator. Figure 9 shows an approximate

model, in which the observer's line of sight is close to the edge of the emission cone throughout most of the period, where it can cross several regions (spots) of emission. In this model, one necessary condition is that the cone of emission not be circular, but instead be extended along the meridian; this is consistent with, for example, the polarization measurements described in [27] and the model of Malov [28], which can explain some peculiarities of the radio emission of PSR 1822-09. This simple scheme can account for (1) the presence and long duration of the envelopes of both the main pulse and interpulse, (2) the wide variation of the duration and shapes of integrated and individual pulses, and (3) the presence of large changes in the arrival phases of the main pulse and interpulse. However, in this scheme, we attribute the last two effects to selected regions of emission (spots) with varying sizes and separations between them. This is an old idea. There have long been attempts to explain the subpulses and individual pulses of some pulsars using such regions (see, for example, [29, 30]).

The major difficulty is to explain the very rare, strong emission of Geminga over nearly the entire period using this model. In this case, we must invoke either precession of the spin axis or an unexpected, transient rise of the emission region in height, with an associated growth in the size of the hollow cone. Then, the line of sight could for a short time completely sink inside the hollow cone, and, in combination with high activity of the pulsar emission, we could observe emission over the entire period. We understand that this is a very approximate model that requires confirmation and refinement (in particular, taking into account the frequency dependences of the durations, shapes, and arrival phases of the main pulse and interpulse). Recently, at least two theoretical papers [31, 32] have attempted to explain such peculiarities of the radio emission of Geminga as its low radio luminosity and the shape of the radio spectrum. Both papers propose coaxial-rotator models, but, naturally, they do not include explanations for the new peculiarities in the behavior of the durations, shapes, and phases of the pulses of Geminga brought to light by the present study. We hope that such theoretical studies will soon appear.

5. CONCLUSION

(1) From data obtained at four meter-wave frequencies, we have further demonstrated the unusual character of the radio emission of Geminga.

(2) Compared to most radio pulsars, the durations of individual and integrated pulses of Geminga vary over very wide limits: from 15 ms (0.1 of the period) to rare cases (~0.1% of the pulses) when the emission occupies the entire period. The mean duration of the integrated pulse is 73 ± 31 ms, or 0.3 of the period at 102.5 MHz, and the mean interpulse duration is 44 ± 27 ms, or 0.19 of the period.

(3) The arrival phases of the main pulse and interpulse also vary over unusually wide limits (up to one-third of the period). At 102.5 MHz, the interpulse is separated from the main pulse by 0.51 ± 0.09 of the period.

(4) In the emission of Geminga, strong flares with durations from one to several dozen periods are observed, when the flux increases by factors of tens and possibly hundreds. The intensities of the interpulse and main pulse are similar; they can be present either alternately or simultaneously.

(5) We have estimated the radius of frequency correlation of the interstellar scintillations toward Geminga to be 120 ± 60 kHz at 102.5 MHz.

(6) The unusual behavior of the durations, shapes, and arrival phases of the main pulse and interpulse can be explained by a model in which Geminga is a nearly coaxial rotator, so that the observer's line of sight almost never leaves the emission cone of the pulsar. In this case, the shape of an individual pulse is determined by the width and intensity of the emission of individual regions inside the cone, whereas the shape of the integrated profile is determined, in addition, by the number of regions, their possible motions, and their evolution.

(7) Though the detection of pulsed radio emission from Geminga changed this object's classification as a unique multiwavelength radio quiet pulsar, the character of its radio emission gives every indication that Geminga is, nevertheless, a unique radio pulsar.

REFERENCES

1. C. E. Fichtel, R. C. Hartman, D. A. Kniffen, *et al.*, Astrophys. J. **198**, 163 (1975).
2. J. P. Halpern and S. S. Holt, Nature **357**, 222 (1992).
3. D. L. Bertsch, K. T. S. Brazier, C. E. Fichtel, *et al.*, Nature **357**, 306 (1992).
4. G. F. Bignami, P. A. Caraveo, J. A. Paul, *et al.*, Astrophys. J. **319**, 358 (1987).
5. P. A. Caraveo, G. F. Bignami, R. Mignami, and L. G. Taff, Astrophys. J. Lett. **461**, L91 (1996).

6. V. M. Malofeev and O. I. Malov, Nature **389**, 697 (1997).

7. A. D. Kuz'min and B. Ya. Losovskiĭ, Pis'ma Astron. Zh. **23**, 323 (1997).

8. Yu. P. Shitov and V. D. Pugachev, New Astron. **3**, 101 (1997).

9. H. O. Vats, M. R. Deshpande, C. Shah, *et al.*, IAU Circ., No. 6699 (1998).

10. M. A. McLaughlin, J. M. Cordes, T. H. Hankins, *et al.*, Astrophys. J. 1998 (in press).

11. R. Ramachandran, A. A. Deshpande, and C. Indrani, Astron. Astrophys. **339**, 787 (1998).

12. L. Burderi, F. Fauci, and V. Boriakoff, Astrophys. J. Lett. **512**, L59 (1999).

13. Yu. P. Shitov and V. M. Malofeev, IAU Circ., No. 6775 (1997).

14. V. M. Malofeev, O. I. Malov, and N. V. Shchegoleva, in preparation.

15. V. A. Izvekova, A. D. Kuz'min, V. M. Malofeev, *et al.*, Astrophys. Space Sci. **78**, 45 (1981).

16. J. H. Taylor, R. N. Manchester, A. G. Lyne, *et al.*, private communication (1995).

17. T. V. Shabanova, Astrophys. J. **453**, 779 (1995).

18. A. S. Vdovin, Yu. P. Ilyasov, and Yu. A. Fedorov, in *Research in Time and Frequency Measurements, Collection of Scientific Papers* (Gosstandart, Moscow, 1989), p. 46.

19. I. M. Dagkesamanskaya, K. A. Lapaev, and S. V. Logvinenko, *Abstracts of 25th Radio Astronomy Conference* (Pushchino, 1993), p. 234.

20. A. V. Pynzar' and V. I. Shishov, Astron. Zh. **57**, 1187 (1980).

21. G. F. Bignami and P. A. Caraveo, Ann. Rev. Astron. Astrophys. **34**, 331 (1996).

22. S. A. Suleĭmanova, D. V. Volodin, and V. M. Malofeev, Astron. Zh. **60**, 554 (1983).

23. D. C. Backer, V. Boriakoff, and R. N. Manchester, Nature Phys. Sci. **243**, 77 (1973).

24. R. N. Manchester, A. G. Lyne, J. H. Taylor, *et al.*, Mon. Not. R. Astron. Soc. **185**, 409 (1978).

25. T. E. Perry and A. G. Lyne, Mon. Not. R. Astron. Soc. **212**, 489 (1985).

26. T. V. Smirnova and T. V. Shabanova, Astron. Zh. **65**, 117 (1988).

27. R. Narayan and M. Vivekanand, Astrophys. J. **274**, 771 (1983).

28. I. F. Malov, Astron. Zh. **72**, 185 (1995).

29. L. Oster and W. Sieber, Astrophys. J. **203**, 233 (1976).

30. A. G. Lyne and R. N. Manchester, Mon. Not. R. Astron. Soc. **234**, 477 (1988).

31. I. F. Malov, Astron. Zh. **75**, 281 (1998).

32. J. A. Gil, D. G. Khechinashvili, and G. I. Melikidze, Mon. Not. R. Astron. Soc. **298**, 1207 (1998).

Translated by G. Rudnitskiĭ

Hydrodynamic Instabilities and Photospheric Structures

A. V. Getling

Institute of Nuclear Physics, Lomonosov Moscow State University, Moscow, 117234 Russia
E-mail: A.Getling@g23.relcom.ru
Received January 18, 1999

Abstract—The possible role of convective-flow instabilities in the formation of certain structures observed in the solar photospheric and subphotospheric layers is discussed. High-resolution video records suggest that the granulation field is structurally and dynamically ordered in accordance with the mesogranulation pattern. Thus, it strikingly resembles the so-called spoke patterns of convection observed experimentally. These patterns could be produced by some instability of the mesogranular flow. Mesogranules seem to be the main structural features of the velocity field, whereas granules behave as relatively passive elements—blobs of overheated material carried by the mesogranular flow. One possible mechanism for their origin is the development of a three-dimensional analogue of the one-blob or the two-blob instability known from studies of convection. In particular, if this interpretation is adopted, the phenomenon of exploding granules can be accounted for in a natural way. © *2000 MAIK "Nauka/Interperiodica".*

1. INTRODUCTION

The notion that the dynamics of the Sun's convective envelope is at the heart of mechanisms of solar activity can hardly be disputed. This is the main reason why solar convection deserves careful investigation. However, researchers will not be able to understand the dynamics of magnetic fields if they are interested only in averaged characteristics of convective flows. An individual, "deterministic" description of *flow structures* is necessary; however, in solar physics, such approaches remain virtually unexplored.

Meanwhile, the behavior of structures produced by thermal convection has already been investigated fairly comprehensively using methods of fluid mechanics (see, e.g., [1, 2]). In parallel with highly accurate experimental studies, nonlinear theory for the formation and evolution of convective flow patterns is being successfully developed. Heliophysics has gathered a wealth of observational material concerning the above-mentioned layers of the Sun, and considerable progress in this area is being brought about by the development of high-resolution techniques for extra-atmospheric observations and efficient modern tools for experimental data processing.

Advances in these two areas—fluid mechanics and solar physics—provide grounds for attempts to directly identify features observed on the Sun with flow forms known from theory and laboratory experiments. Since the flow structure is highly sensitive to variations in the stratification of physical parameters, there is now even hope for developing diagnostics of the internal structure of subphotospheric layers on the basis of such identifications.

Nevertheless, these two scientific disciplines remain separated by a barrier, for reasons that are more subjective than objective. In many cases, astrophysical theorists who simulate convective flows aim to reproduce as precisely as possible the measured quantitative characteristics of the solar emission. In view of this, various physical mechanisms affecting these characteristics are incorporated in models. Many of these are not of fundamental importance for understanding flow dynamics, but substantially sophisticate the formulation of the problem. Thus, the calculations must be restricted to some spatial region isolated more or less arbitrarily. Moreover, this implies the imposition of artificial boundary conditions. By virtue of the stringent limitations placed, such a statement of the problem may largely predetermine the desired output parameters (which may actually be in good agreement with observations provided that the input parameters are properly chosen, since the visible emission is generated in the uppermost layers of the solar envelope). In this case, however, the general dynamic features of the convective circulation remain completely beyond the scope of the study. In essence, this approach ignores the nonlocal nature of fluid mechanics—the important circumstance that the formation of structures in a given place is governed by the overall flow pattern in the entire region involved (this point is also discussed in [1, 2]).

On the other hand, if relatively simple models are used, which do not reproduce the observed picture in great detail but provide a basis for studying regularities of the flow dynamics, only qualitative inferences can be made. This is likely to reduce the interest of fluid-dynamics researchers in the problem. As a result, the extensive material provided by investigations of hydrodynamic stability and flow-pattern formation remains largely unused by solar physicists, hindering their comprehension of the fundamental dynamical processes involved.

The current study aims to give a qualitative hydrodynamic interpretation to some features of the structure and behavior of the observed photospheric patterns. Such preliminary reasoning serves as a guideline for further investigations based on solving hydrodynamic equations. Initially, it is natural to abstract ourselves from electromagnetic phenomena and to restrict our consideration to quiet regions of the Sun, which are free of strong magnetic fields.

2. THE DISCRETE CHARACTER OF THE SCALE SPECTRUM OF PHOTOSPHERIC FEATURES

One characteristic property of flow patterns in the layers under study is the splitting of their spatial spectra, i.e., the coexistence of structural elements on different scales. In the velocity field, such elements (cells) correspond to mesogranules, supergranules, and, presumably, granules and giant structures. A similar spectrum of characteristic scales is exhibited by structures observed in the distribution of magnetic fields. The basic parameters of the velocity-field cells inferred from observations of granules, mesogranules, and supergranules are given in the table, along with hypothetical parameters of giant cells (which have never been directly observed but whose existence is suggested indirectly).

The coexistence of velocity-field structures differing widely in their scales could result from at least two factors: (1) sharp changes in the parameters of the material at certain heights (associated, e.g., with partial ionization) and (2) the development of small-scale secondary flows as the result of the loss of stability by a larger scale flow. By the *primary* flow, in any particular case, we will mean the flow that, losing its stability, gives rise to *secondary* flows on relatively small scales (this definition is merely conventional, since a secondary flow itself can be primary with respect to flows on even smaller scales, whereas a flow regarded as primary can be secondary for flows on larger scales).

Traditionally, observed patterns are accounted for only in terms of the first type of factor. Such explanations can be traced back to the study of Simon and Leighton [3], who suggested that the coexistence of granulation and supergranulation implied the coexistence of partial-ionization zones for hydrogen and helium in the solar envelope.

It is known that the superisentropic temperature gradient (the absolute value of the difference between the conductive and isentropic gradient) varies widely in the solar convection zone, depending on the degrees of ionization of hydrogen and helium. The specific heat is maximum and the superisentropic gradient is minimum at heights where the degree of ionization is neither too small nor too large. At the same time, under such conditions, due to the low transparency, the radiative thermal conductivity proves to be minimum and, accordingly, the conductive temperature gradient to be maximum. Therefore, especially high values of the superisentropic temperature gradient are inherent in zones of partial ionization. These zones are, thus, the layers where the convective instability of the material is highest. In the models of the Sun's interior structure regarded as most reliable in the 1960s, the depths of these layers crudely corresponded to the sizes of granules and supergranules. On this basis, Simon and Leighton [3] suggested that the initiation of convective flows on these two characteristic scales is associated in some way with the action of the increased driving force of convection in these two layers.

November *et al.* [4] detected mesogranulation and determined its characteristic scale. Following the idea of Simon and Leighton [3], they associated this scale with the position of the layer of partial single ionization of helium. Accordingly, the supergranulation scale is determined by the double ionization of helium.

Note that this quite reasonable hypothesis, when taken alone, in no way resolves the issue of the coexistence of different scales. The presence of height intervals of enhanced convective instability is not sufficient to account for motions on the distinguished scales, confined to certain height zones in the convective envelope. The results of various studies of convection in fluid layers with complicated stratification show that situations with scale-spectrum splitting are nontrivial: this effect requires fairly restrictive conditions on the height distribution of parameters. Therefore, convective circulation involves, as a rule, the entire thickness of the layer [1]. This means that only the existence of giant cells (precisely that phenomenon that has not been established with certainty) can easily be accounted for. Moreover, the example presented by certain simple problems shows that, even if sufficiently large gradients are present within rather narrow height intervals so that splitting of the spectrum is possible, the flow scales are not known *a priori*—they do not necessarily correspond to the depths where the most unstable layers are situated and may be several times larger [5, 6].

Let us return to the two groups of factors that determine the flow structure. While the effects of complicated

Cell type	Size, 10^3 km	Lifetime	Horizontal velocities within cells
Granules	~1	5–10 min	?
Mesogranules	5–10	$\gtrsim$2 h	~0.4 km/s
Supergranules	~30	$\gtrsim$1 day	0.3–0.5 km/s
Giant cells	$\gtrsim$200	tens of days	$\lesssim$10 m/s

stratification have not yet been adequately described, hydrodynamic instabilities remain completely outside investigators' field of vision (this refers to *flow instabilities*; the role of *convective instability* as the origin of convection is, obviously, beyond question). In the mean time, without studying these instabilities, neither particular features of the scale spectra of convective flows nor the spatial shapes of various structures observed in these flows can be understood.

3. HIGH-RESOLUTION OBSERVATIONAL DATA

The video records obtained by Title *et al.* [7] using the Solar Optical Universal Polarimeter (SOUP) of the *Spacelab 2* orbital laboratory on the *Challenger* space shuttle provide observational material that is extremely informative for investigations of the dynamics of the photosphere and upper subphotospheric layers. Along with primary material, images processed in one way or another are presented in these records. Let us note here some features of the photospheric dynamics that are revealed by this movie or are mentioned in some publications.

First of all, a cellular organization can clearly be traced in granular motions. The cells of the horizontal-velocity field correspond to mesogranules (more precisely, according to [7], a superposition of mesogranular and supergranular patterns is observed). Granules run apart from the central regions of mesogranules and, in most cases, disappear at their peripheries; in other words, they conform to the order dictated by the mesogranules. (More recently, the results of a continuous three-hour series of observations at the Pic du Midi Observatory showed that mesogranules are, in turn, carried by supergranular motions [8].) This finding is confirmed by the field patterns of the divergence of the horizontal velocities, as presented in the movie, and by fragments of the movie that demonstrate the motion of model test particles (corks) calculated from these velocities. The divergence field coded by the image brightness demonstrates an alternation of light and dark squares (i.e., an alternation of regions of positive and negative divergence), so that the pattern as a whole resembles a checkerboard. According to [7], the velocities of granular motions are 0.1–0.5 km/s.

A spatially ordered arrangement of granules on a mesogranular scale can also clearly be seen in many high-resolution photographs of granulation. In particular, such spatial organization was considered by Amal'skaya [9], who noted that "intergranular lanes in the quiet solar photosphere frequently form star-shaped structures with a dark central knot and a varying number of rays—intergranular lanes, which diverge from the center in different directions" (Fig. 1). True, the characteristic size of such structures is indicated to be 2100–2400 km, which is obviously smaller than the size of a mesogranule. However, the procedure used to determine this size (from the positions of the ends of the longest rays) should sys-

tematically and substantially underestimate it: the ray does not necessarily stretch to the outer boundary of the ordered group of granules as a regular, continuous lane.

Some other features of the photospheric dynamics reflected by the SOUP movie whose detection is regarded by Title *et al.* [7] to be an important observational result are related to the behavior of so-called exploding granules. Exploding granules display a rapid growth in size followed by a darkening in their central regions, after which they become expanding annuli (Fig. 2). In contrast to the formerly accepted view, "explosions" of granules are by no means a rare phenomenon: at least one such event occurs in a $10'' \times 10''$ area (corresponding approximately to the area of a mesogranule) every 400 s. It is remarkable that the emergence and evolution of exploders are closely linked to the dynamics of the mesogranular flow. Exploders "appear almost exclusively in the center of mesogranular size flow cells" [11]. The radial expansion velocity of the annulus is estimated to be 1–2 km/s [7]. The annulus breaks down into smaller fragments and disappears at the periphery of the cell.

To interpret the relationship between mesogranules and exploders, Simon, Title, and Weiss [12, 13] proposed a model in which randomly distributed exploders themselves produce a velocity-field component that is superposed on the spreading mesogranular flow. Although such a formal superposition results in a pattern similar to that observed, the physical mechanism that could produce it remains obscure.

Here, we put forward a simple hypothesis based directly on the physics of the phenomena.

4. INSTABILITIES OF CONVECTIVE FLOWS

Convection can assume diverse spatial forms. Two-dimensional roll convection (Fig. 3a) and the flows that produce hexagonal cells (Fig. 3b) are known most widely and considered most frequently. The form of the flow is primarily determined by the spatial distribution of the physical parameters of the material; in general, other factors that can be reduced to initial and boundary conditions may also be important (a detailed discussion of these points can be found in [1, 2]).

In studies of the structure of convective flows on the Sun, it would be desirable to know how three-dimensional flows are rearranged when they lose their stability as a parameter of the convection regime goes beyond the range in which the flow is stable. Ideally, a bifurcation diagram—the distribution of possible flow forms—should be constructed for a large region of parameter space. Such a detailed investigation of the full nonlinear problem of convection is still a long way off, even if we are only interested in the simplest case of an incompressible and almost uniform fluid (a plane horizontal layer of which is heated from below). However, the question of stability has already been studied fairly well for the roll flows typical of this case.
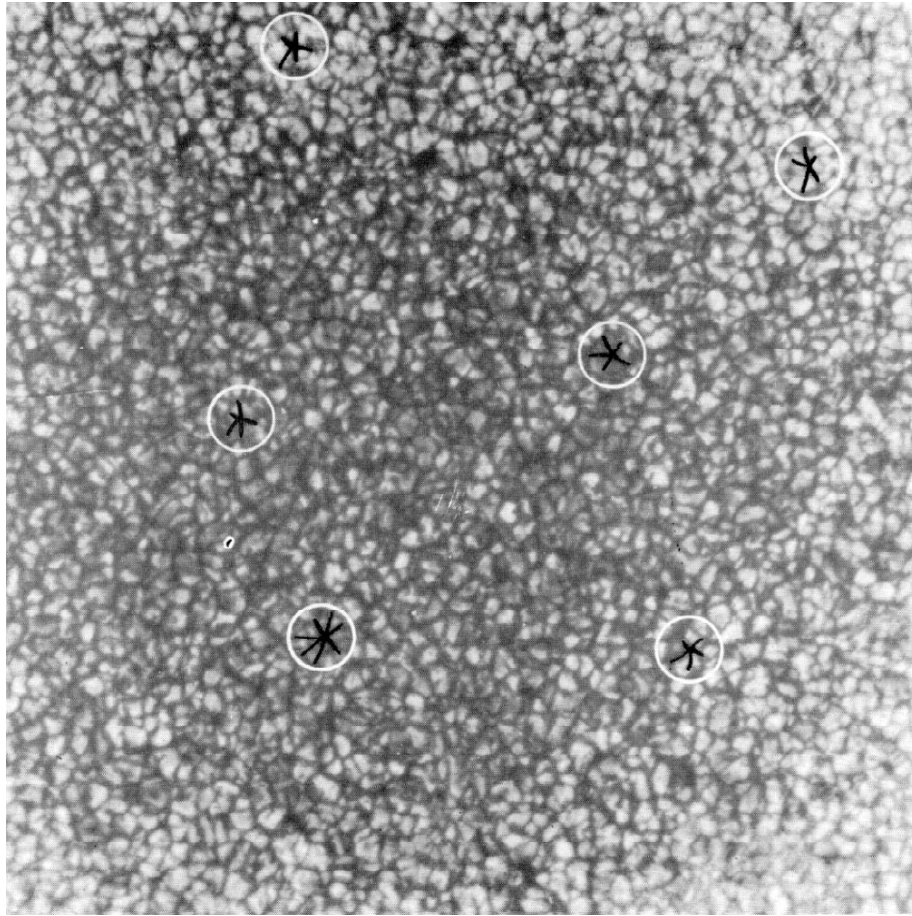
Fig. 1. A photograph of solar granulation in which some star-shaped intergranular-lane structures are marked [9].
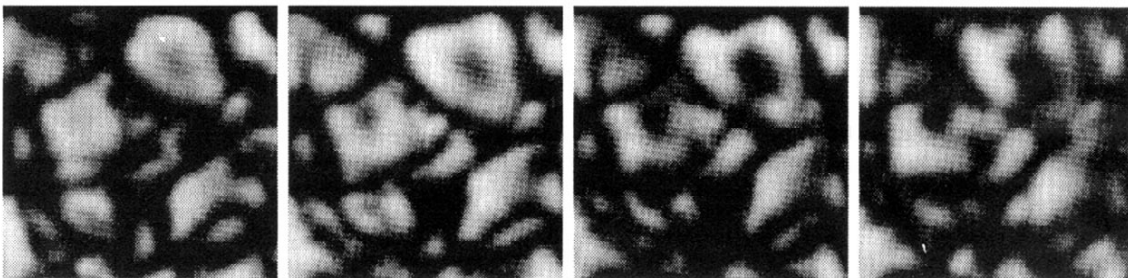
Fig. 2. Evolution of exploding granules [10]. The photographs of a $7'' \times 7''$ area were taken one minute apart.

In an extensive series of studies, Busse and his coauthors (see [1, 2] for a review) calculated such flows using a Galerkin method and the full nonlinear equations, then analyzed their stability in a linear approximation. The results of these studies are summarized in Fig. 4, which depicts the roll stability region in (k, P, R) space. This region is sometimes referred to as the "Busse windsock." Here, k is the wavenumber specifying the horizontal period of the roll flow (the reciprocal of the roll width), and P and R are the Prandtl and the

Rayleigh numbers: $P = \nu/\chi$ (where ν is the kinematic viscosity of the fluid and χ is its thermal diffusivity) and $R = \alpha g \Delta T h^3 / \nu \chi$ (where α is the volumetric thermal-expansion coefficient of the fluid, g the free-fall acceleration, ΔT the temperature difference between the lower and upper layer boundary, and h the layer thickness). Roll flows are stable against infinitesimal perturbations inside the windsock, and this stability is lost at its boundary. The various marked parts of the boundary show the thresholds at which various perturbation
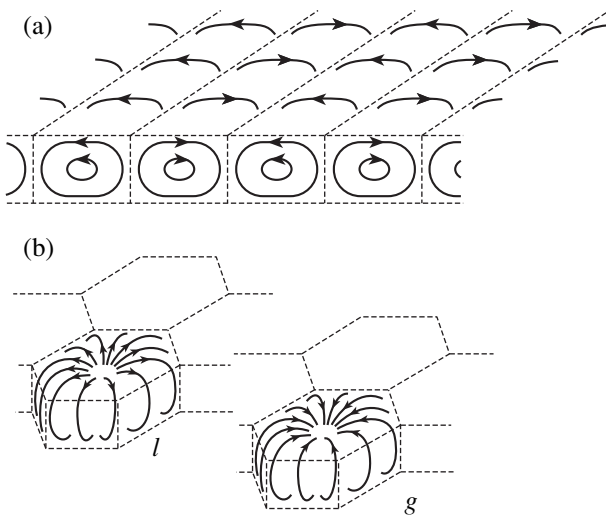
Fig. 3. Schematic of convection cells: (a) two-dimensional rolls and (b) hexagonal cells of two types, which differ in the direction of circulation of the fluid in a cell.

modes start to develop. Without going into detail and without considering all these modes (which are described, e.g., in [1, 2]), we focus our attention on four of them.

The cross-roll (CR) instability gives rise to a secondary flow in the form of rolls perpendicular to the original ones. Such crossed rolls begin developing in the thermal boundary layers produced by the main flow; accordingly, they are somewhat pressed up against the layer boundaries (they occupy only part of the layer thickness) and have smaller widths than the original rolls.

There is also an additional, relatively long-wavelength, branch of the CR instability called the knot (K)

instability. It derives its name from the fact that, at sufficiently large R values, it results in the formation of concentrated rising and falling plumes and of a pattern of "knots," clearly observed in experiments—these knots are streamline bunches formed by diverging or converging horizontal streams.

The pattern of fully developed knot convection appears as a *spoke* pattern, in which a system of irregular polygons is observed instead of the original roll pattern. Sheets of hot and cold fluid erupting from the thermal boundary layers at the upper and lower boundaries of the fluid layer are stretched radially with respect to the plumes and appear as spokes (Fig. 5). The fine fluctuating features of this pattern are spatially ordered—they are controlled by the steady large-scale structure.

Two more instability modes we will need are designated BE1 and BO2. These are associated with the emergence of blobs of overheated and overcooled material (compared to the ambient fluid) in the cross section of a roll, which are then carried by the convective circulation (Fig. 6). These instabilities are called the one-blob and the two-blob instability, respectively [in the above notation, the letter B means *blob*, the digit indicates the number of overheated (and overcooled) blobs in the roll cross section, and the letters O and E characterize the symmetry of the corresponding perturbations in a specific geometrical sense—odd or even].

As noted above, the diagram in Fig. 4 was obtained from a linear stability analysis. In any particular case, this diagram merely indicates the threshold values of the parameters at which the roll flow becomes unstable; thus, it fails to predict the form of the flow at appreciable distances from the surface of the windsock. Nevertheless, the diagram suggests the character of variations in the well-established flow with distance from this surface. For example, it is quite reasonable to expect that
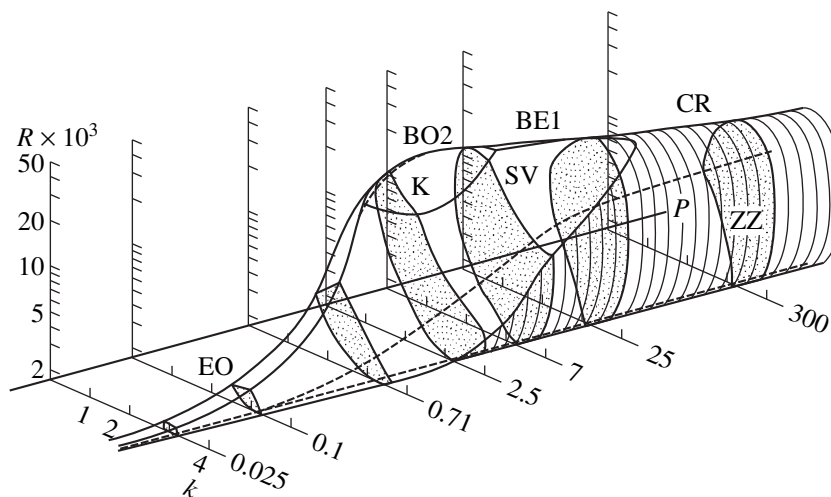
Fig. 4. Region of stability of spatially periodic convection-roll patterns in (k, P, R) space (the "Busse windsock"); adapted from [14]. The calculations were carried out for a layer with rigid horizontal boundaries. Parts of the surface delimiting the stability region corresponding to the thresholds for the development of various instabilities are marked according to the notation used for these instabilities.
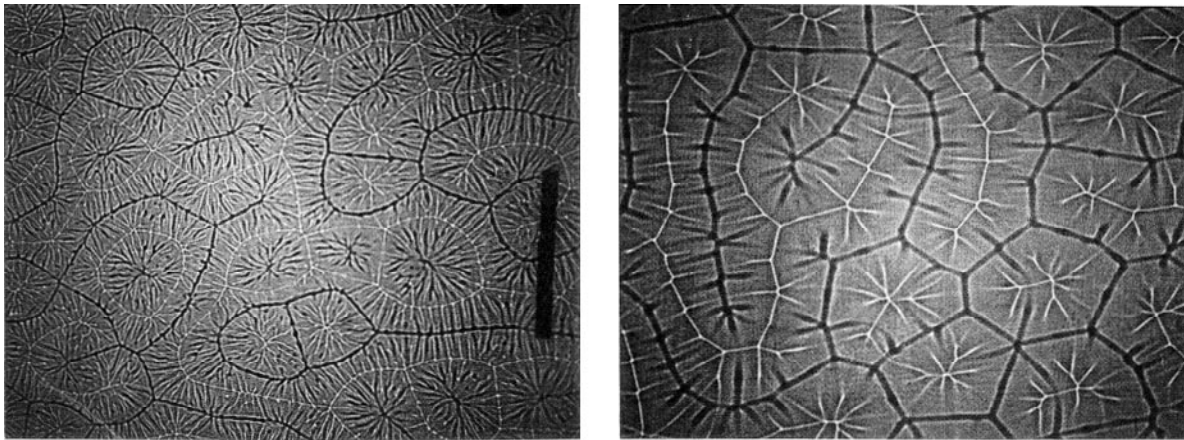
Fig. 5. Experimental photographs of spoke-pattern convection [15]. Left: $R \approx 5 \times 10^4$, $P = 7$ (methyl alcohol); right: $R = 9 \times 10^4$, $P = 64$ (silicone oil).

BE1   BO2
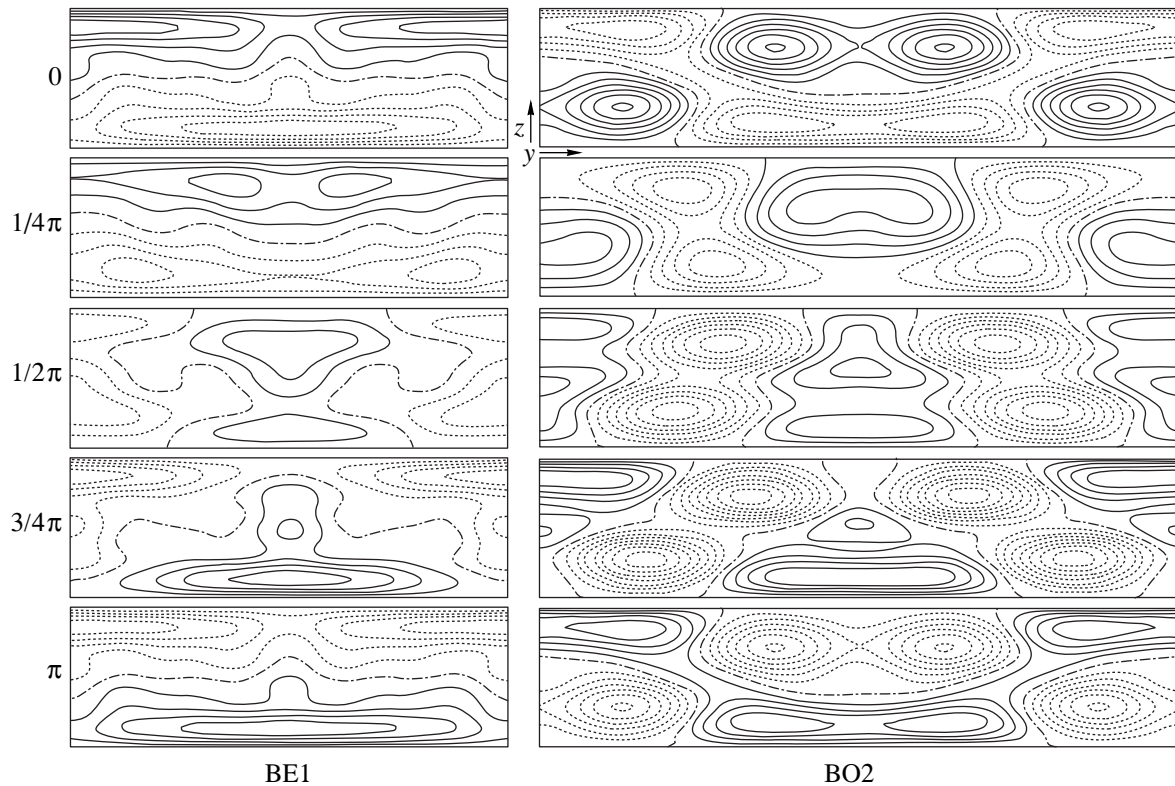
Fig. 6. Temperature perturbations due to "blob" instabilities in a cross section of a pair of rolls [16] (superposed on the steady temperature distribution characteristic of well-established roll convection). The top-to-bottom sequence of plots corresponds to phases 0, $\pi/4$, $\pi/2$, and $3\pi/4$ of the period associated with the roll rotation. Left: one-blob instability BE1; right: two-blob instability BO2. Positive and negative values of the temperature perturbation are shown by solid and dotted isotherms, respectively.

if, for a moderate Prandtl number (crudely, within the range 1–10), the Rayleigh number is increased above the values specifying the upper boundary of the windsock, a pattern typical of the knot instability or some blob instability will first be observed; then, at even larger R values, this pattern will be replaced by a combination of secondary disturbances generated by these instabilities. It is important that intense secondary flows that develop well away from the instability threshold can strongly distort (or even completely disrupt) the flow that was regarded as original (unperturbed) in the stability analysis—this was already evident from the spoke pattern example. In most cases, this implies that the flow pattern established is generally typical of the

given region of parameter space, and depends only weakly on the pattern's previous history: whether this pattern was derived by leaving the stability region for rolls or any other (three-dimensional) primary flow; moreover, such a flow could develop from random noise perturbations.

5. ARE GRANULES A PRODUCT OF MESOGRANULE INSTABILITY?

Let us now discuss how the instabilities discussed above can be manifest under solar conditions. Even a purely visual examination indicates that the patterns shown by the spatial organization of granules on mesogranular scales clearly resemble convection spoke patterns. The impression of a close relationship (both genetic and dynamic) between mesogranulation and granulation is reinforced if we turn to observational material that shows the mesogranular cellular structure of the horizontal-velocity field; as we know, this structure is quite pronounced due to the transport of granules by mesogranular motions (see Section 3). Similar to what is observed in convection experiments, the mesogranular-scale flow appears to be quasi-stationary compared to the pattern of the granules, which constantly move and change their shapes. The granulation pattern seems to be an imprint of the fine structure of the mesogranular velocity field, which should be responsible for the deformation and fragmentation of bright features—granules. It is natural to suppose that this fine structure is produced by a secondary flow that results from an instability of the primary, mesogranular, field.

Similarly, granules themselves could be a product of some instability. If such a point of view is accepted, the origin of both normal and exploding granules can be uniquely accounted for.

Let us assume that the physical conditions are suitable for the operation of a mechanism like a blob instability in a three-dimensional convection cell—mesogranule. That this is possible in some region of the parameter space for a three-dimensional flow is far from a daring assumption; on the contrary, it is almost certain. This is true because there are no known reasons why only two-dimensional convection should be amenable to blob instabilities. Moreover, under solar conditions, radiative transfer can provide additional destabilization, since this mechanism is known to enhance the effects of various overheating instabilities. A hot material is less transparent, reducing the cooling rate compared to the case with no radiative heat transfer.

Let us imagine that each of the plots in Fig. 6 depicts a cross section of two contiguous three-dimensional (polygonal) cells rather than a cross section of a roll pair, and that upflows are present in the central parts of these cell (the side regions of the plots). Hotter material glows more brightly. Therefore, if we observe the upper surface of the layer, we will see at some time the emergence of a bright spot at the center of the cell. The spread of material in the uppermost region will stretch this spot, and its center will soon darken, since the overheated material will be replaced with cooler material. In other words, we will observe an "explosion" of the granule. Subsequently, the overheated material will sink at the periphery of the cell. Under natural conditions, as a rule, we will not observe only one pure perturbation mode, and the pattern will be more complex. The overheated blobs that originate inside the mesogranule should not necessarily be carried upward at the mesogranule's center and could be carried at some distance from it. They should not necessarily appear as annuli surrounding the center of the cell and may be more or less compact features. Such spots will also be observed as granules, but "normal" rather than exploding. As already noted, the small-scale secondary flows that should arise against the background of the mesogranular circulation will lead to the fragmentation of the granules and create the fine details of the granular pattern.

It may appear that the agreement between the observationally determined [7] radial expansion velocities of exploding granules (1–2 km/s) and the velocities of motion of normal granules (0.1–0.5 km/s) is not good, whereas they should coincide if the proposed interpretation of the phenomena is true. In this context, we should consider the methods used to determine these velocities.

The velocities of granular motion were measured by the method of local correlation tracking [11]. In other words, the local velocity vector was determined from the displacement of the position of the maximum cross correlation between images of a small surface area obtained at different times. The measured velocity reflects the displacement of the *center of gravity* of the brightness distribution and, as shown in [11], strongly depends on the size of the areas used in such measurements. In the same study [11], the expansion velocities of exploders were calculated using diagrams that represented the coordinates of the brightness maxima in some photometric section of the granule as functions of time. Conventionally speaking, the diagram appeared like a < sign, and the velocity was determined from the angle between the upper and the lower curve. Naturally, the result should depend on the choice of the section.

Thus, the velocities were measured differently in the two cases, and the results are fairly sensitive to the details of the measuring procedure. Moreover, it is quite reasonable to expect a large dispersion in the velocities of normal granules, since this velocity depends on the position of the granule within the boundaries of the mesogranule. In view of these arguments, the available data on the velocities of normal and exploding granules cannot be considered contradictory.

It would be good to verify whether or not the parameters of the solar convection zone agree with the convection regime parameters at which the convective-flow instabilities considered above can develop. Regrettably, this cannot be done at present with any reasonable

confidence. The Rayleigh and Prandtl numbers based on the available (fairly uncertain) estimates of the molecular transport coefficients differ by many orders of magnitude from (larger and smaller than, respectively) the values for which we could expect even the existence of relatively ordered, quasi-stationary mesogranular (or any other) flows, to say nothing of the above-mentioned instabilities. However, it is absolutely clear that such estimates of ν and χ for the solar convection zone are not relevant. The character of flows in this zone should be governed by the turbulent transport coefficients, and the numbers R and P for the region considered are quite likely to fall in the "needed" ranges. In particular, an effective Prandtl number of order unity is considered to be quite plausible.

Thus, on the basis of our discussion, we can formulate our hypothesis as follows. Mesogranules are the main structural features of the photospheric velocity field. In contrast, granules behave, to first approximation, as passive tracers—blobs of hotter material carried by mesogranular motion. They owe their origin to some overheating instability similar to the "blob" instabilities of convection rolls. The features of the granulation pattern (including granule fragmentation) reflect the fine structure of the velocity field; the flow instability causes this structure to resemble the spoke patterns of convection. Granules are, therefore, a product of mesogranule instability. Exploders do not represent a particular class of object; among other granules, they are distinguished only by the fact that they emerge from deep in the central parts of mesogranules.

Note that, based on photometric observations of the solar surface and velocity measurements, Abdussamatov and Zlatopol'skiĭ [17] also consider granules to be a mesogranular product—secondary, or daughter structures. However, in fact, they treat the convection zone merely as a collection of rising and sinking elements on differing scales. As a result, such points as structural order in the flows and physical mechanisms for the formation of flow patterns fall beyond the scope of their discussion.

6. CONCLUSION

Let us summarize our conclusions. Usually, only thermogravitational convective instability, due to the nonuniform heating of material and the action of the buoyant force, has been taken into account in studies of the solar convection zone and photosphere. However, this approach seems unwarranted. Other hydrodynamic instabilities can play an important role in the dynamics of these layers; in particular, they may be responsible for the formation of the structures observed there.

The notion that mesogranules are the basic structural elements of the velocity field, granules are a product of mesogranule instability, and exploders are phys-

ically no different from normal granules is consistent with available high-resolution video records.

REFERENCES

1. A. V. Getling, *Rayleigh–Bénard Convection: Structures and Dynamics* (World Scientific, Singapore, 1998; URSS, Moscow, 1999).
2. A. V. Getling, Usp. Fiz. Nauk **161** (9), 1 (1991) [Sov. Phys. Usp. **34** (9), 737 (1991)].
3. G. W. Simon and R. B. Leighton, Astrophys. J. **140** (3), 1120 (1964).
4. L. J. November, J. Toomre, K. B. Gebbie, *et al.*, Astrophys. J. Lett. **245** (3), L123 (1981).
5. A. V. Getling, Izv. Akad. Nauk SSSR, Mekh. Zhidk. Gaza, No. 5, 45 (1975).
6. A. V. Getling, Izv. Akad. Nauk SSSR, Fiz. Atmos. Okeana **16** (5), 529 (1980).
7. A. M. Title, T. D. Tarbell, G. W. Simon, and the SOUP Team, Adv. Space Res. **8** (8), 253 (1986).
8. R. Muller, H. Auffret, T. Roudier, *et al.*, Nature **356** (6367), 322 (1992).
9. S. I. Amal'skaya, Soln. Dannye, No. 3, 87 (1990).
10. P. Foukal, *Solar Astrophysics* (Wiley, New York, 1990).
11. A. M. Title, T. D. Tarbell, K. P. Topka, *et al.*, Astrophys. J. **336** (1), 475 (1989).
12. G. W. Simon, A. M. Title, and N. O. Weiss, Astrophys. J. **375** (2), 775 (1991).
13. G. W. Simon, A. M. Title, and N. O. Weiss, Adv. Space Res. **11** (5), 259 (1991).
14. F. H. Busse and R. M. Clever, Arch. Mech. **43** (5), 565 (1991).
15. F. H. Busse, Acta Mech. Suppl. **4**, 11 (1994).
16. E. W. Bolton, F. H. Busse, and R. M. Clever, J. Fluid Mech. **164**, 469 (1986).
17. H. I. Abdussamatov and A. G. Zlatopol'skiĭ, Pis'ma Astron. Zh. **23** (11), 863 (1997) [Astron. Lett. **23**, 752 (1997)].

Translated by A. Getling

The Gap in the Gaseous Disk of the Galaxy as a Manifestation of Processes in the Corotation Region

Yu. N. Mishurov

Space Research Department, Rostov State University, ul. Zorge 5, Rostov-on-Don, 344104 Russia

Received August 30, 1998

Abstract—The evolution of a system of a large number of particles ($N \sim 4 \times 10^4$) moving in planar trajectories in the gravitational field of the Galaxy is simulated with allowance for perturbations by a spiral density wave that give rise to spiral arms (the problem of a collisional N-body system in a specified external field). The particles simulate the motion of diffuse HI clouds in the Galaxy. The spiral-wave parameters are chosen so that the corotation region lies in the vicinity of the Sun. The spiral field pumps cloud out of the corotation region, creating a trough or gap in the initially monotonic radial distribution of particles near the corotation circle. At the same time, the arms proper exhibit no conspicuous features near corotation. This trough could explain the gap in the Galactic HI distribution observed near the solar circle and can be used to locate the corotation region if combined with other data. © 2000 MAIK "Nauka/Interperiodica".

1. INTRODUCTION

Marochnik *et al.* [1] analyzed the global spiral pattern of the Galaxy and concluded that the Sun is located near the so-called corotation resonance, where the angular velocity of the spiral pattern is equal to that of the Galactic disk. This conclusion is strongly at variance with the results of Lin *et al.* [2] who argued that the corotation circle is far from the Sun at the edge of the Galaxy. At first glance, this discrepancy seems surprising, since both studies used the same observational data. However, there is nothing mysterious here. The results of [1] are based on a model that differs from that used by Lin *et al.* [2]; namely, Marochnik *et al.* [1] considered the Galaxy to be a multicomponent system, whereas Lin *et al.* [2] modeled it as a single rotating disk.

Note that the discrepancies between the two models for the spiral pattern in our Galaxy do not reduce to simple quantitative differences, although even these have far-reaching implications. The differences between the models have a fundamental nature [3], making the problem of determining the corotation radius especially urgent.

In their independent analysis of stellar kinematics, Crézé and Mennessier [4] concluded that the corotation radius is located within the solar circle. It is important that their method allows computation of the spiral-pattern parameters without any assumptions about the global structure of the Galaxy. Furthermore, their conclusions are based on data that are different from those used in [1]. Mishurov *et al.* [5] and Pavlovskaya and Suchkov [6] modified the method of Crézé and Mennessier [4], used it to analyze the velocity fields of various stellar groups, and concluded that the solar trajectory is close to the corotation circle.

Subsequent studies have demonstrated that it is very important to know whether the Sun is located near the corotation radius. For instance, Nelson and Matsuda [7] discovered that certain features of the 21-cm line distribution can be explained only if the corotation region is located near the solar circle. This also provides an easy solution to the problem of variations in the synchrotron emission in the solar neighborhood [8]. Furthermore, it flows from the results of Burton [9] that the distribution of molecular gas in the Galaxy can be understood if the Sun is close to the corotation circle.

New data on the velocity field of Galactic Cepheids, including the results of the HIPPARCOS mission, have allowed estimations of the corotation radius on a qualitatively new level [10–12]. The fundamentally new result obtained in these studies is that the corotation region is within only 100–200 pc of the solar circle, compared to the roughly 1 kpc estimated in previous works. The radius of the epicyclic orbit of the Sun is ~200 pc, implying that the solar trajectory virtually coincides with the corotation circle.

These results demonstrate how important it is to locate the corotation circle in the Galaxy. This motivates the task of looking for additional manifestations of corotation, apart from those noted above (see also [13]). Our aim here is to investigate this question.

2. BASIC IDEA

There have been several attempts to use various structural features of galactic disks, such as spurs or rings, to locate resonance regions (see [14] and refer-

ences therein). We suggest an observational test that, in our opinion, could be used to locate the corotation circles in spiral galaxies. Burton [9] pointed out a gap in the radial HI distribution in the Galaxy (see Fig. 6 in [9]), which shows a conspicuous trough at a Galactocentric distance of about 11 kpc; note that this paper used an old distance [9] scale with a solar Galactocentric radius of $R_0 = 10$ kpc).

The existence of such a trough in the gas distribution could naturally be attributed to the corotation circle. The gravitational field of the spiral density wave pumps gas out of the corotation region. We first explain our idea qualitatively and then present the results of quantitative computations.

It is well known that galactic shocks form in the gas flowing into a spiral arm [15]. The result of the interaction between the gas clouds and spiral waves (via the galactic shock) depends on the relative velocity of the wave and surrounding medium. It is important for our subsequent analysis that the spiral wave rotates rigidly (its angular velocity $\Omega_P = $ const), whereas the galactic disk rotates differentially with an angular velocity Ω that is a function of galactocentric radius R. The corotation radius R_C is determined from the condition $\Omega(R_C) = \Omega_P$.

If $R < R_C$, $\Omega > \Omega_P$, so that the gas overtakes the spiral wave and flows into it from the inner edge. The gas then decelerates in the spiral arm, and the overall galactic gravitational field moves its orbit closer to the galactic center.

Beyond the corotation circle $R > R_C$, $\Omega < \Omega_P$, and the situation is reversed. The wave overtakes the gas and "pushes" it. As a result, the gas moves into an orbit that is further from the galactic center, providing a qualitative interpretation for the gaps observed in spiral galaxies.

Fridman and coworkers (see [16]) have developed a theory for the redistribution of matter in the vicinity of resonances in the framework of a weak perturbation approximation. They have used this theory to interpret the fine structure of planetary rings, in particular, the well-known Cassini division in the rings of Saturn. Gor'kavyĭ and Fridman [16] also point out certain analogies between planetary rings and galactic disks. Thus, the aforementioned gap in the HI distribution in our Galaxy and the famous Cassini division in Saturn's rings could be closely related phenomena.

In the current paper, we analyze the evolution of an ensemble of N particles simulating the behavior of a system of diffuse HI clouds in the external Galactic gravitational field perturbed by the density wave responsible for spiral arms. We neglect the effect of the density wave on the matter redistribution. At the same time, direct numerical integration of the equations of motion for N particles with allowance for mutual collisions enables analyses of finite-amplitude perturbations, including those due to shock waves.

3. MATHEMATICAL FORMULATION AND EQUATIONS

Thus, we are dealing with the planar (two-dimensional) motion of N particles in the Galactic gravitational field. We assume the gravitational field to be specified (i.e., we determine the motion of particles in the external field). The particles simulate gas clouds, and our model includes collisions between them.

Broadly speaking, our problem is similar to that considered in [17]. However, we use a somewhat different model for the Galactic gravitational potential. One important difference is that, in our analyses, the corotation circle is located near the Sun, whereas Roberts and Hausman [17] place it at the edge of the Galaxy and do not even address the question of the gap in the radial gas distribution.

Model of the galactic gravitational potential. In accordance with the density-wave theory for the spiral patterns in galaxies, we represent the gravitational potential φ_G as the sum of two components:

$$\varphi_G = \varphi_0(R) + \varphi_S(R, \vartheta, t), \qquad (1)$$

where φ_0 is the unperturbed axisymmetric potential, φ_S the spiral density-wave perturbation, R and ϑ Galactocentric polar coordinates, and t time.

We adopted a functional form for $\varphi_0(R)$ in accordance with the well-known model of Allen and Santillan [18]. We do not write the corresponding formulas here due to their unwieldiness. We note only that $R_0 = 8.5$ kpc in this model.

The expression for φ_S has two different forms for $R > R_{in}$ and $R < R_{in}$, where R_{in} is the radius of the inner Lindblad resonance [2]. According to the theory of galactic density waves:

$$\varphi_S = A\cos 2\left[\cot i \ln\left(\frac{R}{R_0}\right) - \vartheta + \Omega_p t\right], \qquad (2)$$

if $R > R_{in}$. Here, A is the amplitude of the spiral gravitational potential ($A < 0$), given by $A = 0.5F(\Omega_0 R_0)^2 \tan i$; F is the dimensionless amplitude of the radial component of the perturbing force [17]; $\Omega_0 = \Omega(R_0)$; i is the pitch angle ($i < 0$ for winding spirals); and the factor of two in the cosine argument of (2) corresponds to a two-armed spiral pattern (the qualitative picture is the same for a four-armed pattern).

Strictly speaking, these formulas are valid only in the region between the inner and outer Lindblad resonances [2] (we denote the radius of the latter R_{out}). We cut off both the perturbed potential and the perturbing force beyond R_{out}. The cutoff factor γ has the form of the smooth function

$$\gamma = \left[1 + \exp\left(\frac{R - R_{out}}{c}\right)\right]^{-1},$$

where c is the scale length of the potential cutoff.

We now discuss the model of the gravitational potential when $R < R_{in}$. We are interested primarily in what happens near $R \sim R_0$, and, therefore, the exact form of the φ_S dependence in the central region is of little importance. However, to provide a complete picture, we use the currently popular idea that there is a barlike structure at the center of the Galaxy and write the perturbed potential in the form:

$$\varphi_S = B\exp\left\{-\left[\left(\frac{x'}{a}\right)^2 + \left(\frac{y'}{b}\right)^2\right]\right\}, \qquad (3)$$

where

$$x' = R\cos(\vartheta - \vartheta_{in}),$$

$$y' = R\sin(\vartheta - \vartheta_{in}), \qquad (4)$$

$$\vartheta_{in} = \cot i\ln\left(\frac{R}{R_0}\right) + \Omega_p t,$$

$B = A\exp\left(\frac{R}{R_0}\right)^2$, and a and b are the spatial scale lengths of φ_S. It is evident from (3) and (4) that the equipotential lines (in the Galactic plane) have the form of ellipses rotating with angular velocity Ω_P.

Cloud–cloud collisions. Unlike stars, the clouds form a collisional system. Therefore, evolutionary computations for an ensemble of cloud particles should include collisions between them.

Here, we are not interested in the formation of molecular complexes and restrict our analysis to the narrower problem of interpreting the gap in the radial distribution of Galactic neutral hydrogen in the vicinity of the corotation circle. We accordingly assume that our particles all have the same mass. In an approximation with instantaneous two-body collisions between spherical particles, each elastic collision simply rotates the relative particle velocity vector $\Delta\mathbf{u}$ by some angle χ, leaving its absolute value unchanged (the scattering angle χ can be found from equation $\cos\chi = 2\left(\frac{\rho}{d}\right)^2 - 1$, where ρ is the impact parameter and d the diameter of the particles). To allow for inelastic collisions, we modify the above result in accordance with [17] as follows. We assume that the scattering angle after collision is given by the same formula as in the elastic case, but the absolute value of the relative cloud velocity is equal to $\varepsilon\Delta u$, where ε is an elasticity factor. $\varepsilon = 1$ and 0 for completely elastic and inelastic collisions, respectively, and $0 < \varepsilon < 1$ in intermediate cases. We repeated our computations with various values of ε.

The mean free path is an important parameter in our problem. In our (two-dimensional) geometry, it is equal to

$$\lambda_2 \sim \pi R_G^2/\sqrt{2}dN, \qquad (5)$$

where R_G and N are the radius of the gaseous disk and the number of particles, respectively. We treat (5) only as an order-of-magnitude equation, since the above estimates, as usual, assume that the particles are uniformly distributed in the disk, whereas the true distribution could be nonuniform. Note also that the denominator contains the particle diameter instead of the collision cross section.

On the other hand, the typical distance between particles is

$$D \sim \sqrt{\frac{\pi R_G^2}{N}}. \qquad (6)$$

It follows from the last two formulas that

$$\frac{D}{d} \sim \sqrt{\frac{2N}{\pi}}\frac{\lambda_2}{R_G}. \qquad (7)$$

Relations (5)–(7) impose certain restrictions on the parameters of the problem. To preserve the physical properties of the simulated system, we should choose mean free paths that are consistent with observations of diffuse HI clouds in the Galaxy—say, of order several hundred parsecs. On the other hand, D/d cannot be close to unity or the clouds would be in constant contact with their neighbors. All this, in turn, imposes certain constraints on the number of particles N in the experiment (see below).

Initial conditions. We take the amplitude of the perturbing potential to be zero at $t = 0$ (the initial time). The particles in the disk are distributed axisymmetrically and move in quasi-circular orbits in the regular field of the Galaxy. (Departures from purely circular orbits are due to chaotic particle motions, which we assume to be characterized by equal radial and azimuthal velocity dispersions, σ).

When $t > 0$, we turn on the perturbing field $F = F_0[1 - \exp(-\beta\Omega_0 t)]$ (here, F_0 is the observed dimensionless amplitude of the perturbing field at the Sun's location and β is a constant regulating the rapidity of the turn-on) and determine the system's response.

We adopted the following initial radial particle distribution (at $t = 0$). The initial surface density is

$$n = \frac{n_0}{1 + \exp\left(\frac{R - r}{L}\right)}, \qquad (8)$$

where L is the scale length of n, and n_0 and r are constants. Clearly, n_0 can be found from the normalization condition

$$N = 2\pi\int_0^{R_G} nR'dR'.$$
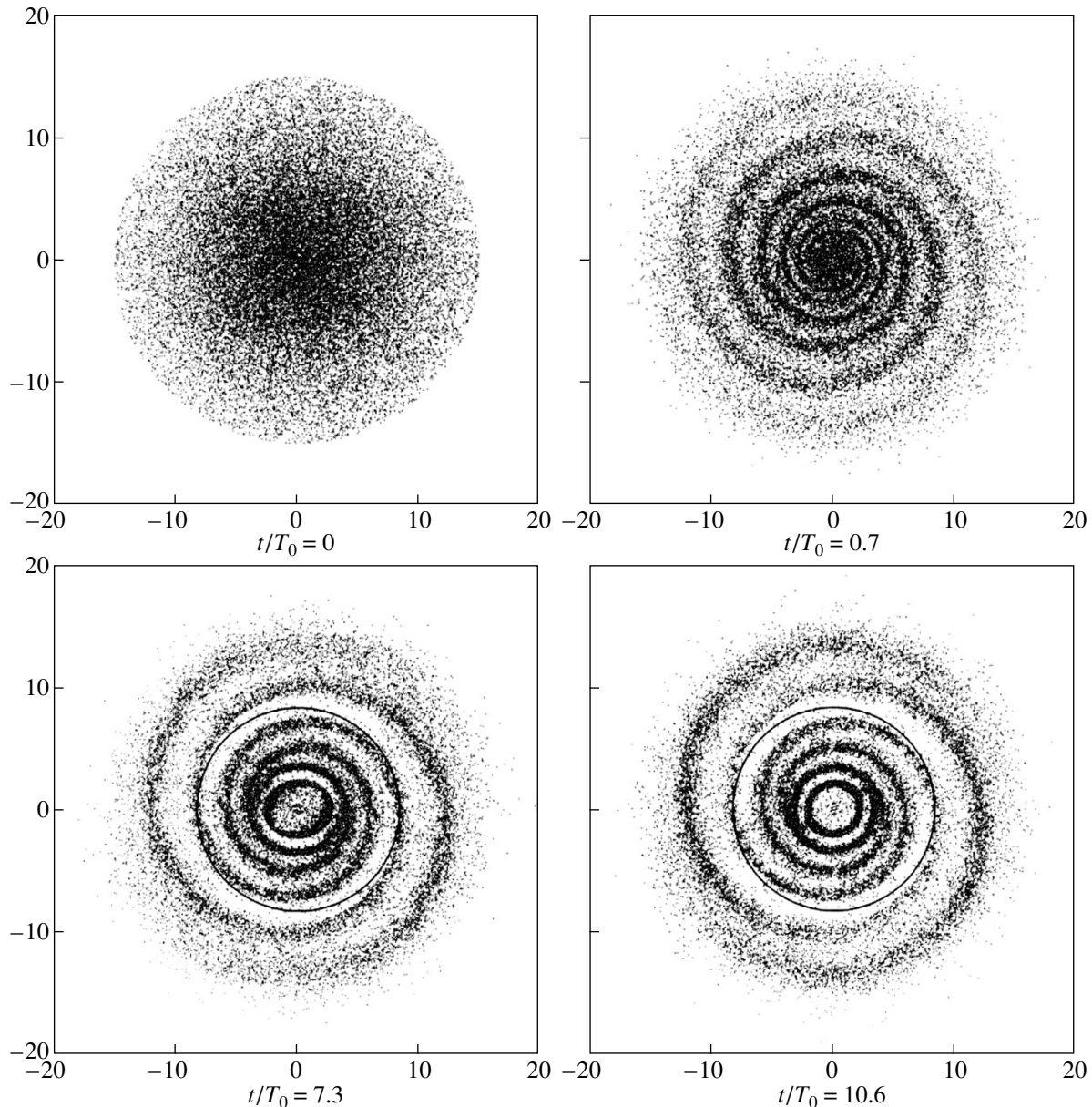
Fig. 1. Evolution of a system of cloud particles under the action of the gravitational field of a spiral density wave. $T_0 \approx 241$ Myr is the period of Galactic rotation at the solar Galactocentric distance. The ring indicates the corotation circle. The axes are in kpc.

By introducing the constant r, we avoid an unrealistically abrupt increase of the particle density at the center of the Galaxy. As is evident from (8), the density decreases exponentially at sufficiently large Galactocentric distances.

Computational features and parameter values. As in [17], we integrated the equations of particle motion using a fourth-order Runge–Kutta technique in a reference frame corotating with the spiral arms with angular velocity Ω_P. To speed up the computations, we calculate the gravitational force beforehand on a square grid with step Δ. We then perform a two-dimensional interpolation to compute the gravitational force at specified points.

After computing the particle locations after a time step τ, we look for all colliding pairs, i.e., for particles separated by a distance of less than d and approaching one another. We then compute the result of the collision. This procedure imposes a restriction on the time step, $\tau \leq d/\sigma$. However, since we compute the gravitational force via an interpolation, another restriction arises—$\tau \leq \Delta/\max(\Omega R)$—which proved to be more severe than the former one.

The problem is periodic with period π, and we therefore performed the computations only for one half of the disk.

$\langle n \rangle$, kpc^{-2}
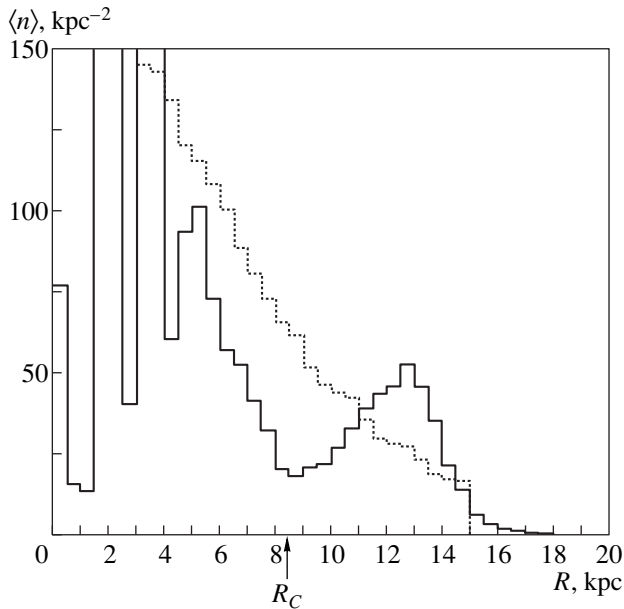
Fig. 2. Evolution of the radial distribution of the averaged (in rings) particle density $\langle n \rangle$ as a function of time. The dotted and continuous curves correspond to $t = 0$ and $t/T_0 = 10.6$, respectively.

We repeated our computations with various parameter values and present here the results obtained with the following parameters. The parameters of the initial particle distribution in the disk were $N = 4 \times 10^4$, $R_G = 15$ kpc, $L = 4$ kpc, and $r = 3$ kpc; $\sigma = 8$ km/s; the cloud diameter $d = 30$ pc (this choice of an "effective" cloud size yields a mean free path $\lambda_2 \approx 500$ pc, and we neglect the gravitational cross section of the cloud, since we consider a system of HI clouds); the collision elasticity factor $\varepsilon = 0.8$; the parameters of the spiral density wave were $F_0 = 0.1$, $\Omega_P = 26.5$ km s^{-1} kpc^{-1} (this results in $R_C \approx 8.3$ kpc; $R_{in} \approx 2.3$ kpc, and $R_{out} \approx 13.6$ kpc for the model of [19]), and the spiral-arm pitch angle $i = -7°$; the parameters of the central bar were $a = 3$ kpc and $b = 1$ kpc; the constant of the potential cutoff beyond the external Lindblad resonance $c = 1$ kpc; and $\beta = 0.2$.

4. COMPUTATION RESULTS

Figure 1 shows the development of structure in the system with time. It would be interesting to trace the formation of various features, such as the ring, or to analyze the formation of molecular clouds in the Galaxy at $R \sim 4$ kpc. However, we do not aim here to interpret various morphological features in the spiral pattern, and therefore do not discuss the pictures obtained in more detail.

Note that it is immediately evident that particles inside the corotation circle are concentrated toward the center and those beyond it are pushed outward, whereas the spiral pattern itself exhibits no conspicuous features

at the corotation circle. It follows that the corotation region cannot be located based only on the appearance of spiral arms.

However, it can be located from analyses of the radial distribution of gas. Figure 2 shows the temporal evolution of the distribution of the averaged (in rings) number density $\langle n \rangle$ as a function of the Galactocentric distance. It is immediately evident that the particles are, indeed, pumped out of the corotation region, resulting in a formation of a gap in the radial particle distribution at this radius.

5. CONCLUSION

We have numerically simulated the formation of the spiral pattern in a system of clouds in our Galaxy induced by the field of the spiral density wave. Our results show that spiral arms develop no conspicuous features near the corotation region that would enable location of this region based only on the appearance of spiral arms. However, in about seven Galactic rotations after the switch-on of the spiral field (at the solar Galactocentric distance), the Galactic spiral density wave produces a conspicuous gap in the initially monotonic cloud distribution near the corotation radius. The cloud density in this gap is lower than in neighboring regions. This could explain the gap in the radial HI-density distribution in the vicinity of the solar circle found by Burton [9].

Combined with other data, this result can be used to directly determine the locations of corotation regions in other galaxies.

REFERENCES

1. L. S. Marochnik, Yu. N. Mishurov, and A. A. Suchkov, Astrophys. Space Sci. **19**, 285 (1972).

2. C. C. Lin, C. Yuan, and F. H. Shu, Astrophys. J. **155**, 721 (1969).

3. L. S. Marochnik and A. A. Suchkov, *The Galaxy* [in Russian] (Nauka, Moscow, 1984).

4. M. Crézé and M. O. Mennessier, Astron. Astrophys. **27**, 281 (1973).

5. Yu. N. Mishurov, E. D. Pavlovskaya, and A. A. Suchkov, Astron. Zh. **56**, 268 (1979).

6. E. D. Pavlovskaya and A. A. Suchkov, Pis'ma Astron. Zh. **4**, 450 (1978).

7. A. H. Nelson and T. Matsuda, Mon. Not. R. Astron. Soc. **179**, 663 (1977).

8. E. S. Batova and Yu. N. Mishurov, Astron. Tsirk., No. 1426, 2 (1986).

9. W. B. Burton, Ann. Rev. Astron. Astrophys. **14**, 275 (1976).

10. Yu. N. Mishurov, I. A. Zenina, A. K. Dambis, *et al.*, Astron. Astrophys. **323**, 775 (1997).

11. Yu. N. Mishurov and I. A. Zenina, Astron. Astrophys. **341**, 81 (1999).

12. Yu. N. Mishurov and I. A. Zenina, Astron. Zh., 1998 (in press).

13. V. V. Lyakhovich, A. M. Fridman, O. V. Khoruzhiĭ, *et al.,* Astron. Zh. **74**, 509 (1997).

14. G. Byrd, P. Rautiainen, H. Salo, *et al.*, Astron. J. **108**, 476 (1994).

15. W. W. Roberts, Astrophys. J. **158**, 123 (1969).

16. N. N. Gor'kavyĭ and A. M. Fridman, *Physics of Planetary Rings* (Nauka, Moscow, 1994).

17. W. W. Roberts and M. A. Hausman, Astrophys. J. **277**, 744 (1984).

18. C. Allen and A. Santillan, Rev. Mex. Astron. Astrofis. **22**, 255 (1991).

Translated by A. Dambis